Imperial College
London

Measurement and Manipulation of Ultracold Bosons using Microfabricated Optics

James Garvie-Cook
September 2014

Thesis submitted in partial fulfilment of the
requirements for the degree of
Doctor of Philosophy of Imperial College London
and the Diploma of Imperial College

Centre for Cold Matter
Quantum Optics and Laser Science Group
Department of Physics
Imperial College London
London, SW7 2BW
United Kingdom

Declaration

I declare that the work in this thesis is my own, and that all the material that I used that is not my own has been properly acknowledged.

The copyright of this thesis rests with the author and is made available under a Creative Commons Attribution Non-Commercial No Derivatives licence. Researchers are free to copy, distribute or transmit the thesis on the condition that they attribute it, that they do not use it for commercial purposes and that they do not alter, transform or build upon it. For any reuse or redistribution, researchers must make clear to others the licence terms of this work.

Abstract

This thesis describes atomic physics experiments performed using a microfabricated photonic waveguide chip: a device that enables the interaction of cold atoms with an array of 12 microscopic light beams emitted by optical waveguides, inside a microscopic trench that has been cut into the chip, across all of the waveguides. The chip uses standard cold-atom control techniques along with readily available photonics technologies to provide an integrated atomic physics device that is not 'scalable' so much as already scaled.

We describe experiments where atoms are driven into the trench using magneto-optical traps and magnetic traps. In the latter case, the large, homogeneous magnetic field that is present during the atom-light interaction allows us to observe polarization-dependent effects in absorption signals from the trench.

Vacuum difficulties have limited the efficiency of rf-driven evaporative cooling in our magnetic trap to 0.4 (with a final phase-space density of 2×10^{-5}). To circumvent this issue, we have developed a novel evaporative cooling process, in which a dimple potential, comprised of an optical trap and a magnetic trap, is used to perform cycles of isentropic trap deformation and selective atom removal. Using this cooling process increases our evaporative cooling efficiency to 1.2. Various other cooling strategies that involve the dimple are also investigated. Using the dimple, we achieve a phase-space density of 0.04.

Having cooled the cloud using the dimple, we move it into the trench and measure absorption signals of 50%, much larger than those achieved previously. We investigate the possibility of producing microscopic optical dipole traps in the trench by sending red-detuned light through the waveguides, and show results of preliminary experiments looking at light shifts.

Acknowledgements

Getting this far would not have been possible without the guidance and support of Rob Nyman, a postdoc who acted more like a second supervisor, even after starting his own experiment. Thanks also to my main supervisor, Ed Hinds, for giving me the opportunity to work on the project and for our regular discussions about the science. I'm grateful for the contribution of everyone who worked on the experiment over the years; Matthias Kohnen, Plamen Petrov, and Camille Frapolli.

I'd also like to thank Jon Dyne and Steve Maine for building many of the components of the experiment, Valerijus Gerulis for his help with the endless electronics problems, and Sanja Maricic for her help with the endless administrative work.

Thanks to the rest of CCM for making the lab a friendly and supportive working environment. Thanks also to all the people I've shared an office with, in vaguely chronological order; Alex, David, Steve, Sofia, the two Marcos, Jon, Emilio, Pete, and Felicity. The atmosphere was always friendly, if not always conducive to work!

Finally, I'd like to thank my family and non-work friends, and of course Bridgette, who supported me throughout and even read through this entire thesis checking for errors before I submitted it. So if there are any glaring errors remaining, they're entirely her fault.

Contents

1. Introduction

1.1. Atom chips

Atom chip research effectively began with the proposal of microfabricated particle mirrors that could reflect atomic or molecular beams. The first such mirror was demonstrated by Roach *et al.* in 1995, who observed cooled rubidium atoms reflecting off the periodic magnetic structure generated by recording sinusoidal signals onto a magnetic audio-tape[1]. Similar results were achieved in subsequent experiments with permanent periodic magnetic structures by Sidorov *et al.*[2], Hughes *et al.*[3] and Lau *et al.*[4].

The use of miniaturized permanent magnetic structures to trap and manipulate cold atoms was investigated by Vuletic *et al.* in 1998[5]. While the field provided by a permanent structure can be altered to an extent by changing the bias fields, much greater flexibility can be achieved by replacing the permanent magnets with current carriers. This was demonstrated in 1998 by Fortágh, Grossman, Zimmermann and Hänsch, who used two adjacent wires of different thicknesses to generate a long and thin region of low magnetic field, which was then able to capture and confine cold atoms that had been released from a nearby free-space magnetic trap[6]. Müller *et al.* demonstrated that the magnetic field from a pair of current-carrying wires could be used to a form an 'atom waveguide', which guided cold atoms along a curved path[7]. Similar techniques were investigated by Denschlag *et al.*, who have examined the possibility of guiding atoms in high-field-seeking states[8].

In 1999 Reichel *et al.* realized the first true 'atom chip' (although the term was not coined until a similar experiment in 2000[9]), trapping atoms using microfabricated conductors on a substrate surface, with the addition of a reflective silver coating to allow for a mirror MOT from which atoms are loaded into the magnetic trap[10]. The mirror MOT configuration helps to avoid problems with optical access.

The magnetic traps that can be produced with atom chips can be generated with very high trapping frequencies due to the proximity of the trap centre to the conductors. High frequency traps can produce high interatomic elastic collision rates in trapped atom clouds, allowing for rapid, high efficiency evaporative cooling, which can be used to cool a trapped atom cloud to degeneracy[11, 12]. This makes atom chips ideal for experiments with Bose-Einstein condensates (BECs). Condensates produced using atom chips were achieved in 2001 by the groups of Ott *et al.*[13] and Hänsel *et al.*[14], followed by the groups of Schmiedmayer[15], Zimmermann[16] and Hinds[17, 18]. Aubin *et al.* succeeded in loading a degenerate Fermi gas of ^{40}K atoms into an atom chip magnetic trap, by sympathetic cooling with ultra-cold ^{87}Rb atoms[19].

More generally, atom chips can be used to develop integrated, scalable cold atom systems that have a varety of potential applications, such as miniaturized atom interferometers[20, 21] and devices for quantum information processing[22, 23]. There is also growing interest in the intersection of cryogenics with atom chips, with several groups using atom traps with integrated superconducting wires[24], which offer the prospect of extremely low noise environments and, potentially, coupled systems of BECs and superconducting loops[25].

1.1.1. Photonic atom chips

Cavities on chips

An important feature for any cold atom experiment is a sensitive atom detection system. We can further miniaturize atom chip systems, and make them more self-contained, by integrating such detectors onto the chip. In fact, miniaturizing the detectors can dramatically increase their sensitivity; as shown in [26], microfabricated optical cavities can allow for single-atom detection in the cavity mode, either by a measurable increase in the absorption of resonant light or by a measurable phase shift of off-resonant light. To investigate this, Eriksson *et al.*[27, 28] constructed an array of optical microcavities, formed by the plane tip of an optical fibre (coated for reflectivity) and 100 μm-diameter concave micromirrors. The micromirrors consisted of hollows that had been etched into a silicon substrate and then covered with a 100 nm layer of gold to give a reflective surface. By dropping a cold atom cloud through the cavity, the system was capable of detecting less than one atom, on average[29, 30]. The authors note that the cavity does not need to have a particularly high finesse if the beam waist is sufficiently small, as corroborated in a similar experiment by Haase *et al.*[31]. Other groups have demonstrated atom detection via fluorescence measurements in microcavities[32], and optical atom traps in microcavities[33].

Microscopic beams

Although the enhanced atom-light coupling in cavities naturally provides sensitive detection, we can build atom detectors that forgo the cavity entirely, and rely solely on a small beam size. The effectiveness of small beams of resonant light to perform measurements on atom clouds can be shown using some simple physics. If a beam of initial power P_0 is directed through an atomic sample, the power of the beam a distance l into the sample is given by the Beers-Lambert law;

$$P = P_0 \exp(-\alpha l), \tag{1.1}$$

where α is the absorption coefficient of the atomic sample, given by

$$\alpha = n\sigma_{\text{abs}}, \tag{1.2}$$

where n is the number density of the atoms and σ_{abs} is their absorption cross section. If the light is resonant with an atomic electric-dipole transition of wavelength λ and its intensity is much less than the saturation intensity of the transition, σ_{abs} can be as much as

$$\sigma_{\text{abs}} = \frac{3\lambda^2}{2\pi}. \tag{1.3}$$

Assuming the light field and atomic density are uniform in space $n = N_{\text{a}}/V$, where N_{a} is the number of atoms and V is the mode volume of the beam, equal to lA where A is the cross-sectional area of the beam. We therefore have

$$\alpha = N_{\text{a}}\frac{\sigma_{\text{abs}}}{A}, \tag{1.4}$$

indicating large α can be obtained with relatively small N_a when $A \approx \sigma_\mathrm{abs}$. As a result, if the absorption of a microscopic beam can be accurately measured through a sample of atoms, the number of atoms in the mode can be determined very precisely, even down to very low numbers.

Eriksson *et al.*[27] discusses a potential detector that makes use of this effect. Two fibres are positioned inside V-grooves on a chip, facing each other. The fibres taper a few hundred micrometers from their tips, giving a curved surface at the tip that focuses light leaving the fibre to a waist of 2.8 μm. This setup should give absorption signals of around 5% when a single rubidium atom is in the beam. Two facing optical fibres attached to an atom chip were used by Quinto-Su *et al.* to send a 31 μm-waist beam through a cloud of cold caesium atoms[34], measuring the linewidth of the Cs D_2 line at different laser intensities. Tey *et al.* have demonstrated a single trapped atom producing a 13% absorption signal, using a laser focused to a waist of around 860 nm[35]. Several groups have investigated the use of fibres attached to chips to perform local measurements of the fluorescence emitted by a cold atom cloud[36, 37, 38, 39] — in some cases experimentally demonstrating single-atom sensitivity.

In general, these fibre chips are not as easily scalable as the microcavity structures, due to the fine alignment needed to get fibre-to-fibre coupling and the difficulties encountered in attaching fibres to chips[38].

1.2. Our waveguide chip

Our photonic chip, detailed in the next chapter, is the first device to use an array of microfabricated optical waveguides to both deliver microscopic light beams to cold clouds of rubidium-87 atoms and receive light from the atoms, creating an array of potential interaction regions, or 'atom-photon junctions'. These junctions allow for the investigation and exploitation of the aforementioned benefits of using microscopic beams. The beams that propagate in the waveguides have a $1/e^2$ intensity radius of 2.2 μm, giving them a mode area of comparable size to the atomic absorption cross section of the D_2 line of rubidium-87, which following equation (1.3) is around 0.3 $\mu\mathrm{m}^2$, given the 780 nm transition wavelength. Therefore the expression $N_\mathrm{a}\sigma_\mathrm{abs}/A$ from equation (1.4) evaluates to $0.02N_\mathrm{a}$ for this system, suggesting that we should be able to obtain around 2% absorption when a single atom is in the beam mode.

We measure this absorption by cutting a microscopic trench, 16 μm wide, through all 12 waveguides. Light coupled into one of the waveguides will be emitted as a 2.2 μm-waist beam into the trench. This beam then crosses the trench and couples into the corresponding waveguide on the opposite side of the trench with 85% efficiency. We can therefore place atoms in the beam mode by moving trapped clouds into the trench.

The use of microfabricated waveguides written into the chip allows for far more scalability in our photonic chip than is feasible with the fibre chips discussed above. This makes it ideal for potential applications in quantum information processing[40].

1.3. Evaporative Cooling strategies

Preparing a cloud of rubidium atoms to interact with the microscopic beams on our chip requires cooling the cloud to temperatures the order of 1 μK. The 10^{-9} mbar vacuum pressure of our chamber means we cannot cool the cloud efficiently using standard evaporative cooling processes (such as rf-driven evaporation in a magnetic trap), so we have developed an alternative cooling strategy based on the addition of an optical 'dimple' trap to our magnetic trap.

Dimple potentials have been investigated by several other groups. Following the 1996 work of Pinkse *et al.*[41], in 1998 Wolfgang Ketterle's group demonstrated a way to cross the BEC transition in a reversible manner, by adiabatically deforming their trapping potential to include a small dimple region of lower potential[42]. This was shown to lead to a local increase in phase space density (to an arbitrarily large degree, in principle) and with an appropriate dimple depth could produce a condensate. The trap deformation was achieved by overlapping an attractive optical dipole trap with a magnetic trap. Garrett *et al.* have used a similar setup to produce a BEC in a dimple without evaporative cooling, permitting study of non-equilibrium condensate formation dynamics[43].

Basic single-beam optical dipole traps are not ideal for efficient evaporative cooling, as decreasing the trap depth by ramping down the beam power entails decreasing the collision rate of the trap. Several groups have implemented dimple potentials as a means to circumvent this issue. In

Innsbruck, Weber *et al.* have used a dimple to create a cesium BEC[44, 45], starting with a large atomic reservoir in a weakly confining crossed-beam trap. Following some evaporative cooling down to around 1 μK (aided by exploitation of a Feshbach resonance to increase the scattering length), the trap was then intersected with a tightly focussed beam, creating a smaller cigar-shaped dimple potential. The dimple beam was ramped on over several seconds to ensure an adiabatic trap deformation, and captured around 10% of the atoms, increasing the phase space density by a factor of 10. The loading of the dimple trap significantly increases the collision rate, allowing the remaining atoms to be efficiently evaporatively cooled.

Similar all-optical techniques have been used by Beaufils *et al.* to create a chromium BEC[46], and by Jacob *et al.* to create a sodium BEC[47]. Jacob *et al.* note that a relatively short evaporative cooling process applied to their atomic reservoir rapidly loaded almost all of the atoms into the dimple. Following the work of the Innsbruck group, Ma *et al.* have investigated evaporative cooling dynamics for cesium in all-optical dimple potentials using a numerical simulation [48, 49].

Dimple potentials have also been implemented in magnetic traps on atom-chips. Proukakis *et al.* have suggested and modelled a chip with a Z wire structure (as on our experiment) with an additional nano-fabricated 'dimple wire' crossing the central strut of the Z in the centre[50]. The magnetic field produced by current through the dimple wire can generate a deep, attractive dimple potential inside the Z wire potential. This potential could then be used to examine the growth dynamics for 1-D quasicondensates, with potential applications for atom lasers and atom interferometers. The authors also suggest creating an on-chip dimple using the electrostatic forces generated by an electrode of similar dimensions to the dimple wire placed close to the Z wire. They briefly consider the creation of such a dimple with a dipole trap, noting the danger posed by the scatter of trapping light off the chip surface, which has the potential to distort the trap.

Using a wire structure similar to that suggested in [50], Horikoshi *et al.* have developed an atom chip based method for fast BEC production[51]. One significant benefit of using an all-magnetic approach is that rf evaporation can be used throughout, allowing efficient three-dimensional evaporation inside and outside the dimple. The very high densities produced in the dimple region do however result in high three-body collision loss rates towards the end of the evaporation ramp - mitigated here by relaxation of the trapping potential. The authors specifically note that the high rate of evaporative cooling in their technique lessens the need for ultra-high vacuum.

Lin *et al.* have demonstrated production of a rubidium BEC using a combination of optical and magnetic traps[52], loading a quadrupole magnetic trap and ramping on an optical dipole trap (slightly offset from the trap centre) once the atoms in the magnetic trap are cool enough for Majorana spin flips to become a significant source of atom loss. As the atoms adiabatically load from the linear quadrupole trap into the harmonic dipole trap, the phase space density increases. Once the atoms have been loaded into the dipole trap, the magnetic fields are ramped down to zero and the remaining atoms are cooled in the now purely optical trap.

Comparat *et al.* have presented a theoretical study of evaporative cooling using a dimple, focussing on the dimple potential being added to the system non-adiabatically[53]. This results in heating as the atoms rethermalize into the dimple, but the authors argue that the heating rate is only marginally higher compared to that brought about by an adiabatically introduced dimple, and that the non-adiabatic regime is ultimately preferable as the loading occurs faster. The authors find that small and deep dimple potentials are good for maximising loaded atom number and phase space density, and a characteristic loading time for the dimple is derived based on the probability of an atom losing sufficient energy through collisions to be captured by the dimple. This time is typically a few collision lifetimes of the atoms in the reservoir. The authors suggest a strategy for evaporative cooling of cesium with a dimple potential, although their strategy focuses on methods to avoid issues with cesium cooling[1] that are generally not encountered with rubidium.

1.4. Content of this Thesis

When I started work on the waveguide chip experiment in October 2010, the waveguide chip had been installed in a vacuum chamber, and absorption

---

[1] Such as excessive two-body and three-body losses, which the authors suggest can be mitigated by ramping the size of the dimple potential. Weber *et al.* avoided these issues by trapping atoms in the absolute ground state ($F = 3, m_{\mathrm{F}} = +3$), which eliminates 2-body inelastic decay.

signals had been measured that indicated the presence of ^{87}Rb atoms inside the trench. These signals were produced by moving an atom cloud held in a magneto-optical trap into the chip. This work has been covered by the theses of Matthias Kohnen[54] and Manuel Succo[55].

Chapter 2 of this thesis gives details of our waveguide chip and its fabrication, along with a description of the copper substructure that enables magnetic trapping near the chip and a brief look at waveguide physics. Chapter 3 covers the rest of the experimental apparatus; the laser setup, characterisation of the magnetic fields generated by the copper substructure, and the vacuum setup. Our attempts to improve our vacuum pressure are also covered in this chapter. Chapter 4 covers the initial experiments in moving atoms into the trench, firstly with atoms from a magneto-optical trap, and then with atoms from a magnetic trap. Chapter 5 describes our attempts to efficiently cool trapped atom clouds, initially with rf radiation and then by the introduction of an opto-magnetic dimple potential. Chapter 6 returns the focus to the trench and waveguides, introducing the cold clouds obtained with the dimple potential into the trench, and looking at the possibility of generating in-trench optical dipole forces using red-detuned light in the waveguides.

1.5. Coordinate System

As the work in this thesis centers around the waveguide chip, it makes sense to use a coordinate system based on the structure of the chip. Figure 1.1 shows a simplified diagram of the chip. We define the z axis as being parallel to the long axis of the trench. The x axis is parallel to the waveguides at the trench, and the y axis is normal to the chip surface. The chip is oriented horizontally, so that gravity acts only in y. This coordinate system is used throughout the thesis.

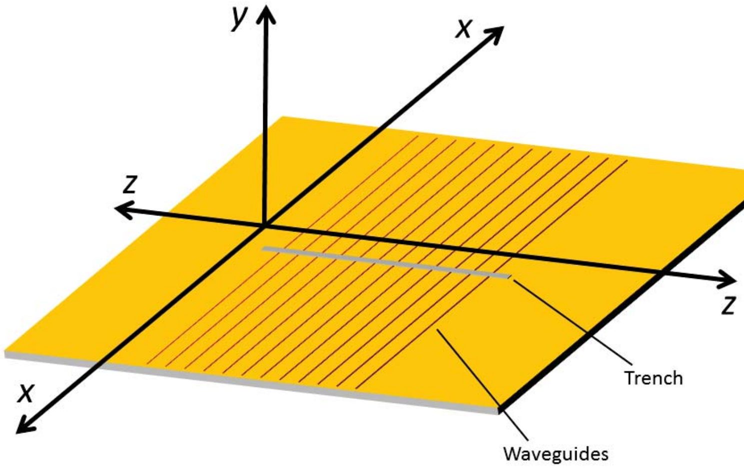

Figure 1.1.: A simplified diagram of the central region of our waveguide chip, showing the coordinate system used throughout this thesis.

2. The Waveguide Chip

This chapter covers the design and fabrication of the waveguide chip, and the subchip structures attached to it. Some basic waveguide physics is also discussed and the intensity distribution of the fundamental mode in our waveguides is determined.

2.1. Design and Construction

The waveguide chip consists of a 3 cm × 3 cm silicon substrate, 500 μm thick, with a 22 μm layer of silica deposited on top using flame hydrolysis. 10 μm beneath the surface of the silica, 12 optical waveguides have been written by doping regions of the silica with germanium and boron, providing a 0.75% higher refractive index than the surrounding silica, which has a refractive index of 1.47.

A diagram showing the position of the waveguides on the chip is shown in Figure 2.1. The waveguides have a centre-centre separation of 10 μm at the trench and have a square 4μm × 4μm cross section, and fan out towards the edges of the chip to allow for optical fibres to be connected to each waveguide using a V-groove structure. On top of the silica layer there is a coating consisting of a 50 nm thick layer of chromium (needed for bonding) and a 100 nm thick layer of gold, providing a reflective surface layer. The photonics for the waveguide chip were manufactured at the Centre for Integrated Photonics (CIP) in Ipswich, UK.

At the centre of the chip, a trench has been cut into the surface using deep reactive ion etching. The trench is 22 μm deep, 16 μm across and 500 μm long, oriented perpendicular to the waveguides so that all 12 are intersected. Light coupled into the waveguides on one side of the chip must therefore propagate across the trench before it can be collected by the optical fibres connected to the other side of the chip.

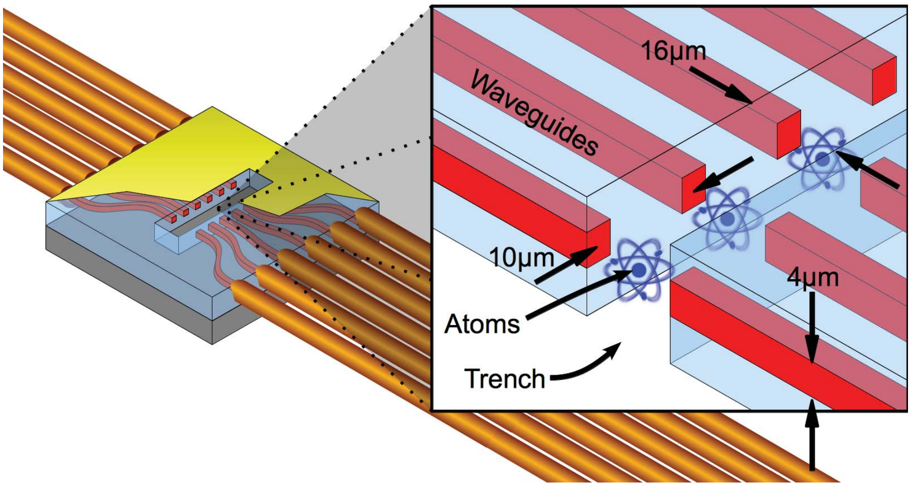

Figure 2.1.: A simplified diagram of the waveguide chip. Optical fibres (gold) couple light into the waveguides (red), which get closer together as they approach the trench. Diagram taken from [55].

Cold atom clouds moved into this trench can therefore be measured and manipulated by microscopic light beams entering and exiting the trench via the waveguides. To achieve this, we need to be able to produce cold atom clouds and have some means of moving them precisely into the trench. To achieve this, the waveguide chip is supplemented by a 'subchip' just below the silicon substrate. Figure 2.2 shows an exploded diagram of the full chip setup as it is installed in the vacuum chamber.

The subchip is a collection of millimeter-scale shaped copper wires that, given the appropriate current configurations, are able to generate tunable magnetic trapping potentials close to the surface of the photonic chip, suitable for moving clouds into the trench. The thickness of the silicon substrate sets a minimum separation between trap centre and wire structure, with the result that high currents must be used if trap frequencies the order of 100 Hz are to be obtained in the vicinity of the trench. To prevent the resistive heat dissipated in the wires from posing a threat to the glue securing the V-grooves in place, we fix the wires to a layer of Shapal which is in turn fixed to a large copper heatsink, using thermally conductive Epotek H74 epoxy adhesive. The Shapal layer provides electrical insulation between the wires and the rest of the setup. The subchip wires also have large cross

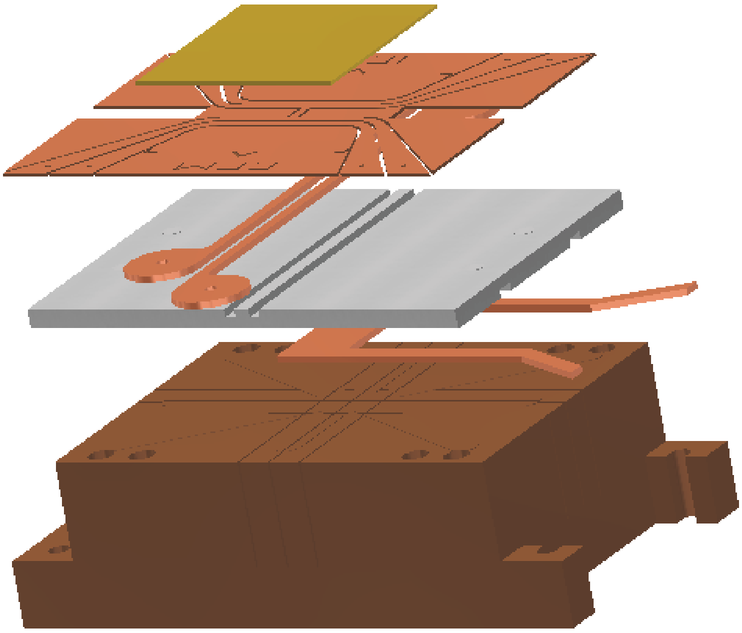

Figure 2.2.: An exploded diagram of the full chip setup mounted inside the vacuum chamber, showing, from top to bottom: the waveguide chip, the subchip wire structure (used to generate magnetic trapping fields near the chip), two ribbon wires (which, carrying the same current, generate a mostly uniform field near the centre of the waveguide chip), a layer of Shapal for electrical insulation, a U-shaped plate (used to generate a quadrupole field near the chip, which we use for magneto-optical trapping) and the copper heatsink. Diagram taken from [54].

sectional areas to reduce resistance. There is also a U-shaped plate fixed to the heatsink, which is used to generate a quadrupole field near the chip for a magneto-optical trap. Further details of the subchip structure and magnetic trapping in general are provided in Chapter 3.

2.2. Propagation of Light in Optical Waveguides

The physics of waveguide operation can be described by considering the wave equation of an electromagnetic wave propagating through a medium;

$$\nabla^2 \mathbf{E}(\mathbf{r}, t) - \frac{n^2(\mathbf{r})}{c^2} \frac{\partial^2 \mathbf{E}(\mathbf{r}, t)}{\partial t^2} = 0, \tag{2.1}$$

where $\mathbf{E}(\mathbf{r}, t)$ is the electric field strength and $n(\mathbf{r})$ is the refractive index of the medium. As the magnetic field strength is governed by the same wave equation, only the electric field will be considered here for simplicity - the magnetic field can be derived from the electric field using $\nabla \times \mathbf{E}(\mathbf{r}) = -\frac{\partial \mathbf{B}(\mathbf{r})}{\partial t}$. In the steady state the time dependence of the field can be separated out such that $\mathbf{E}(\mathbf{r}, t) = \mathbf{E}(\mathbf{r})e^{i\omega t}$, reducing equation (2.1) to the Helmholtz equation

$$\nabla^2 \mathbf{E}(\mathbf{r}) + k^2 n^2(\mathbf{r}) \mathbf{E}(\mathbf{r}) = 0, \tag{2.2}$$

where $k = \omega / c$ is the wave number of the radiation. If the radiation propagates in x, $\mathbf{E}(\mathbf{r})$ can be written

$$E(\mathbf{r}) = \mathbf{E}(y, z) e^{i k_{\mathrm{x}} x}, \tag{2.3}$$

so that

$$\nabla^2 \mathbf{E}(y, z) + (k^2 n^2(y, z) - k_{\mathrm{x}}^2) \mathbf{E}(y, z) = 0. \tag{2.4}$$

As stated, a waveguide can be constructed by increasing the refractive index $n(y, z)$ inside a thin channel. However, the mathematics of the system can be greatly simplified by reducing the channel waveguide to a 'slab' waveguide, where the refractive index varies in only one dimension. Setting this dimension to y and taking the wave to be polarised in z so that $\mathbf{E} = E\mathbf{z}$, and denoting the refractive indices inside and outside the waveguide by n_{I}

and n_{O} respectively gives equations for E inside and outside:

$$\frac{d^2}{dy^2}E(y) + (k^2 n_{\mathrm{I}}^2 - k_{\mathrm{x}}^2)E(y) = 0 \text{ for } |y| \leq \frac{d}{2} \tag{2.5}$$

$$\frac{d^2}{dy^2}E(y) + (k^2 n_{\mathrm{O}}^2 - k_{\mathrm{x}}^2)E(y) = 0 \text{ for } |y| > \frac{d}{2} \tag{2.6}$$

where d is the width of the waveguide. For the solutions to be physical the field must vary sinusoidally inside the waveguide channel and exponentially decay outside. This is why the refractive index inside the waveguide must be greater - for a sinusoidal solution kn must be greater than k_{x}, and for an exponential solution kn must be less than k_{x}. Therefore, n_{I} must be greater than n_{O}. Setting $\alpha^2 = k_{\mathrm{x}}^2 - k^2 n_{\mathrm{O}}^2$ and $\beta^2 = k^2 n_{\mathrm{I}}^2 - k_{\mathrm{x}}^2$, the solutions to equations (2.5) and (2.6) can be written

$$E(y) = A\cos(\beta y) + B\sin(\beta y) \text{ for } |y| \leq \frac{d}{2} \tag{2.7}$$

$$E(y) = Ce^{-\alpha|y|} \text{ for } |y| > \frac{d}{2} \tag{2.8}$$

where A, B and C are constants. As the refractive index layers are symmetric in y, the solutions for $E(y)$ must be either symmetric or antisymmetric. Examining first the symmetric modes where $B = 0$, the solutions will be continuous in values and derivatives only if $A\cos(\beta d/2) = C\exp(-\alpha d/2)$ and $A\beta\sin(\beta d/2) = C\alpha\exp(-\alpha d/2)$. Combining these two expressions gives

$$\alpha = \beta\tan(\beta d/2), \tag{2.9}$$

and substituting for k_{x} in the definitions of α and β gives

$$\alpha = \sqrt{k^2(n_{\mathrm{I}}^2 - n_{\mathrm{O}}^2) - \beta^2}. \tag{2.10}$$

As a result, β can only take discrete values, determined by the transcendental equation

$$\beta\tan(\beta d/2) = \sqrt{k^2(n_{\mathrm{I}}^2 - n_{\mathrm{O}}^2) - \beta^2}. \tag{2.11}$$

A similar line of reasoning gives the equivalent for the antisymmetric modes;

$$-\beta \cot(\beta d/2) = \sqrt{k^2(n_\mathrm{I}^2 - n_\mathrm{O}^2) - \beta^2}. \tag{2.12}$$

The right hand sides of equations (2.11) and (2.12) show that for confined modes β cannot exceed $k\sqrt{n_\mathrm{I}^2 - n_\mathrm{O}^2}$ - at this point the solutions for α become complex and the waveguide enters a 'radiation mode' where total internal reflection no longer works and the wave is not confined. This sets an upper limit on the number of modes that can be supported by the waveguide. The number of symmetric modes can be determined by noting that $\beta \tan(\beta d/2)$ increases monotonically with β, therefore each zero crossing point corresponds to one intersection with $\sqrt{k^2(n_\mathrm{I}^2 - n_\mathrm{O}^2) - \beta^2}$. Zero crossings in $\tan(\beta d/2)$ occur with a period of $2\pi/d$, therefore the upper bound to the number of symmetric solutions N_s is given by

$$N_\mathrm{s} \leq 1 + \frac{k\sqrt{n_\mathrm{I}^2 - n_\mathrm{O}^2}}{2\pi/d} = 1 + \frac{d}{\lambda}\sqrt{n_\mathrm{I}^2 - n_\mathrm{O}^2}. \tag{2.13}$$

The first zero crossing of $-\beta \cot(\beta d/2)$ occurs at $\beta = \pi/d$, so the upper bound to the number of antisymmetric solutions N_a is given by

$$N_\mathrm{a} \leq 1 + \frac{k\sqrt{n_\mathrm{I}^2 - n_\mathrm{O}^2} - \pi/d}{2\pi/d} = \frac{1}{2} + \frac{d}{\lambda}\sqrt{n_\mathrm{I}^2 - n_\mathrm{O}^2}. \tag{2.14}$$

Equation (2.14) shows that if $\frac{d}{\lambda}\sqrt{n_\mathrm{I}^2 - n_\mathrm{O}^2} < \frac{1}{2}$ the waveguide does not support any antisymmetric modes. However, following equation (2.13) the waveguide must always support at least one symmetric mode, in the form of the fundamental mode.

For the waveguides used in this experiment, d is 4 μm, n_O is 1.47, λ is 780 nm and n_I is 0.75% larger than n_O. Plugging these numbers into the equations given above suggests that the waveguide supports two modes, one symmetric and one antisymmetric. The values of α and β for the fundamental mode can be found by numerically solving equation 2.12, giving 1.4×10^6 m^{-1} and 5.9×10^5 m^{-1} respectively. Using these values in equations (2.7) and (2.8) gives the intensity distribution (equal to $\epsilon_0 c|E|^2$) shown in red in Figure 2.3b.

The slab model is attractively straightforward, but we can obtain a slightly more accurate picture by considering the problem in 2 dimensions and solving equation 2.4 numerically. This can be done by expanding the electric field into a Fourier series, using the modified Fourier decomposition method demonstrated by Hewlett and Ladouceur[56]. This method allows us to accurately account for boundary conditions at infinity by mapping the infinite $z - y$ plane onto the unit square, using the transformation

$$z = a_{\mathrm{z}} \tan\left[\pi\left(u - \frac{1}{2}\right)\right], \tag{2.15}$$

with some constant a_{z} and a similar transformation for y and v. Plugging a series expansion in terms of u and v into equation 2.4 turns the differential equation into an eigenvalue problem, which can be solved using standard techniques[57]. The intensity profile of the fundamental waveguide mode found using the modified Fourier decomposition method is shown in Figure 2.3a, and compared with the slab model results and a Gaussian fit in Figure 2.3b. The intensity profile of the mode closely resembles a Gaussian profile with a $1/e^2$ radius of 2.17 μm.

The intensity profile has been measured experimentally[54], using a CCD camera to measure the profile of the beam that exits the waveguide in the far-field and extrapolating back to find the shape of the profile in the waveguide. These measurements suggest a $1/e^2$ radius of 2.2 ± 0.1 μm, in agreement with the results from the calculations.

Modelling the waveguide mode as a Gaussian beam allows for simpler calculations of quantities such as the transmission across the trench after the beam has exited a waveguide, which can be determined by finding the mode overlap at the opposite waveguide after the beam has propagated through the 16 μm gap. The curvature of the wave front must be taken into account in this calculation, which ultimately suggests a transmission of 85%.

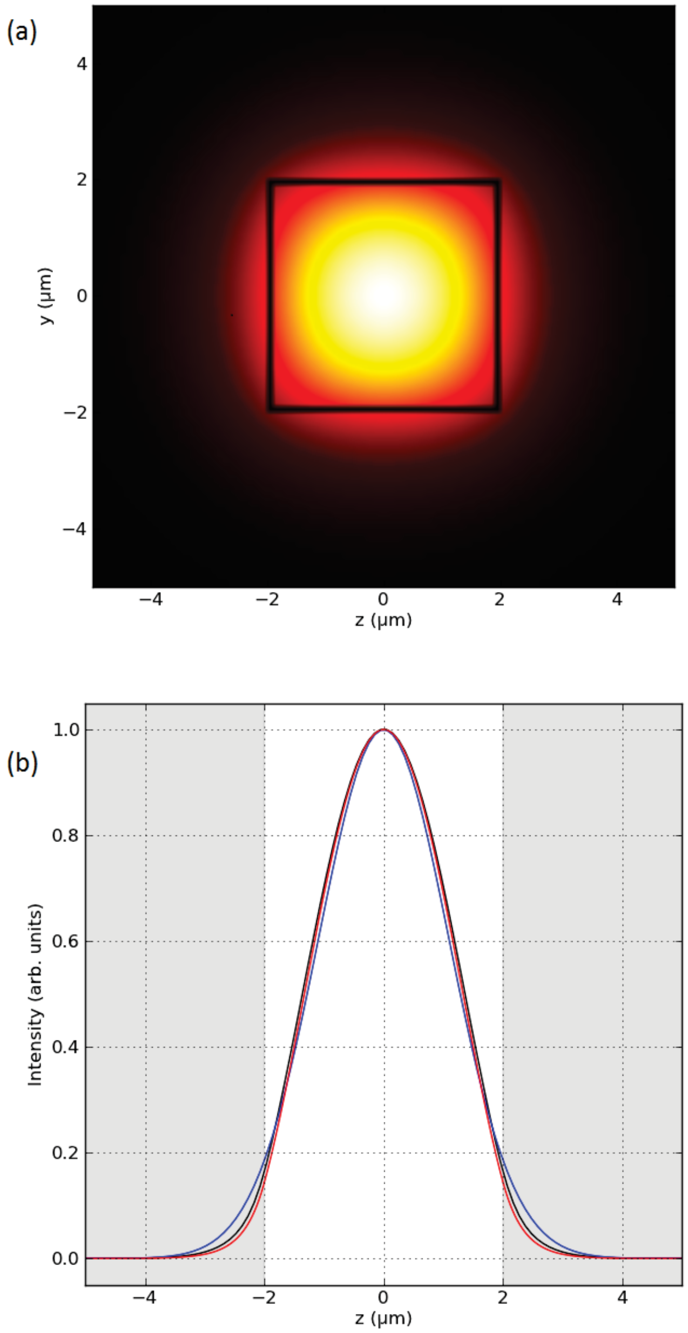

Figure 2.3.: (a) The intensity profile of the fundamental waveguide mode as found using the modified Fourier decomposition method. (b) The intensity profile in z (at $y = 0$) as found using the slab model (red) and the modified Fourier decomposition method (black). A Gaussian fit (blue) to the MFDM intensity profile has a $1/e^2$ radius of 2.17 μm.

3. Experimental Setup

This chapter covers the experimental apparatus we use to generate cold atom clouds to interact with the waveguide chip. The basic principles of magneto-optical trapping are covered, followed by a description of the laser setup we use to generate magneto-optical traps near the chip. We then describe magnetic trapping on the chip, the vacuum setup, and our attempts to improve the pressure in our main vacuum chamber. Figure 3.1 shows a sketch of our experimental apparatus.

3.1. Magneto-Optical Trapping

The first stage of any experiment involving the waveguide chip is to capture a cloud of cold atoms in a magneto-optical trap (MOT). The atom species we use is rubidium-87, chosen for its simple energy level structure and the availability of laser diodes that have output wavelengths close to its D_2 line, around 780 nm.

Typically, free-space MOTs rely on 3 orthogonal pairs of counterpropagating, frequency-stabilised laser beams, intersecting at the central minimum of a quadrupole magnetic field. If the polarization of the beams is correctly configured, the light will drive transitions between the Zeeman states of atoms depending on their velocity and position relative to the intersection, confining and cooling them. The 'U-MOT' used in the waveguide chip experiment uses the reflective surface of the chip to reduce the required number of beam pairs to 2[58, 59, 15]. A quadrupole field is generated by passing a current of about 80 A through a U-shaped plate in the subchip, and adding a homogeneous bias field of about 17 G in the X direction, generated using a pair of Helmholtz coils external to the vacuum chamber. A diagram of our U-MOT is shown in Figure 3.2a.

The U-MOT is itself loaded with pre-cooled atoms from a low-velocity

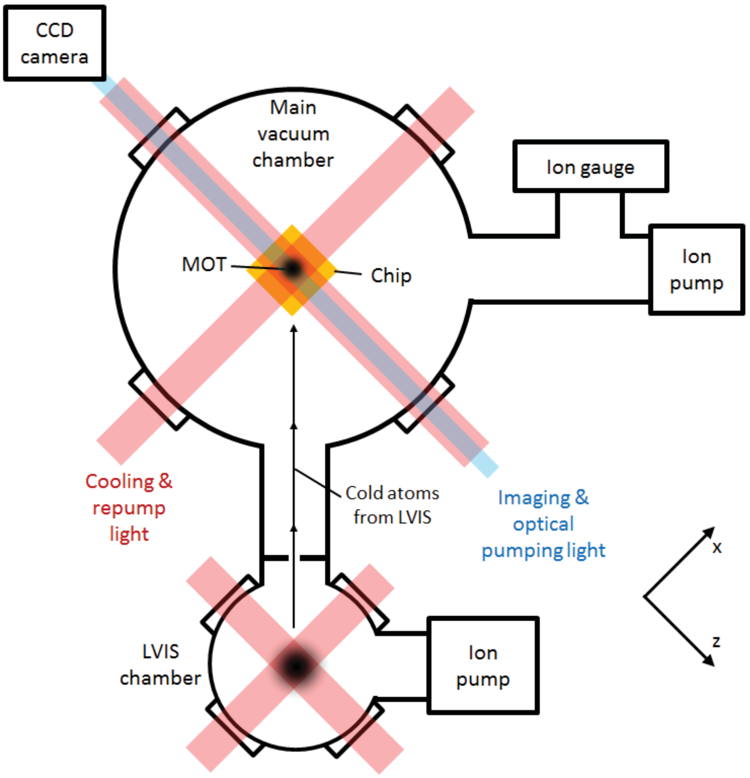

Figure 3.1.: A sketch of our experimental apparatus (as of October 2010) showing the vacuum chamber setup and the path of the cooling light and imaging light. The waveguide chip is mounted inside the main chamber, where we produce a magneto-optical trap (MOT) which captures atoms from a low-velocity intense source (LVIS). The LVIS is a second MOT with a hole in one of the mirrors so that a beam of cold atoms is pushed through into the main chamber.

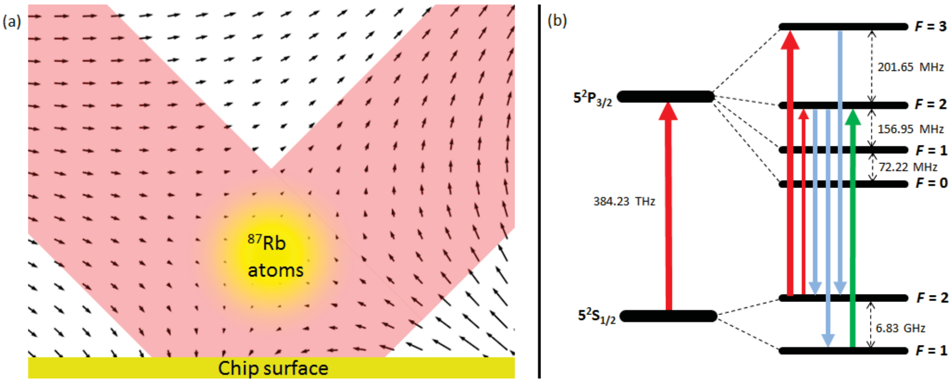

Figure 3.2.: (a) A cross-sectional diagram of our rubidium-87 U-MOT. The cooling and repump beams (red) intersect at the zero point of the magnetic field (black arrows) generated by the U plate and bias fields to produce a combined cooling and trapping force on the atoms (yellow). (b) Energy level diagram for the D_2 transition ($5^2S_{1/2} \to 5^2P_{3/2}$) of rubidium-87. The red arrow shows the cooling $F_\mathrm{g} = 2 \to F_\mathrm{e} = 3$ transition addressed using the reference and tapered amplifier lasers, with several possible decays shown in blue. The cooling lasers can also drive the $F_\mathrm{g} = 2 \to F_\mathrm{e} = 2$ transition, so we also need to use a repump laser, which drives the $F_\mathrm{g} = 1 \to F_\mathrm{e} = 2$ transition shown in green.

intense source (LVIS), in the form of a free-space MOT with a higher capture velocity that collects atoms emitted by alkali metal dispensers which have been subjected to resistive heating. The LVIS and dispensers are in a vacuum chamber separate to that of the U-MOT, connected by a small hole in one of the LVIS mirrors that allows transversely cold atoms to move from LVIS to U-MOT. With 3-7 A running through the dispensers and around 100 mW of total LVIS light power and 35 mW of total MOT light power, we load around 7×10^7 atoms into the U-MOT over 2 s of loading time, at a temperature of about 100 μK.

The lasers used to generate the two MOTs must therefore have a high enough output power while remaining stabilised close to atomic transition frequencies of the atoms being trapped. We use transitions in the hyperfine structure of the D_2 transition of rubidium-87, using $F_\mathrm{g} = 2 \to F_\mathrm{e} = 3$ as our cooling transition. The energy level structure of the D_2 line is shown in Figure 3.2b.

3.2. Laser Setup

This section describes the laser system used to produce a MOT and perform absorption imaging on the atoms, both in the trench and in the region close to the chip.

3.2.1. Cooling light

A schematic diagram of our laser setup is shown in Figure 3.3. To generate light stabilised at the frequency of the cooling transition, we use a home made extended cavity diode laser (ECDL)[60, 61] designed in Littrow configuration to bring the linewidth below 1 MHz, sufficiently small compared to the natural 6 MHz linewidth of the transition. This laser is locked to the cooling transition using polarization spectroscopy[62] and a standard locking circuit, and is then used to provide a reference for the cooling frequency.

The Reference Laser is used in conjunction with a commercial Toptica TA100 module, consisting of an 'DL100' ECDL with an output power of around 30 mW at a diode current of 90 mA, which is then amplified using a tapered amplifier chip driven at 2 A to give a final output power of around 400 mW. A 'monitor' beam is split off from the ECDL and split into two beams, one used for frequency monitoring via saturated absorption spectroscopy and the second overlapped with light from the reference laser. The beat between the two laser frequencies is detected on a RF photodiode and its frequency is compared to that of a tunable, local oscillator controlled by an external voltage. By altering this external voltage we can therefore control the difference in frequency between the lasers. Using a side-of-filter technique[63] we lock the TA100 frequency to about 80 MHz higher than the cooling transition frequency. The TA100 frequency is then shifted down towards the transition using an AOM. This system allows us to tune the laser frequency to the cooling frequency ±40 MHz. The frequency-stabilised 400 mW beam from the TA100 is split into 300 mW and 100 mW beams for the LVIS and MOT respectively. These beams are both passed through acousto-optic modulators to permit fast switching and then injected into single-mode, polarisation maintaining fibres which bring the light to the vacuum chamber, where they are further split into counterpropagating pairs. Injecting the light into fibres serves to improve the beam quality, as well

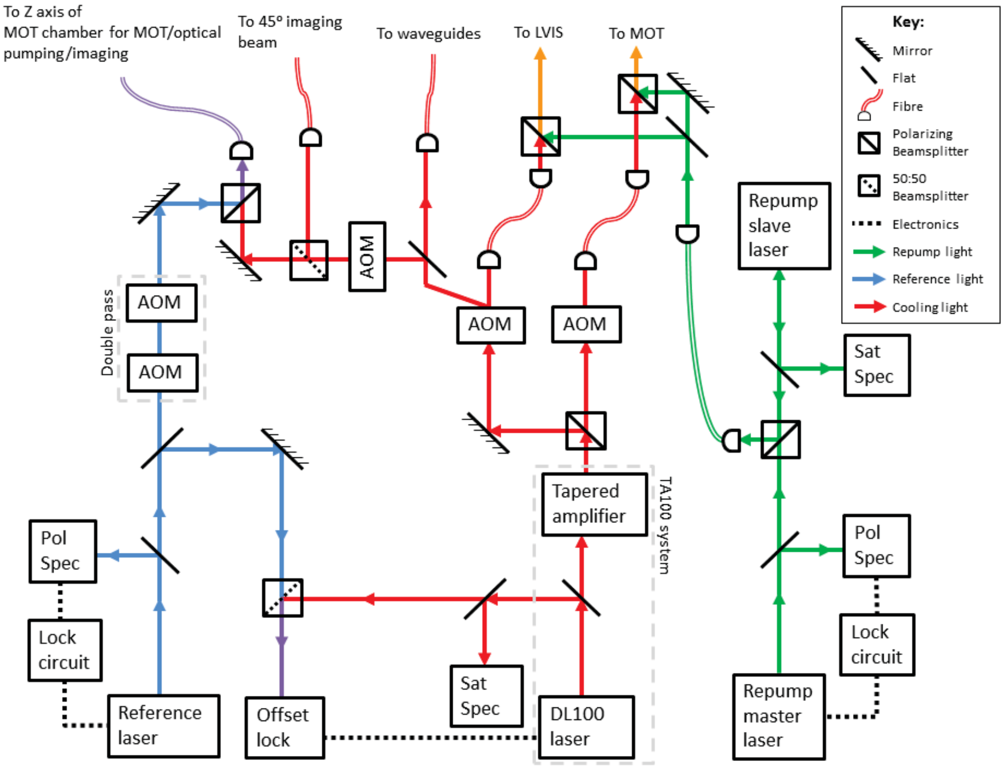

Figure 3.3.: Diagram of the laser setup for this experiment.

as decoupling the alignment of the TA100 output beam from that of the beams in the chamber. The shape of the beam before it is injected into the fibre is crucial to efficient injection, and is very sensitive to the alignment of the DL100 beam into the amplifier crystal. The alignment that produces the optimal beam shape does not coincide with the alignment that produces the highest overall TA100 output power, meaning a fine balance must be achieved between beam shape and power to ensure a high power is injected into the fibre.

3.2.2. Repump Light

As shown in Figure 3.2b, the cooling transition is not closed, as atoms can decay to the $F_g = 1$ state through inadvertent excitation of the $F_\mathrm{g} = 2 \rightarrow F_\mathrm{e} = 2$ transition, removing them from the cooling cycle and ultimately losing them from the MOT. This necessitates the addition of a second set of 'repump' beams resonant with the $F_\mathrm{g} = 1 \rightarrow F_\mathrm{e} = 2$ transition which pump atoms back into the cooling cycle if they escape. The repump light is generated by two ECDLs in a master-slave configuration. Using polarization spectroscopy, the master laser is locked to the $F_\mathrm{g} = 1 \rightarrow F_\mathrm{e} = 0, 1$ crossover transition, about 80 MHz above the repump transition, and is aligned directly into the slave laser diode (which is run at around 80 mA) to produce a beam of sufficient power. The slave laser light is then shifted down to the repump frequency using an AOM, before being injected into a fibre and finally split up into two beams of about 2 mW, which are overlapped with both MOT and LVIS beams at their fibre outputs.

3.2.3. Detection Light and Optical Pumping Light

To perform absorption imaging of atoms in the chamber and the trench, the unshifted zero order light from the LVIS beam's AOM is directed into another AOM which shifts it to the atomic resonance. This beam is then split into three beams, each of which is attenuated using a neutral density filter before being coupled into an optical fibre. One of these fibres is used to bring light to the optical fibres connected to the waveguide chip. Two bring light to the vacuum chamber, where they are expanded. One is directed through the vacuum chamber, oriented horizontally along the Z direction parallel to the chip surface. Upon leaving the vacuum chamber the beam is directed into a CCD camera. The other imaging beam is directed up at the chip in the X-Y plane, 45 degrees from the horizontal. After reflecting off the chip surface this beam is also measured using a CCD camera. By comparing the transmission measured on the CCD between two pulses, one with atoms trapped (or just released) and one 0.25 s after their release, we can map the optical density of the cloud and hence determine the number and distribution of atoms.

Optical pumping light is used to pump atoms into the $F_{\mathrm{g}} = 2$, $m_{\mathrm{F}} = +2$ Zeeman state suitable for magnetic trapping, through repeated cycles of σ^+ excitation and spontaneous decay. We achieve this using a homogeneous 'director' magnetic field and circularly polarised light resonant with the $F_{\mathrm{g}} = 2 \rightarrow F_{\mathrm{e}} = 2$ transition. The light is split off from the reference laser beam and directed through a double pass AOM to shift the frequency down by 246 MHz, at which point it is 20 MHz to the blue of the pumping transition (the blue detuning is necessary because of the Zeeman shift caused by the director field). The light is then injected into the fibre that carries the Z axis imaging light, overlapping the two beams as they enter the chamber.

3.3. Magnetic trapping

Magnetic traps confine atoms by making use of the Zeeman shift, caused by the interaction between an external magnetic field $\mathbf{B}(\mathbf{r})$ and the coupled magnetic moments of the atom's nucleus and electrons, giving rise to an interaction potential U_{int}:

$$U_{\mathrm{int}}(\mathbf{r}) = -\boldsymbol{\mu} \cdot \mathbf{B}(\mathbf{r}), \tag{3.1}$$

where $\boldsymbol{\mu}$ is the magnetic moment of the atom. Following this, an atom in hyperfine state $|F, m_{\mathrm{F}}\rangle$ has its energy level E_{F} shifted such that:

$$E_{\mathrm{F}}(\mathbf{r}) = E_{\mathrm{F},|\mathbf{B}|=0} + g_{\mathrm{F}}\mu_{\mathrm{B}}m_{\mathrm{F}}|\mathbf{B}(\mathbf{r})|, \tag{3.2}$$

where g_{F} is the Landé g-factor and μ_{B} is the Bohr magneton. As a result, the atom is subject to a force $\mathbf{F}$;

$$\mathbf{F}(\mathbf{r}) = -g_{\mathrm{F}}\mu_{\mathrm{B}}m_{\mathrm{F}}\nabla|\mathbf{B}(\mathbf{r})|. \tag{3.3}$$

Atoms with positive values of $g_\mathrm{F} m_\mathrm{F}$ are therefore attracted to regions of low $|\mathbf{B}|$, and atoms with negative $g_\mathrm{F} m_\mathrm{F}$ are attracted to high $|\mathbf{B}|$. However, static local maxima in $|\mathbf{B}|$ are impossible in free space regions where there are no electric currents, due to Earnshaw's Theorem[64]. Magnetic trapping is therefore exclusively achieved using 'low-field-seeking' atoms, with positive $g_\mathrm{F} m_\mathrm{F}$. The sign of the Landé g-factor g_F is determined by the hyperfine state of the atom, and the sign of the z component of the spin m_F can be set by optical pumping.

It is worth noting that equation (3.2) only holds when the Zeeman shift is small compared to the hyperfine splitting - in a strong magnetic field the coupling between the electronic and nuclear angular momentum is disrupted and the energy shift is no longer linear in $|\mathbf{B}(\mathbf{r})|$. For the experiments covered in this thesis, however, the weak-field approximation of the shift is sufficient.

There is a general problem encountered by all traps using a magnetic field minimum with low-field-seeking atoms. If there is a region where $|\mathbf{B}|$ is sufficiently small, the centre-of-mass oscillation frequency of the trap becomes comparable to the frequency at which the atom's magnetic moments precess about the direction of the magnetic field. In this situation the so-called 'adiabatic approximation' is violated, as the magnetic dipole is no longer aligned with the local field at all times. This allows the atom to undergo a Majorana spin-flip from a low-field-seeking state to a high-field-seeking state, resulting in its ejection from the trap. As a result, all magnetic trap experiments must either ensure that no regions of sufficiently low $|\mathbf{B}|$ are present, or take steps to ensure that no atom can reach the region of low $|\mathbf{B}|$ (this can be achieved by 'plugging' the low-$|\mathbf{B}|$ region with a blue-detuned laser beam that repulses the atoms[11], or by rapidly moving the trap so that the atoms experience a time-averaged potential with no points of zero $|\mathbf{B}|$[65]).

3.3.1. Two Magnetic Trap Geometries

The simplest form of magnetic trap is the quadrupole trap, which can be generated by a pair of Helmholtz coils with opposing currents. The field of a quadrupole in the vicinity of the trap minimum is given by

$$\mathbf{B} = B' \begin{pmatrix} x \\ y \\ -2z \end{pmatrix}, \tag{3.4}$$

where B' is the magnetic field gradient along the x and y axes (the gradient along z must be -2B' to satisfy $\boldsymbol{\nabla} \cdot \mathbf{B} = 0$), and the z axis coincides with the axis of the two coils and therefore constitutes an axis of cylindrical symmetry. Following this, the magnitude of the field varies as

$$|\mathbf{B}|^2 = \left(x^2 + y^2 + 4z^2\right)^{1/2}. \tag{3.5}$$

As a result the quadrupole trap is susceptible to Majorana spin flip losses, as $|\mathbf{B}| = 0$ at the centre of the trap.

The Ioffe trap is a static trap configuration that does not have a $|\mathbf{B}| = 0$ point. The standard macroscopic Ioffe trap uses two Helmholtz coils with parallel currents, along with four current-carriers arranged symmetrically around the axis of the coils, each carrying a current opposing that of its nearest two neighbours[66]. A diagram of the currents used in the Ioffe trap is shown in Figure 3.4. This configuration generates a cylindrically symmetric field, which near the centre of the trap is given by

$$\mathbf{B} = B_0 \begin{pmatrix} 1 \\ 0 \\ 0 \end{pmatrix} + B' \begin{pmatrix} 0 \\ -y \\ z \end{pmatrix} + \frac{B''}{2} \begin{pmatrix} x^2 - \frac{1}{2}\left(y^2 + z^2\right) \\ -xy \\ -xz \end{pmatrix}, \tag{3.6}$$

where x is the axis of the coils and B_0 is a bias field. For $x \ll \sqrt{\frac{B_0}{B'}}$ and y, $z \ll \frac{B_0}{B'}$ the magnitude can be approximated by

$$|\mathbf{B}| \approx B_0 + \frac{B''}{2} x^2 + \frac{1}{2} \left(\frac{B'^2}{B_0} - \frac{B''}{2} \right) r^2, \tag{3.7}$$

where $r^2 = y^2 + z^2$. The trap provides radial as well as axial harmonic confinement, and $|\mathbf{B}|$ is always greater than or equal to B_0, avoiding any point of zero field in the trap.

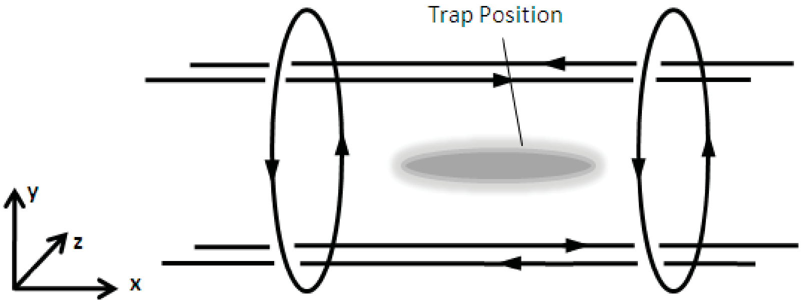

Figure 3.4.: A diagram of the currents needed to produce a Ioffe trap.

3.3.2. Microfabricated Magnetic Trapping Structures

Both quadrupole and Ioffe traps can be generated using planar wire layouts. The underlying principles of wire traps can be illustrated by considering the trap created by a single thin wire and a bias field. The field due to a wire oriented along the z axis is given by

$$\mathbf{B} = \frac{\mu_0 I}{2\pi}\frac{1}{x^2+y^2}\begin{pmatrix}-y\\ x\\ 0\end{pmatrix}. \tag{3.8}$$

A local minimum in $|\mathbf{B}|$ can be created if a uniform bias field is projected perpendicular to the wire such that

$$\mathbf{B} = \frac{\mu_0 I}{2\pi}\frac{1}{x^2+y^2}\begin{pmatrix}-y\\ x\\ 0\end{pmatrix} + B_{\mathrm{bias}}\begin{pmatrix}1\\ 0\\ 0\end{pmatrix}. \tag{3.9}$$

This has a point of zero field, which can be removed by adding a field B_{z} oriented in the z axis. The magnitude of the field is then given by

$$|\mathbf{B}|^2 = \frac{\mu_0 I}{2\pi}\frac{1}{x^2+y^2}\left(\left(\frac{2\pi\left(x^2+y^2\right)B_{\mathrm{bias}}}{\mu_0 I} - y\right)^2 + x^2\right) + B_{\mathrm{z}}^2. \tag{3.10}$$

This has a minimum in the xy plane at $x = 0$, $y = \mu_0 I/2\pi B_{\mathrm{bias}}$. This is effectively the potential used by Hänsch *et al.*[6] in their early wire trap experiment — a thicker wire generated a relatively uniform bias field across the field of a thinner wire, with axial confinement provided by a pair of coils. The resulting trap was found to be mostly cylindrically symmetric and resembled a Ioffe trap.

Alternatively, axial confinement can be integrated into the structure by bending the wire into a ‘U’ or ‘Z’ shape. These layouts are shown in Figure 3.5a. In both U and Z configurations axial confinement is provided by the wires positioned at the ends of the central wire. The symmetric U configuration generates a quadrupole field above the chip, centered on the axis of symmetry between the two end wires which generate opposing magnetic fields, as used for our MOT. The Z configuration generates a Ioffe trap, with a non-zero trap bottom at the centre due to the contribution from the two parallel end wires. The fields generated by the two trap configurations are shown in Figures 3.5b and 3.5c.

Equation (3.8) demonstrates one of the most significant advantages of atom chips over macroscopic trapping systems. The magnitude of the magnetic field of a single thin wire is given by $|\mathbf{B}| = \mu_0 I/2\pi r$ where $r^2 = x^2+y^2$, so the gradient varies as r^{-2} and the curvature varies as r^{-3}. This is how wire traps allow extremely high trap frequencies - as the bias field is increased relative to the wire field, and the trap centre approaches the wire, both the gradient and curvature grow rapidly.

While the trap’s proximity to the wire allows high trap frequencies it does introduce a potential problem - the shape of the trap is now strongly dependent on the direction and magnitude of the current in the wire. In practice, the wire can contain small defects[67, 68] (often due to the fabrication process), which can cause undesirable deviations in the direction of current flow. The contributions to the wire’s magnetic field caused by these deviations average out at larger distances but can introduce ‘corrugation’ into the potential when the trap is close to the wire[69]. This can cause the cloud to fragment, causing atom losses and preventing realization of some of the more elusive objects studied on atom chips, such as Tonks-Girardeau gases[70]. To prevent this, Trebbia *et al.* have employed a system reminiscent of the TOP trap[65], where rapid modulation of the wire current generates a time-averaged potential which can average out defects[71].

Following equation (3.8), the maximum confinement and trap-to-wire distance that can be achieved is dependent on the maximum current. This introduces a potential limitation of atom chips — at high currents excessive resistive heating can occur, heating up the wires and the surrounding com-

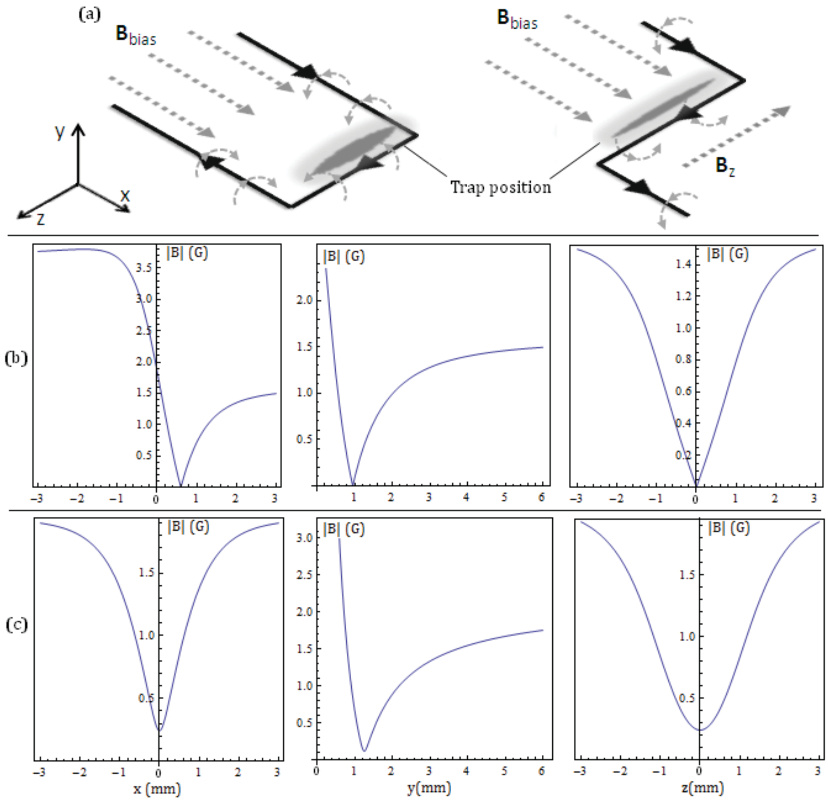

Figure 3.5.: (a) Wire layouts for the U and Z magnetic trap structures. In each case the trap is generated above the wire (in the +y direction). (b) and (c) show the shapes of the magnetic traps created with the U and Z wires respectively. In both cases the central strut of the wire lies on the z axis and is carrying a current of 50A, and $|B_{\mathrm{bias}}| = 50$ Gauss. For the Z wire $|B_{\mathrm{z}}| = 1$ Gauss, raising the trap bottom so there is no point of zero field and Majorana spin flips can be avoided.

ponents of the atom chip with potentially damaging results. The danger is exacerbated by the possibility of 'runaway' heating if the current exceeds a certain critical value - the resistivity of the wire increases with temperature, leading to more resistive heating and ultimately an exponential rise in temperature. As a result, the wires must either only be used at safely low currents, or be placed in thermal contact with a heatsink large enough to dissipate the heat faster than it can build up. The dangers of heating provide another reason to ensure the wire is fabricated to high quality and installed correctly - if there are defects in the wire or in its thermal contact with the heatsink, the wire will heat at that point faster than elsewhere and thus damage will occur at currents far below the predicted safe upper limit.

3.3.3. Magnetic Trapping on the Waveguide chip

Trap Structure

To fit a cylindrical cloud of trapped atoms into the trench of the waveguide chip, the wire structure includes a Z-shaped wire with the central strut parallel to the trench. With a pair of straight wires just beneath the main wire structure capable of generating a relatively uniform bias field near the chip, a Ioffe shape trap can be generated in the vicinity of the trench.

As stated in Chapter 2, high currents must be used to obtain trapping frequencies the order of 100 Hz near the trench. Running a current of approximately 50 A through both the bias and Z wires produces a trap around 0.5 mm above the trench (1 mm above the Z wire). By applying a bias field parallel to the long axis of the trap we can control the trap bottom and radial frequency of the trap — with a 17 G field the trap has a central field of about 7 G, with a depth of a few millikelvin and a radial frequency of about 170 Hz. The large cross sectional areas of the wires mean that the width of the wire is comparable to the trap-wire separation, meaning that models of the magnetic field that approximate the wires to be infinitely thin give inaccurate results. More accurate results can be obtained using a 'filament model' where large wires are approximated by sets of infinitely thin wires, or by using finite element analysis.

Experimental Observations

Once the U-MOT has been loaded with around 7 $\times 10^7$ atoms, the centre of the quadrupole field is shifted by ramping the bias fields over about 200 ms to move the MOT to the position of the magnetic trap. By shifting the frequency of the MOT light by 30 MHz to the red for 4 ms the cloud is cooled to about 50 μK, at which point the MOT fields are switched off and the atoms are subjected to optical pumping to drive them into the low-field seeking $m_{\mathrm{F}} = +2$ substate. With a director field of 11 G oriented in the z direction, we find optimal optical pumping occurs with a 0.2 mW pulse of $F_{\mathrm{g}} = 2 \rightarrow F_{\mathrm{e}} = 2$ light that lasts for 2 ms, at which point the magnetic trap fields are switched on. Longer pulses of optical pumping light result in higher numbers of atoms being pumped, but this must be balanced against atom loss as the untrapped atoms move away from the capture volume of the magnetic trap.

This procedure results in around 2.5 $\times 10^7$ atoms being captured by the magnetic trap. Subsequent thermalization of the atoms causes some to escape from the trap, reducing the number to 1.7 $\times 10^7$ by around 1.3 s. Once the trap has thermalised, the cloud has a temperature of 100 μK, as determined by measuring time-of-flight expansion. Background gas collisions then act as the dominant loss mechanism, giving the trap a pressure-limited lifetime of 5.0 s. The effects of these two loss mechanisms are shown in Figure 3.6.

3.4. Vacuum Setup and Difficulties

Cold matter experiments generally use evaporative cooling techniques to efficiently cool atom clouds. These techniques involve selective removal of the atoms in the cloud with the highest energy, typically by truncating the trap at a certain energy level, reducing the average energy of the cloud. If the cloud is then given sufficient time for each atom to undergo a few elastic interatomic collisions, the energy will be redistributed according to the equilibrium Boltzmann distribution of the potential, increasing the fraction in the lowest energy levels and decreasing the fraction in the highest energy levels. Therefore, by reducing the truncation level slowly enough to allow the cloud to stay close to the equilibrium energy distribution, the

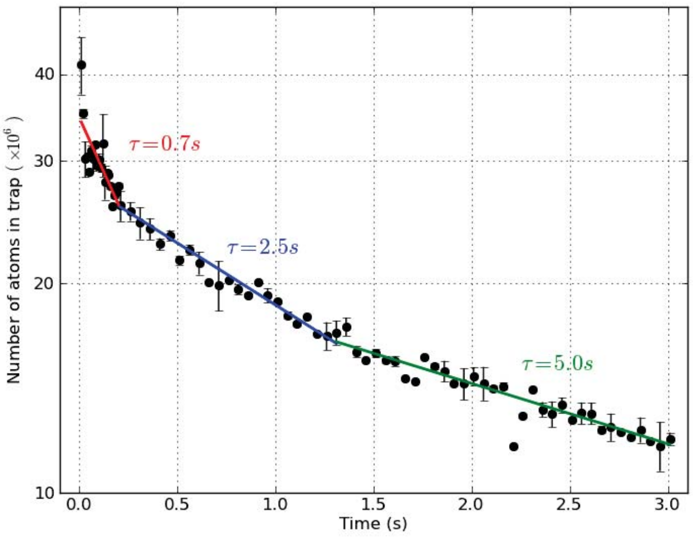

Figure 3.6.: The number of atoms held in the magnetic trap (black) as a function of hold time with exponential decay curves fit to the various loss rates due to rethermalization (red and blue) and background gas collisions (green).

phase-space density of the cloud can be substantially increased.

However, the increase in phase space density is counteracted by the exponential decay in atom number resulting from the background gas collisions mentioned in Section 3.3.3. If the background loss rate is too high relative to the interatomic collision rate, the truncation level cannot be lowered slowly enough to keep the highest energy levels depopulated without significant atom loss occurring across all energy levels. This serves to reduce the maximum efficiency of the process. The interatomic collision rate of our magnetic trap as described in Section 3.3.3 is comparable to the background loss rate, meaning that we cannot achieve efficient evaporative cooling using the current setup. As the background loss rate is proportional to the pressure inside the vacuum chamber, if the pressure can be reduced we would expect to see a slower background loss rate and thus a higher maximum efficiency for our evaporative cooling process. The pressure in our chamber is 1.7×10^{-9} Torr as measured using a nude Bayard-Alpert gauge, much higher than the pressures achieved in other cold atom experiments using vacuum equipment similar to ours. Further details of our work on evaporative cooling for this experiment are given in Chapter 5.

3.4.1. Improving the Vacuum

When I joined the experiment in 2010, the main chamber and the LVIS chamber were both pumped by ion pumps, which have effective in-chamber pumping rates (taking into account the limited conductance of the connecting pipes) of around 2.4 l/s for N_2, which should be capable of pumping the 6.3 litre system to pressures well below 10^{-9} Torr. The fact that the pressure remains above 10^{-9} Torr indicates that either there is a small leak in the system, or one of the components of the internal setup has a high outgassing rate. As the system was leak-checked when assembled the outgassing possibility was examined first, with several possible causes identified; the coating of the optical fibres connected to the chip, the H74 glue used to hold the chip components together and the Epotek OG116 glue on the V-grooves used to couple the optical fibres to the waveguides.

To investigate these candidates we assembled a ‘test chamber’, separate from the main experiment’s vacuum system. The test chamber consists of an empty, windowless stainless steel vacuum chamber, similar in size and shape to the one used in the main experiment. The chamber is connected to a 40 l/s ion pump (through a pipe of conductance similar to the one in the main chamber) and an ion gauge, and sealed off from atmosphere with a valve. A schematic diagram of the setup is shown in Figure 3.7a.

When the valve is opened the system can be pre-pumped by a Leybold TW70H turbomolecular pump with a pumping speed of 60 l/s, with a roughing line provided by a Leybold DiVac 2.5VT diaphragm oil-free pump. The pressure at the inlet flange of the turbo pump is monitored with a cold cathode gauge. Once the chamber had been assembled it was baked at around 100°C for 5 days, reaching a pressure of 7×10^{-10} Torr 3 days after the baking was turned off. Higher temperatures would be preferable and would shorten the necessary baking time and probably ultimately result in a better vacuum. However, the baking temperature was chosen to resemble that used for the main experiment’s chamber, which has its maximum temperature limited by the glass transition temperature of the glue used to couple the optical fibres into the chip waveguides. Following baking the chamber was vented on nitrogen and opened, and a 24 m-long optical fibre was placed inside in order to test the outgassing rate of the fibre coating. This had a surface area of 188cm^2, around 10 times the area of the coating present in the main experiment's vacuum chamber. Then the chamber was baked and pumped down again, and a pressure rise test was performed. This consisted of switching off the ion pump and measuring the increase in pressure on the ion gauge as a function of time. This process was repeated for a sample of 5.6 g of H74 glue, glued between 6 copper plates to try to replicate the conditions in the main chamber, and then for 2 V-groove sets with fibres glued in (but with the fibre lengths extending out of the grooves cut off). The pressure increase rate $\frac{dP}{dt}$ was modelled using

$$V\frac{dP}{dt} = \sum_{\mathrm{i}} Q_{\mathrm{i}} \exp\left(-\frac{t}{\tau_{\mathrm{i}}}\right) + Q_{\mathrm{leaks}}, \tag{3.11}$$

where V is the test chamber volume, τ_{i} is the equilibration time constant of the outgassing from material i and Q_{i} is the initial gas load from that material. The gas load due to leaks is constant, whereas those of the other sources are eventually balanced out by surface readsorption. Equation 3.11 solves to

$$P\left(t\right) = P_0 + \sum_{\mathrm{i}} \frac{Q_{\mathrm{i}}\tau_{\mathrm{i}}}{V}\left[1 - \exp\left(-\frac{t}{\tau_{\mathrm{i}}}\right)\right] + \frac{Q_{\mathrm{leak}}}{V}t, \tag{3.12}$$

where P_0 is the initial pressure. The gas loads Q_{i} are given in Torr.l/s. The gas load from outgassing for the fibre coating q_{fibre} is defined as outgassing rate per surface area, such that $q_{\mathrm{fibre}} = \frac{Q_{\mathrm{fibre}}}{A}$ where A is the surface area. The gas load from the H74 glue is defined as outgassing rate per unit mass, such that $q_{\mathrm{glue}} = \frac{Q_{\mathrm{glue}}}{m_{\mathrm{glue}}}$ where m_{glue} is the mass of the glue. For comparison, pressure rise tests were also performed for an empty chamber and the main experiment chamber. Equation 3.12 was fitted to the five pressure rise curves, as shown in Figure 3.7b. Values for the various q_{i} were inferred from the fits; q_{fibre} was found to be $(2.4\pm0.3)\times10^{-11}$ Torr.l.s^{-1}.cm^{-2} and q_{glue} was found to be $(5.7\pm0.1)\times10^{-10}$ Torr.l.s^{-1}.g^{-1}. The outgassing per V-groove was measured to be $4.1\pm0.1)\times10^{-10}$ Torr.l.s^{-1}. Using these q_{i} values with the quantities in the main chamber to estimate the outgassing rate $\sum Q_{\mathrm{i}}$ in the main chamber gives a total rate of 3.2 $\times10^{-9}$ Torr.l.s^{-1}, lower than the measured value of 4.7 $\times10^{-9}$ Torr.l.s^{-1}. The main experiment may have a

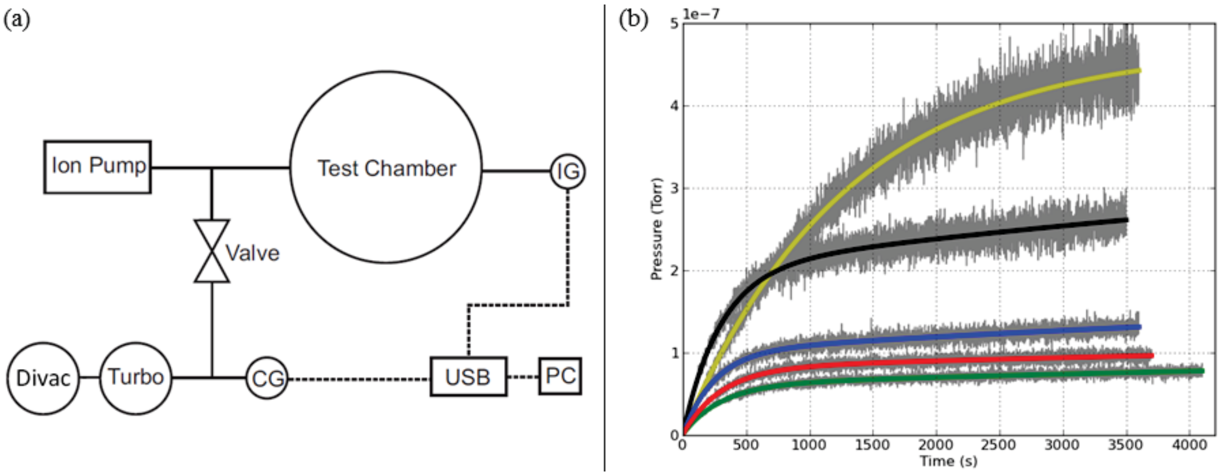

Figure 3.7.: (a) The experimental setup used to investigate the outgassing of the various chip components. (b) Pressure rise test results as measured with an ion gauge along with fits for the main experimental chamber (yellow) and the test chamber containing fibres (black), glue (blue), V-grooves (red) and nothing (green).

higher gas load because of the repeated heating of the setup — during a typical experiment the Z and bias wires will carry 50A, which over a series of experiments can heat the system to around 40°C. The higher pressure may also indicate the presence of a leak. However, a thorough leak test of the system using helium did not reveal any.

If the glue and fibres are the source of the high pressure, the gas load in the system is likely to be composed primarily of organic molecules. The addition of a cold finger to the system should help reduce the pressure, as cold fingers have been shown to be effective at removing high-mass particles from vacuum systems. A preliminary test of a cold finger on the test vacuum chamber (now empty) reduced the pressure from 2.3×10^{-9} to 7×10^{-10} Torr. Unfortunately, the cold finger had little effect on the pressure of the main chamber, reducing the pressure by only 10^{-10} Torr. A non-evaporable getter pump has also been installed on the system, but again without any significant effect on the pressure.

To learn more about the high pressure the gas contents of the main vacuum system were examined using a residual gas analyser (RGA). The RGA was installed as part of a hose system with a turbo pump, connected to the valve that seals off the main chamber. The mass spectrum of the baked hose system outside the valve showed significant partial pressures of H_2, H_2O, N_2 and CO_2, at an overall pressure of 10^{-7} Torr. Once the valve was opened and the RGA could detect gases from the main chamber, an overall reduction in pressure by a factor of 2 was observed in the hose system. No additional peaks were detected, but the H_2O peak reduced less than would be expected given the proportional volumes of the sealed and open systems. This suggests some water is present in the system, and this may be contributing to the gas load. This suggests the temperature at which the system was baked was not high enough - unlike most vacuum setups the temperature had to be limited to around 100°C to prevent the OG116 glue on the V-grooves from losing viscosity and disrupting the fibre coupling. To compensate for the lower temperature the system is baked for two weeks, but this may not have been long enough. Attempts to further bake the system by leaving the chip at 60°C every weekend for 2 months did not show any effect on the pressure, however.

To improve the chamber pressure it may be necessary to redesign the chip, with a design that maintains heat conduction between the components while minimising the amount of glue required. It may also help to strip the coatings from the fibres inside the vacuum chamber.

4. Experiments in the Trench

Chapter 3 describes the various ways in which we can prepare cold atom clouds near the chip, using MOTs or magnetic traps. To get atoms to interact with the waveguides written in the silica, we need to move them into the trench situated in the centre of the chip. This chapter discusses the introduction of detection light into the trench, the experimental procedures that produced the first in-trench absorption using atoms from a MOT, and subsequent experiments using atoms from a magnetic trap.

4.1. Sending detection light through the chip

Section 3.2 describes our laser setup. The light to be used in the waveguides is split off from the LVIS MOT light and sent through an AOM that allows us to tune its frequency, and a mechanical shutter. It is then coupled into a fibre that delivers the light close to the main vacuum chamber, where it is emitted from the fibre and split into three using 50:50 beamsplitters. Each of the three beams can then be attenuated as needed using neutral density filters, before being coupled into a fibre which has been spliced[1] to a fibre connected to the chip. The detection light is split into three to allow us to easily change which chip fibre it enters — currently, we can only use one fibre at a time, so when performing experiments we block the light from entering the other two.

These fibres enter the vacuum chamber via Teflon ferrules (similar to those used in [72]) and are then coupled to the waveguides using V-groove assemblies glued to the side of the chip. Details on the alignment of the V-groove assemblies and early waveguide tests are given in [54].

The total transmission across the chip varies by fibre and ranges from

---

[1] Using an arc fusion splicer.

1–6.5%, significantly lower than expected given that on test chips the transmission was around 35%. In practice, it was found that part of the subchip prevents the V-groove assembly on one side of the chip from optimal alignment, so we believe that most of the loss occurs at this interface.

The microscopic size of the detection beams inside the trench poses a problem, because high-intensity resonant light can saturate an atomic transition, causing a drop in absorption. For the $|F = 2, m_{\mathrm{F}} = +2\rangle \rightarrow |F = 3, m_{\mathrm{F}} = +3\rangle$ transition that we use for detection, the saturation intensity $I_{\mathrm{sat}} = 1.67$ mW/cm^2. Since the spot size of the beam is expected to be 2.2 μm, this corresponds to a power of about 120 pW. To avoid a significant drop in absorption we aim for intensities around $0.1 I_{\mathrm{sat}}$, so we need to have about 12 pW in the trench. Assuming that the drop in transmission is relatively constant across the chip assembly, around 3 pW at the fibre output should correspond to 12 pW in the trench. We attenuate to this power using neutral density filters.

Powers the order of picowatts are difficult to measure using a standard photodiode, so we measure the light exiting the chip with a single-photon avalanche photodiode (APD). Powers of 3 pW correspond to photon count rates of about 12/μs, which will be reflected as 10/μs on the APD given the dead time of 32 ns. When the detection light is not on, we measure a count rate of around 0.01/μs. To get a zero-light count rate this low, we had to block out as much ambient light as possible, which entailed covering the seams of the APD case with black tape and covering the entire device with matte black cloth.

4.2. Absorption signals from a MOT

The first signals of atoms entering the trench were achieved using the U-MOT. After 2 s of loading, the MOT contains around 7×10^7 atoms around 3 mm from the chip. By ramping down the current in the U plate we can move the trap centre into the chip.

The exact position of the trench can be found by sending non-attenuated detection light through the waveguides[2]. Some of the light scatters out of the trench, making it visible on the CCD camera we use to measure the 45° imaging beam (see Section 3.2.3). We steer the MOT cloud towards the

---

[2] With the APD switched off to prevent damage.

trench in the x and z directions by adjusting the bias fields during the U plate ramp, measuring how the cloud moves using the 45° imaging system. The MOT light and trap currents are switched off as the cloud approaches the trench, with the momentum of the atoms carrying them upwards into the trench.

Atoms in the trench were detected by coupling the detection light into the 5th waveguide, near the centre of the trench, and opening the detection light shutter around 30 ms before the cloud hits the chip and measuring the transmitted power on the APD as a function of time. As the cloud reaches the chip we measure a small ($< 1\%$) drop in transmission, indicating that some of the light is being scattered by atoms in the trench. This drop in transmission is shown in Figure 4.1a. The drop lasts for about 1 ms, and is only visible against the intensity noise after the signal has been averaged around 20 times. By measuring the maximum absorption in a signal as a function of various ramp parameters we can increase the absorption to around 1.2%.

Aside from the position of the cloud, the most important parameter was the speed of the ramp, as shown in Figure 4.1b. Faster ramps produce much larger signals than slower ones, suggesting that slow ramps allow too many atoms to hit the room temperature chip surface, causing them to be ejected from the trap.

4.2.1. Absorption Analysis Algorithm

Graphs of in-trench absorption such as Figure 4.1b have been produced using an analysis algorithm that can be used to automatically obtain the magnitude of the absorption from APD traces, such as the one shown in Figure 4.1a. This algorithm checks that the trace was measured correctly, then corrects the count rate to account for the APD dead time (32 ns) using the formula

$$\text{Corrected count rate} = \frac{R}{1 - R \times (32\ ns)}, \tag{4.1}$$

where R is the uncorrected count rate. The trace is then smoothed using the Hann window function[73] — traces with lower signal-to-noise ratios require more smoothing (i.e. larger windows) to give accurate results. The absorption is then determined by finding the time of lowest count rate (within a user-defined ‘signal region’), and comparing this count rate with the back-

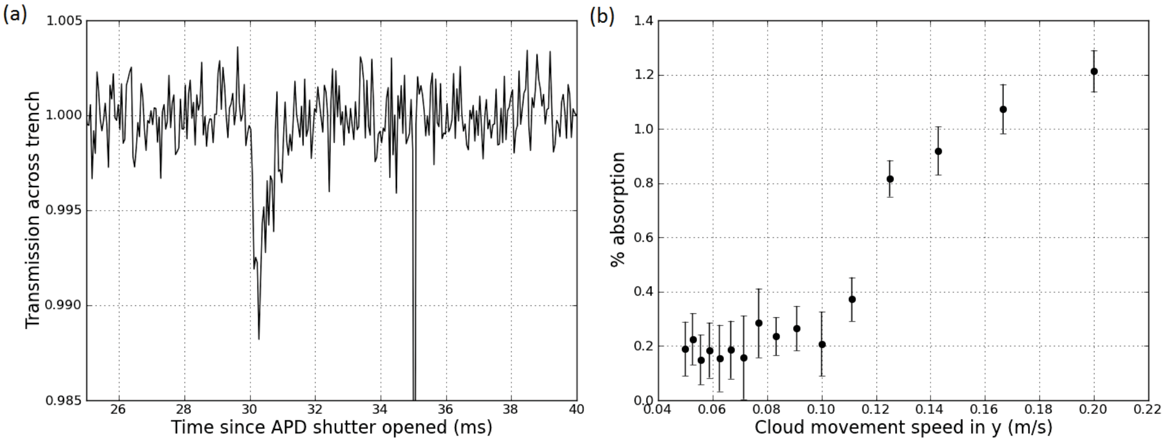

Figure 4.1.: (a) The drop in transmission across the chip we observe as the MOT cloud hits the trench, as measured on the APD. Atoms from the cloud enter the trench at around 30 ms, absorbing some of the detection light. There is a second drop at 35 ms that is caused by a mechanical shutter on the experiment closing, not the presence of atoms in the trench. This graph shows the average of results from about 50 separate experiments. (b) The absorption as a function of cloud movement speed. Slower entry speeds result in more atoms hitting the room temperature chip surface instead of entering the trench, ejecting them from the trap and reducing the overall absorption.

ground count rate, which we obtain by repeating the same experimental procedure, except with the initial MOT loading disabled.

This algorithm will, in the absence of a genuine absorption signal, return an absorption magnitude proportional to the noise on the signal, which itself is proportional to the square root of the number of averages taken, hence the 0.2% ‘background’ absorption visible on Figure 4.1b. The magnitude of a genuine absorption signal is returned accurately, however — there is no need to subtract the background absorption. When scanning over a parameter (such as ramp speed) we randomise the order of experiments to account for slow drifts in experimental conditions, and for particularly long scans we periodically use absorption imaging to check that the MOT number is stable throughout. This algorithm is used for all of the in-trench absorption measurements described in this thesis.

4.2.2. Interpreting absorption measurements

We can interpret these results by assuming the atom density is homogeneous in the trench (this is reasonable, as the MOT cloud is much larger than the trench), in which case the absorption A in the trench is given by

$$A = 1 - \exp\left(-n\sigma w_{\mathrm{T}}\right), \tag{4.2}$$

where n is the atom number density, σ is the absorption cross section and w_{T} is the width of the trench.

Using the measured absorption of 1.2% in equation (4.2) suggests the number density in the trench is around 5×10^{-3} /μm^3 (or 5×10^{15} /m^3), which is similar to the central number density we measure in the MOT cloud prior to trench entry using absorption imaging. Changing between the three waveguides connected to fibres shows no measurable variation in absorption, suggesting the assumption of a homogeneous number distribution in the cloud is valid, as shown in [74].

We can use the measured number density to estimate the number of atoms that interact with the light. In general, if an atom cloud with a number distribution $n(x, y, z)$ is hit by a beam with an intensity profile $I(x, y, z)$, the number of atoms that interact with the beam could be reasonably defined as

$$N_{\mathrm{a}} = \frac{1}{I_0}\int_{-\infty}^{+\infty}\int_{-\infty}^{+\infty}\int_{-\infty}^{+\infty} I(x, y, z)n(x, y, z)dx\,dy\,dz. \tag{4.3}$$

where I_0 is the peak intensity of the beam. If $n(x, y, z)$ is homogeneous, and we assume the beam is gaussian and does not diverge much as it propagates across the trench, equation (4.3) evaluates to

$$\begin{aligned} N_{\mathrm{a}} &= \frac{1}{I_0}\int_{0}^{w_T} dx \int_{-\infty}^{+\infty} dy \int_{-\infty}^{+\infty} dz\, I(x, y, z)\, n\, dx\, dy\, dz \\ &= \pi w_0^2 w_{\mathrm{T}} n, \end{aligned}$$

where w_0 is the beam waist, 2.2 μm. Since $n = 5 \times 10^{-3}$ /μm^3, we find that $N_{\mathrm{a}} = 1.1$. The waveguide system is therefore sensitive enough to detect one atom in the beam mode, on average.

We use the atoms in the trench to check that the intensity of the detection light is sufficiently low compared to I_{sat}, by measuring the absorption as a function of input light power. These measurements are shown in Figure 4.2. Further details of these early experiments on MOT clouds in the trench are given in [74] and [54].

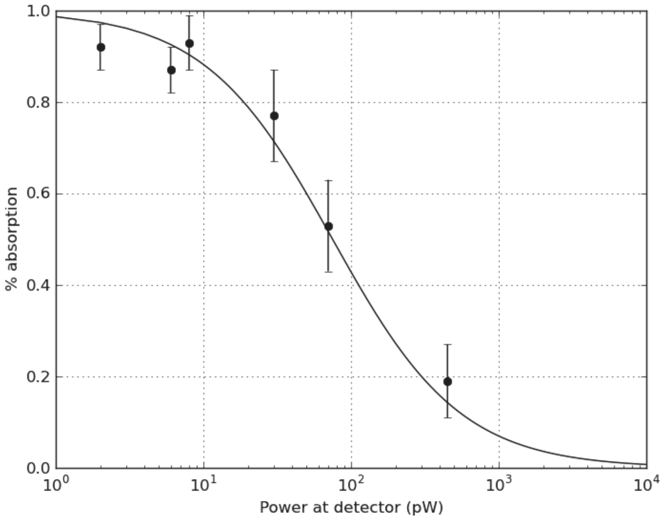

Figure 4.2.: Measuring the effect of increasing the power of the detection light on the in-trench absorption. As the power increases the absorption decreases, as the $F_{\mathrm{g}} = 2 \rightarrow F_{\mathrm{e}} = 3$ transition that we use for detection becomes saturated. The curve $\frac{A_0}{1+P/P_{\mathrm{sat}}}$ is fitted to the data, where A_0 is the absorption in the absence of saturation ($\approx 1\%$) and $P_{\mathrm{sat}} = 60 \pm 21$ pW corresponds to the power measured at the detector when the intensity in the trench is equal to I_{sat}.

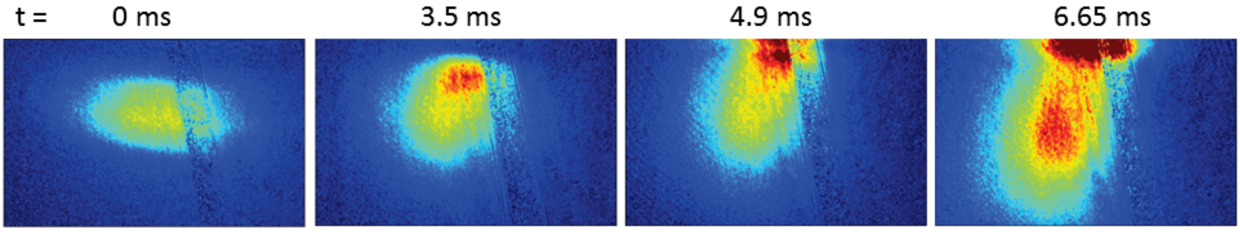

Figure 4.3.: Sequence of absorption images taken using the 45° imaging system showing the movement of the magnetic trap as it is moved into the trench over 7 ms. The trench is not visible but it is close to the top of each image. The reflective chip surface above the waveguides is not quite flat, so there is a (diagonal) line of distortion across each image. Each image shows a 1.5 mm × 0.8 mm area.

4.3. Absorption signals from a magnetic trap

We have also measured absorption signals using atoms from the magnetic trap. Loading the magnetic trap from the MOT cloud results in a cloud of 1.7×10^7 atoms at a temperature of 100 μK held about 1 mm from the chip. We can move the trap centre up towards the chip by increasing the current in the bias wires and decreasing the current in the Z wire. The trap needs to be moved in x to reach the trench, which we achieve by adjusting the y bias field — this moves the trap centre in a circular path around the Z wire in the $x - y$ plane. Some absorption images of the magnetic trap as it is moved to the trench are shown in Figure 4.3. The images are taken with the ramp that produces the largest absorption signals. We see that this ramp moves the trap so fast that a large proportion of the atoms are left behind.

As with the MOT cloud, we introduce the detection light 30 ms before the ramp ends and hold it on for 80 ms. After some adjustment of the ramp we observed a drop in transmission, achieving 9% absorption following some optimization, as shown in Figure 4.4. 9% absorption implies that 4.4 atoms are entering the beam mode, on average. The speed of the ramp was again crucial, with absorption only visible using ramps that move the trap very fast. With such a hot cloud we expect very few atoms to have low enough energy to stay in the central region of the trap, so the entry ramp has to be shorter than the oscillation period of the trap. This prevents atoms near the trap centre from moving too much and hitting the walls before entering the waveguide mode.

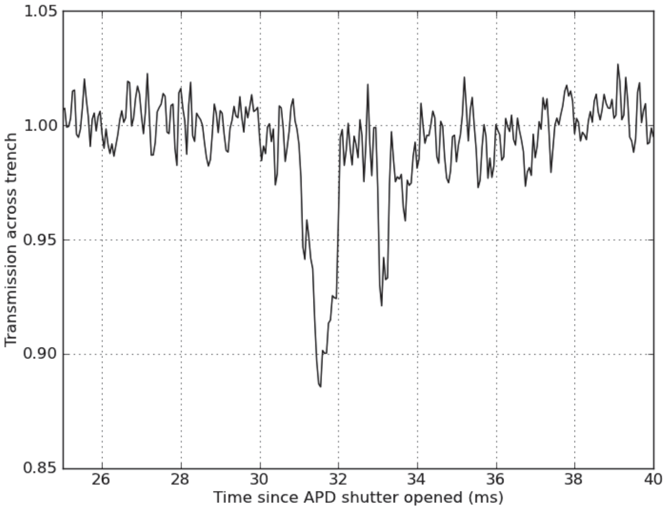

Figure 4.4.: The drop in transmission across the chip we observe as the magnetically trapped cloud hits the trench, as measured on the APD. Atoms from the cloud enter the trench at around 30 ms. In this case we see two transmission drops due to atoms entering the trench — evidently, the rapid movement of the magnetic trap has disrupted the cloud in such a way that a small part of it enters the trench 2 ms after the rest. This graph shows the average of results from about 30 separate experiments.

We expect a central number density in the magnetic trap of around $0.03\ /\mu\text{m}^3$, suggesting we should be able to achieve absorption signals of 14%. The first image in Figure 4.3 shows that the trap is offset from the trench in z before the ramp, which is presumably why we only observe 9%.

4.3.1. Polarization Dependence

During the initial experiments using the magnetic trap we noticed a slow drift (taking place over several hours) in the measured absorption. Measurements looking at the absorption over a range of frequencies showed that the absorption spectrum as a whole was changing shape over time, as shown in Figure 4.5.

This is most likely a result of the detection light polarization in the fibres (which are not polarization-maintaining) drifting over time, combined with the presence of a magnetic field during measurement. When the atoms from the magnetic trap enter the trench, the trapping fields are switched off, but there is a homogeneous 14 G field oriented in the y direction that cannot be switched off quickly (due to the inductance of the y bias coils). The presence of the field means that the magnetic substates of the atoms are no longer degenerate, and can be addressed by different polarizations of light.

Light with linear polarization parallel to the direction of the magnetic field will cause the atoms to undergo π transitions, where the projection of angular momentum m_F is unchanged. Light that is circularly polarised (and light that has a linear polarization which is not parallel to the magnetic field) will drive σ_+ and σ_- transitions in the atoms, in which m_F is changed by $+1$ and -1 respectively. The change in the shape of the spectrum is therefore likely to result from the appearance and disappearance of the π and $\sigma_{+,-}$ absorption peaks as the light polarization drifts.

This idea is supported if we combine all the data from Figure 4.5, which gives the spectrum shown in Figure 4.6. Two separate peaks are clearly visible 9 ± 1 MHz and 20 ± 1 MHz higher than the zero field resonance. These shifts correspond roughly to the shifts we would expect for π ($\mu_\text{B}B/3h = 7$ MHz) and σ_+ ($\mu_\text{B}B/h = 21$ MHz) transitions, where B is the magnetic field (14 G) and μ_B is the Bohr magneton. The σ_- peak is expected at $-\mu_\text{B}B/3h = -7$ MHz, but the matrix element for this transition is 15 times smaller than for the σ_+, so the peak is barely visible. The σ_+ and the π

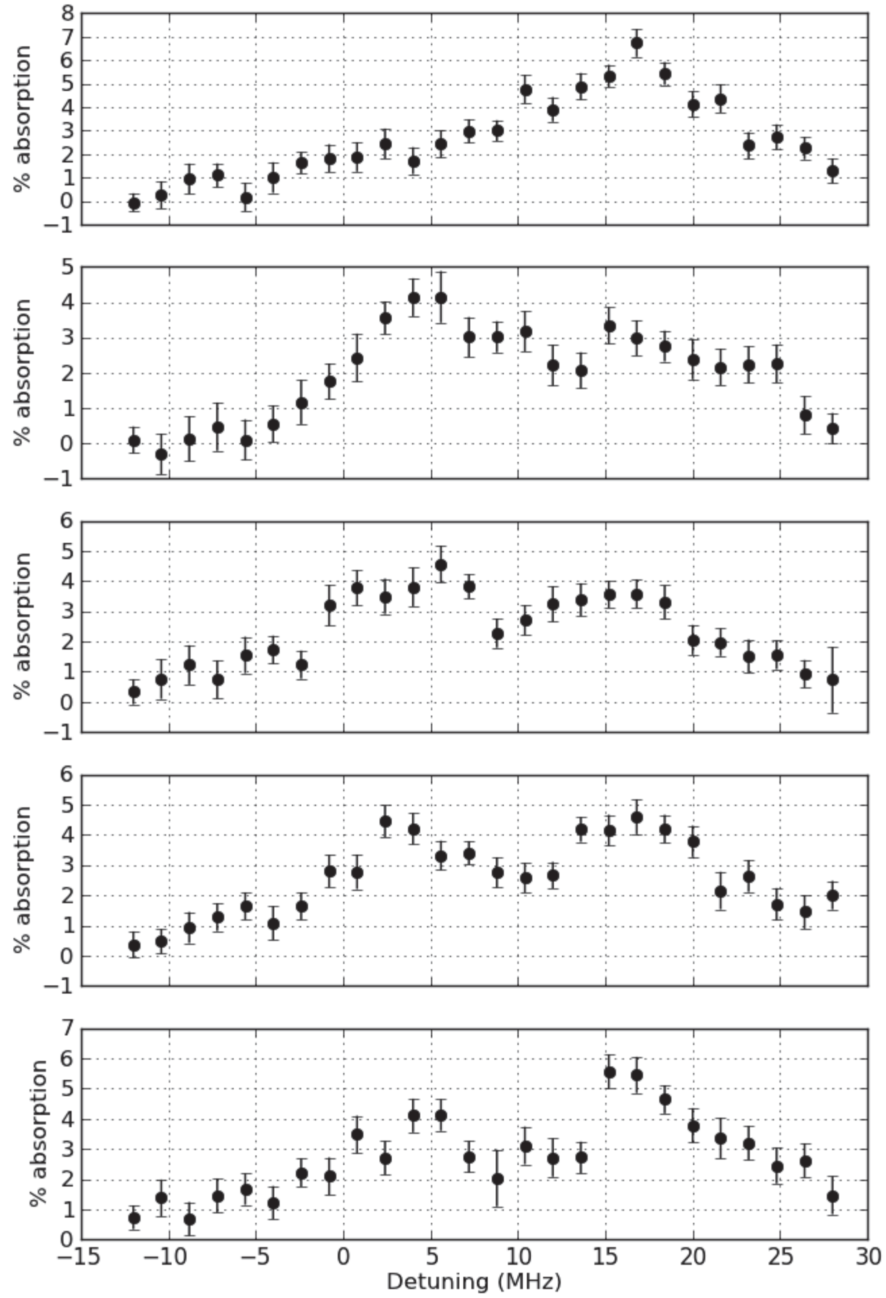

Figure 4.5.: Absorption spectra obtained using the magnetic trap over a total time of 2.5 hours, demonstrating the change in spectrum shape over this time. Each graph shows data taken over successive 30 minute blocks.

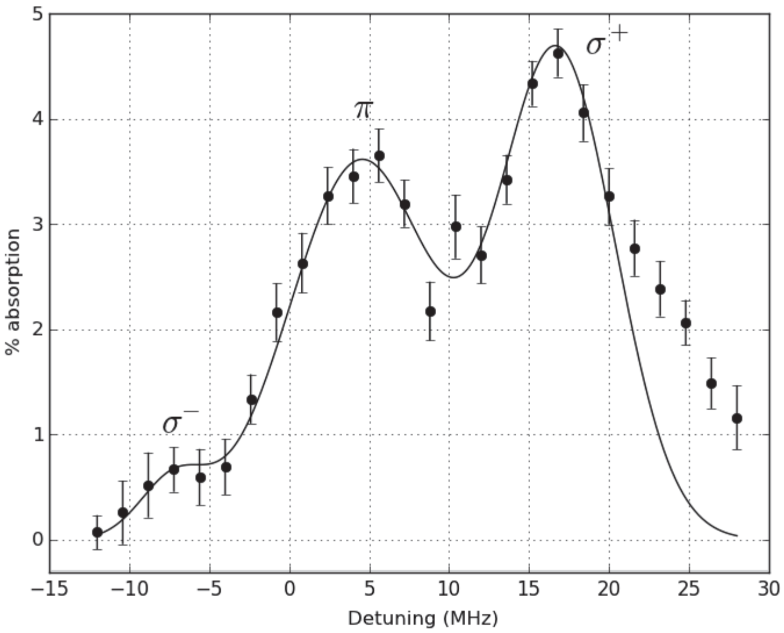

Figure 4.6.: Absorption spectrum obtained by incorporating all the data taken for Figure 4.5 into one graph, effectively integrating the spectrum over a range of polarizations. Absorption peaks due to the light addressing the σ_+ and the π transitions are clearly visible, and there is a small bump where we expect the σ_- peak. The positions of the peaks suggest the magnetic field is around 14 G, as expected.

peaks have FWHMs of 10 ± 1 MHz and 12 ± 2 MHz respectively, higher than the expected width of 6 MHz. This disparity is most likely the result of Doppler broadening, as the cloud is heated substantially by its rapid movement into the chip.

We can stabilise the detection light polarization to an extent by taping the fibres to metal surface of the optics table, keeping them still and stabilising their temperature, which slows the polarization drift substantially. Additionally, we have placed a linear polarizer and a $\lambda/4$ waveplate in front of the fibre coupler, allowing us to tune the polarization manually. By adjusting the waveplate we find we can shift between the π and $\sigma_{+,-}$ spectra at will. We are therefore confident that we have a correct understanding of the physical processes behind the changing spectra obtained using the magnetic trap.

5. Cooling using a Hybrid Dimple Potential

The magnitude of the in-trench absorption signals obtained from the atom cloud in the magnetic trap has been limited by the number density of the cloud. Increasing the density by just adiabatically compressing the trap to the 1 kHz trap in the trench is not an option; the compression will increase the cloud's temperature to 325 μK, so that only one atom in 10^5 will have low enough energy to remain held in the trench without hitting the walls. To ensure that the cloud is sufficiently cold to fit in the trench, the temperature in the 1 kHz trap needs to be the order of 1 μK. Boosting the magnitude of our absorption signals will therefore require some evaporative cooling of the cloud. This chapter describes our efforts to cool the cloud efficiently enough to increase the number density.

5.1. Evaporative Cooling in the Magnetic Trap

Evaporative cooling is a commonly used technique in cold atom physics experiments. By removing high energy atoms from a trapped cloud and allowing the remaining atoms to rethermalize we can increase the population of lower energy states. This section covers the theory underlying evaporative cooling and our attempts to apply it to atom clouds held in our magnetic trap.

5.1.1. Theory

The dynamics of the evaporative cooling process can be examined by considering the general case of atoms confined in a spherical harmonic potential.

For a trapping potential $U(\mathbf{r})$ we can define the density of states $\rho(\epsilon)$ as

$$\rho(\epsilon) = \frac{1}{h^3} \int \int \delta \left(\epsilon - U(\mathbf{r}) - \frac{p^2}{2m} \right) d^3p \, d^3r, \tag{5.1}$$

where $\rho(\epsilon)d\epsilon$ is equal to the number of single-particle eigenstates in the trapping potential with energies between ϵ and $\epsilon + d\epsilon$.

If we integrate this expression over all momenta, we obtain

$$\rho(\epsilon) = \frac{2\pi(2m)^{\frac{3}{2}}}{h^3} \int_{\mathrm{U}(\mathbf{r}) \leq \epsilon} d^3r \sqrt{\epsilon - U(\mathbf{r})}. \tag{5.2}$$

For a spherical harmonic trap where $U(\mathbf{r}) = \frac{1}{2}k|\mathbf{r}|^2$ this evaluates to

$$\rho(\epsilon) = \left(\frac{m}{k}\right)^{\frac{3}{2}} \frac{\epsilon^2}{2\hbar^3}. \tag{5.3}$$

Taking the 'ergodic approximation' — that is, the number distribution P of the atoms is dependent only on energy[75], we can write

$$P(\epsilon) \propto \rho(\epsilon) e^{-\epsilon/k_{\mathrm{B}}T}, \tag{5.4}$$

where T is the temperature. We therefore see that

$$P(\epsilon) = A\epsilon^2 e^{-\epsilon/k_{\mathrm{B}}T}. \tag{5.5}$$

where A is a normalisation constant.

The removal of atoms with the highest energy can be modelled by truncating this distribution above a certain energy E_{evap} (as shown in Figure 5.1a). Assuming the cloud has rethermalised after each atom has had an average of four collisions[75], the rethermalization rate can be taken as $\gamma_{\mathrm{el}}/4$, and the rate at which atoms are evaporated from the trap can be determined as

$$\frac{dN}{dt} = \left[-\frac{\gamma_{\mathrm{el}}}{4} \frac{\int_{\eta}^{\infty} P(\epsilon) d\epsilon}{\int_{0}^{\infty} P(\epsilon) d\epsilon} - \frac{1}{\tau_{\mathrm{loss}}} \right] N = \left[-\frac{\gamma_{\mathrm{el}}}{4} \frac{\Gamma(3,\eta)}{2!} - \frac{1}{\tau_{\mathrm{loss}}} \right] N \tag{5.6}$$

where η is the 'truncation parameter', equal to $\frac{E_{\mathrm{evap}}}{k_{\mathrm{B}}T}$, $\Gamma(x,\eta)$ is the incomplete gamma function[1] and τ_{loss} is the time constant for atom loss due to

---

[1] Given by $\Gamma(x,\eta) = \int_{\eta}^{\infty} t^{x-1} e^{-t} dt$

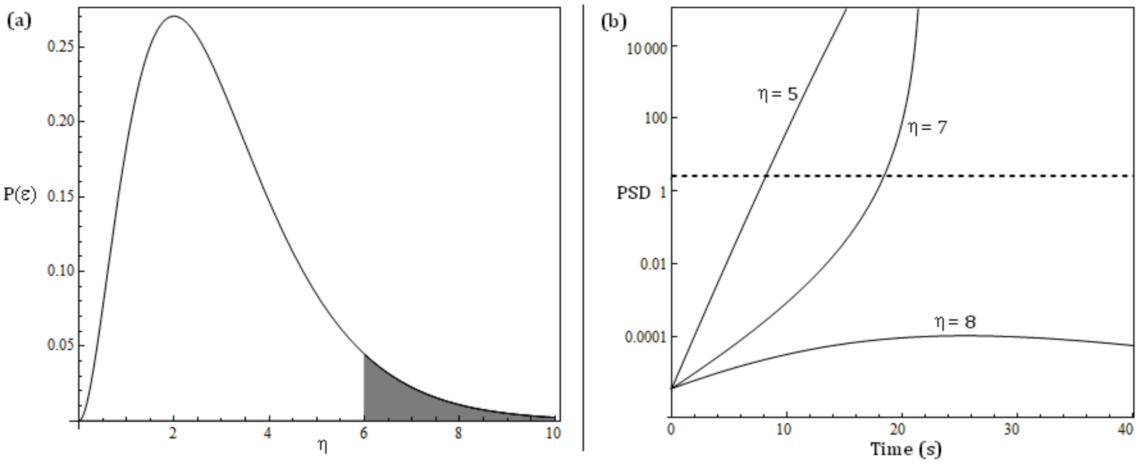

Figure 5.1.: (a) A truncated Boltzmann distribution, representing the number distribution of atoms as a function of energy in a 3D harmonic trap. In this case the distribution has been truncated so that the atoms with energies higher than $6k_\mathrm{B}T$ are removed. (b) Evaporation trajectories for a spherical trap with $f_\mathrm{T} =$ 300 Hz, $\tau_\mathrm{loss} = 10$ s, $N_{\mathrm{t}=0} = 10^7$ and $T_{\mathrm{t}=0} = 0.1$ mK for three values of η. The dashed line indicates the PSD required for Bose-Einstein condensation. The $\eta = 5$ and $\eta = 7$ trajectories reach this PSD (although only $\eta = 7$ undergoes runaway evaporation) while the $\eta = 8$ trajectory is too slow to make up for the rate of the loss processes.

collisions with background gas species and from inelastic collisions from within the trapped cloud. The energy loss rate is given by

$$\frac{dE}{dt} = \left[-\frac{\gamma_\mathrm{el}}{4}\frac{\int_\eta^\infty \epsilon P(\epsilon)d\epsilon}{\int_0^\infty \epsilon P(\epsilon)d\epsilon} - \frac{1}{\tau_\mathrm{loss}}\right]E = \left[-\frac{\gamma_\mathrm{el}}{4}\frac{\Gamma(4,\eta)}{3!} - \frac{1}{\tau_\mathrm{loss}}\right]E, \tag{5.7}$$

and by using the relation $E = 3Nk_\mathrm{B}T$ we obtain:

$$\frac{dT}{dt} = \left[-\frac{\gamma_\mathrm{el}}{4}\left(\frac{\Gamma(4,\eta)}{3!} - \frac{\Gamma(3,\eta)}{2!}\right)\right]T. \tag{5.8}$$

The collision rate γ_el is proportional to $\sigma_\mathrm{el}f_\mathrm{T}^3N/T$ (where f_T is the trap frequency)[2], therefore equations (5.6) and (5.8) are coupled. The elastic collision cross section σ_el can be approximated as $8\pi a^2$ for temperatures much lower than 350 μK[3], where a is the s-wave scattering length[76]. If the

---

[2] For a cylindrically symmetric trap, the trap frequency f_T must be separated into radial (f_r) and axial (f_z) frequencies by $f_\mathrm{T}^3 \rightarrow f_\mathrm{r}^2 f_\mathrm{z}$

[3] The full expression for σ_el is $8\pi a^2/(1+k_\mathrm{dB}^2a^2)$ where $k_\mathrm{dB} = \sqrt{2\pi}h/\sqrt{mk_\mathrm{B}T}$ is the wave number of the atomic wavefunction. Therefore, when $T \ll h^2/2\pi a^2 mk_\mathrm{B} \approx 350\ \mu$K, σ_el can be approximated by $8\pi a^2$.

evaporation proceeds with a constant truncation parameter (and therefore a decreasing energy cutoff), analytic solutions exist for N and T. These solutions can be combined to give an expression for the *phase space density* of the cloud, equal to $n(\mathbf{r})\lambda_{\mathrm{dB}}^3$ where $n(\mathbf{r})$ is the number density of the cloud and λ_{dB} is the spatial extent of the atom wave packet, which is a function of temperature. We are most interested in the phase space density at the centre of the cloud, so throughout this chapter and the rest of the thesis, 'phase space density' refers to $n_0\lambda_{\mathrm{dB}}^3$, where n_0 is the number density at the centre.

The solution for phase space density is plotted for three different values of η in Figure 5.1b. The plot for $\eta = 7$ exhibits positive curvature throughout, indicating the cloud undergoing 'runaway evaporation' — the cloud cools down in such a way that the collision rate increases throughout the process, increasing the rethermalization rate of the atom cloud and thus greatly improving the efficiency of the evaporation process. Although the $\eta = 5$ process reaches the required phase density faster, it does not undergo runaway evaporation as the collision rate decreases throughout, and so the number of atoms remaining at the transition point is much lower than those remaining with the $\eta = 7$ process. The optimal value of η is ultimately dependent on the parameters of the experiment in question.

In magnetic traps the energy-selective truncation is typically achieved by applying radio-frequency (rf) radiation to the trap, slightly detuned from the frequency required to flip the spin of the atom being trapped. Only atoms with sufficient energy will be able to reach the magnetic field required to Zeeman shift their energy levels into resonance with the radiation, leading to them transitioning into a high-field seeking state and subsequently being ejected from the trap.

In optical traps no spatially-dependent Zeeman shift is present, so the same technique cannot be used. Instead, evaporation is typically performed by reducing the power of the trapping beams to reduce the trap depth. Unfortunately, this also reduces the trap frequency, and with it the collision rate γ_{el}, leading to a significantly reduced evaporation efficiency and making runaway evaporation significantly more difficult to achieve. In 2008 Hung *et al.* demonstrated that by adding a magnetic field gradient to an optical trap, the trapping potential could be 'tilted' to introduce an energy truncation without the trap frequency reduction caused by intensity reduction, and thereby achieved runaway evaporation[77]. However, this method required spin polarizing the atoms in the trap, removing the possibility of using this with spin mixtures. Another method that avoids this disadvantage has been demonstrated by Clément *et al.*, who used a misaligned crossed-beam trap configuration to similar effect[78]. In this case a second, wider beam was added to reduce the potential in one direction, decoupling the trap depth from its frequency and thus avoiding the collision rate reduction.

5.1.2. Evaporating in our magnetic trap

Starting from a magnetic trap containing 1.7×10^7 atoms at 160 μK, a small increase in collision rate can be obtained by increasing the radial trap frequency. Higher radial frequencies can be obtained by moving the centre of the trap closer to the chip, achieved by increasing the current in the bias wires or decreasing the current in the Z wire. Higher frequencies at the centre of the trap can be achieved by decreasing the minimum field of the trap (or trap bottom) by decreasing the bias field in the Z direction, as the field at the trap bottom is oriented almost parallel to the central strut of the Z wire. There is a limit to how far the trap bottom can be reduced before spin flip loss starts to occur; we find no loss occurs as long as the trap bottom is kept above 1 G. Additionally, decreasing the trap bottom shrinks the harmonic region of the trap, causing atoms to explore linear regions, which serves to lower the effective frequency. The radial size of the cloud also sets a minimum distance from trap to chip.

The highest radial trap frequency we are able to achieve from our starting cloud is 420 Hz. This was achieved by moving the trap closer to the chip, so that it was only 280 μm from the surface (compared to an initial distance of 850 μm), and by increasing the Z bias field from 15.6 G to 18 G (which required the addition of two more coils to the setup).

If the trap frequency is increased slowly enough, the change will be adiabatic, and the phase space density of the cloud will be conserved. For a cloud at thermal equilibrium in a cylindrical harmonic trap with radial frequency f_r and axial frequency f_z, the phase space density $n_0\lambda_\mathrm{dB}^3$ is proportional to $f_\mathrm{r}^2 f_\mathrm{z} T^{-3}$ where T is the cloud temperature. Therefore, if we adiabatically change the frequencies of the trap, the temperature should change according to

$$T_{\mathrm{f}} = T_{\mathrm{i}} \left(\frac{f_{\mathrm{r,f}}^2 f_{\mathrm{z,f}}}{f_{\mathrm{r,i}}^2 f_{\mathrm{z,i}}} \right)^{1/3}, \tag{5.9}$$

where T_{f} and T_{i} are the final and initial temperatures of the cloud respectively, and $f_{\mathrm{r,f}}$ and $f_{\mathrm{r,i}}$ are the final and initial radial trap frequencies respectively, with similar notation for the axial frequencies. For our compression, where f_{r} changes from 170 Hz to 420 Hz, we expect the temperature to increase by a factor of $(420/170)^{2/3}$, giving around 290 μK.

To ensure that our compression is adiabatic, we have measured the number of atoms remaining and width of the cloud (8 ms after being released from the trap) as a function of compression ramp time, both in the compressed trap and following a subsequent decompression phase where the trap is restored to its initial position with the same ramp time as the compression. The width results are shown in Figure 5.2. Short ramp times clearly cause an increase in width as well as a loss in number, indicating the compression is performed too rapidly, causing heating and ejecting atoms from the trap. To prevent this, a compression time of 25 ms was chosen.

We observe the temperature rising to 280 ± 10 μK during the compression, in line with what we expect from equation 5.9. This compression should increase the collision rate at the centre of the trap from 9 s^{-1} to 20 s^{-1}. The phase space density remains constant at around 3×10^{-7}.

We selectively remove atoms by sending an oscillating rf current through the Z wire using a function generator. The minimum field of the magnetic trap can be determined by finding the frequency that removes all of the atoms in the trap when applied for a few seconds. The number of atoms remaining in the magnetic trap after it has been subjected to a pulse of constant frequency is shown for a range of frequencies in Figure 5.3. The shape of the curve at energies above the trap bottom results from the energy distribution of the trap given in equation 5.5, as the remaining proportion of atoms at a frequency f_{RF} is given by

$$1 - \frac{\int_{\mathrm{E_{RF}}}^{\infty} P(\epsilon) d\epsilon}{\int_0^{\infty} P(\epsilon) d\epsilon} = 1 - e^{-\beta E_{\mathrm{RF}}} (2 + 2\beta^{-1} E_{\mathrm{RF}} + \beta^{-2} E_{\mathrm{RF}}^2) \tag{5.10}$$

where $\beta = 1/k_{\mathrm{B}}T$ and $E_{\mathrm{RF}} = h(f_{\mathrm{RF}} - f_{\mathrm{TB}})$ where f_{TB} is the frequency corresponding to the trap bottom. The dependence of the distribution on tem-

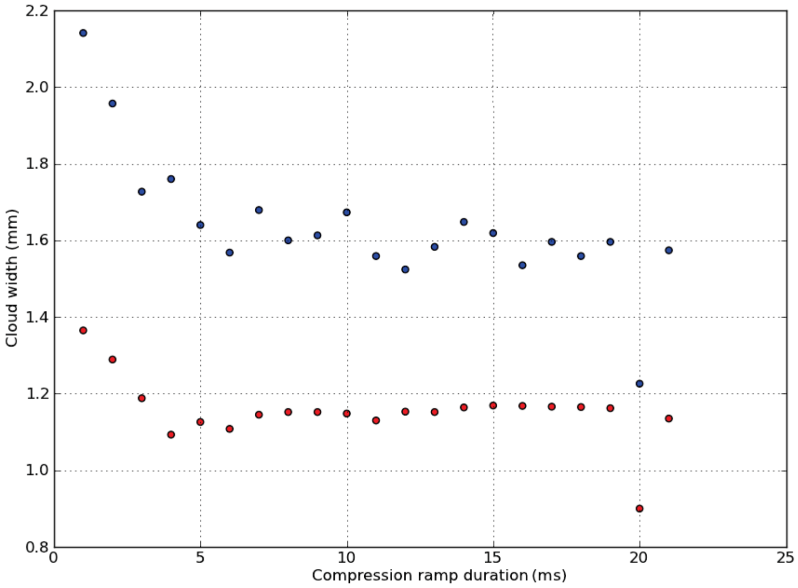

Figure 5.2.: The $1/e$ width of the magnetic trap cloud as measured 8 ms after the trap fields have been switched off, as released from the compressed (blue) and decompressed (red) traps. For shorter compression times the width is higher, indicating that the cloud has been heated and therefore the compression is non-adiabatic.

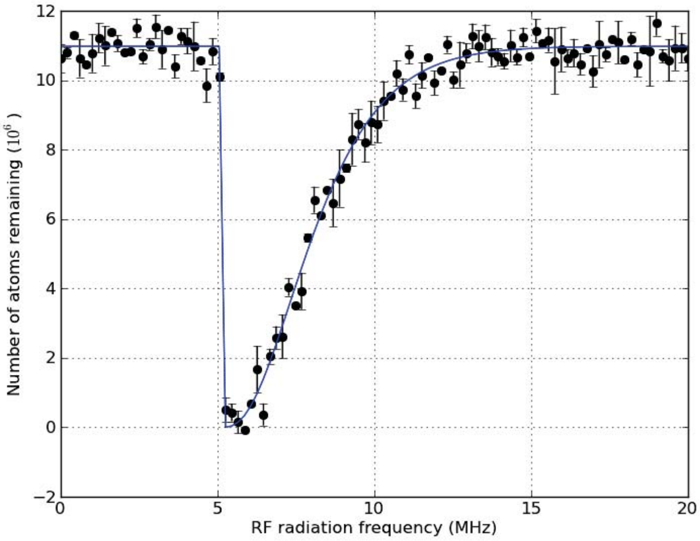

Figure 5.3.: Experimental results showing the number of atoms remaining following a 3 s pulse of rf radiation for a range of radiation frequencies (black). The initial number of atoms was around 20×10^6. The data are fitted to the curve given by equation 5.10 (blue), which suggests the temperature is around 52 ± 1 μK. Time-of-flight expansion measurements of the same cloud suggest the temperature is 50 ± 2 μK.

perature provides a second method of finding the temperature of a trapped cloud, by performing rf spectroscopy and fitting the curve to Equation 5.10. This temperature measurement technique has been described previously by Martin *et al.*[79].

We have developed a flexible system within our control software that enables easy creation and manipulation of piecewise evaporation ramps, allowing each stage of the ramp to be individually optimised. Using this system, we followed a procedure of introducing a new ramp, fixing its final frequency and holding this frequency for a short time following the ramp (thus fixing the temperature it is expected to cool to) and then adjusting the ramp speed and rf power to maximise the number of atoms remaining, thereby maximising the PSD at that temperature before moving on to the next ramp. Towards the end of the ramp when the optical density of the cloud becomes very low, time-of-flight measurements of the temperature become infeasible[4] so using the rf spectroscopy method was necessary.

The highest phase space density we were able to achieve was 2×10^{-5}, with a cloud of 10^4 atoms at a temperature of 5 μK — temperatures lower than this were unachievable without significant drops in number density. The evaporation efficiency[5] of this process is therefore around 0.4. A temperature of 5 μK in the 420 Hz trap suggests that following adiabatic compression into the trench the temperature would reach around 8 μK, in which case around one atom in four would be cold enough to avoid hitting the walls. Additionally, the number density of the cloud in the trench would be lower than that of the cloud used for the signals shown in Chapter 4 by a factor of 4. If the cloud is allowed to thermalize in the trench the density would reduce even further by a factor of around 2. Experiments looking for signals of atoms in the trench using this cloud showed no measured absorption.

5.2. Evaporating in a Hybrid Opto-Magnetic Potential

Evaporation in the purely magnetic trap is clearly not efficient enough if we want to boost the number density of our cloud inside the trench. Other groups have found that adding a tightly confining dimple to their trapping potential can boost evaporation efficiency. This section discusses our work on introducing a dimple to our magnetic trap to form an opto-magnetic 'hybrid' trapping potential and the results of a number of approaches using this hybrid potential to improve our evaporation process.

5.2.1. Our Hybrid Trap

We follow the approaches of Lin *et al.*[52] and Garrett *et al.*[43][6], generating a dimple by intersecting the centre of our cylindrical magnetic trap with an intense, tightly focussed laser beam with a wavelength to the red of the rubidium D_1 and D_2 transitions and directed perpendicular to the long axis of the trap.

---

[4] As the optical density of the cloud when imaged along the long axis of the trap varies as $(\omega_{\mathrm{R}}^{-1}+\tau)^{-3/2}$, where τ is the time of flight and ω_{R} is the radial angular trap frequency.

[5] Defined as $\frac{log(D_{\mathrm{f}}/D_{\mathrm{i}})}{log(N_{\mathrm{i}}/N_{\mathrm{f}})}$ where $D_{\mathrm{f}}(D_{\mathrm{i}})$ and $N_{\mathrm{f}}(N_{\mathrm{i}})$ are the final (initial) phase space density and number of atoms respectively.

[6] As discussed in Section 1.3

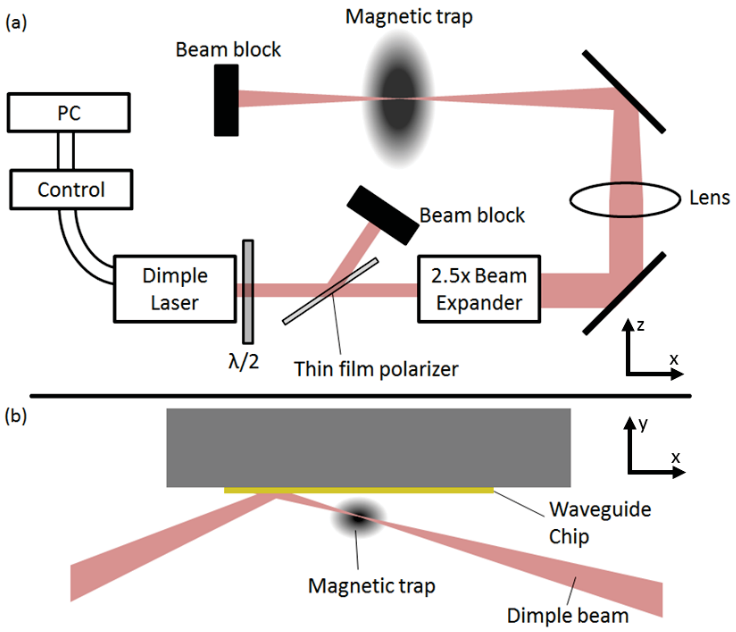

Figure 5.4.: The implementation of the hybrid trap on our experiment. (a) shows the path of the dimple beam from laser to atom cloud. (b) shows the path of the beam inside our vacuum chamber.

5.2.2. Experimental setup

Design

The laser used to generate the dimple is a commercial Innolight Corona laser. Using a diode-pumped solid state amplifier the laser emits a 1030 nm beam with an output power of 8 W at its maximum safe current of 6.1 A. To prevent the laser from heating up during operation without using a fan we have attached it to an aluminium heatsink. We have installed a $\lambda/2$ waveplate immediately in front of the output of the laser, followed by a thin film polariser oriented at 56° to the beam path, as shown in Figure 5.4. By adjusting the waveplate we can therefore redirect around 98% of the laser power into a beam dump.

Characterisation

The current of the laser can be modulated using an inbuilt system controlled by a voltage input, which we can control using our computer control software. The speed of this modulation was measured using a photodiode. When the laser current is increased above the threshold current at 1.3A to a set value, the power rises with a $1/e$ rise time of 60μs. When switching from 0W to 4W, the power overshoots 4W in 60μs before stabilising in around 50μs. When switching to powers over 5W, the laser reaches 5W in 60μs and then increases up to full power over several milliseconds. These issues appear to be mitigated by ramping the control voltage over a few milliseconds instead of stepping it. When the voltage is stepped down from any value to below threshold the power decreases with a $1/e$ fall time of 46μs.

The manufacturers of the laser quoted a $1/e^2$ beam waist of 1.25mm, with an M^2 of less than 1.3. We have installed a 2.5X beam expander after the polariser, which gives a beam waist of 3.46 mm as measured using a knife edge and translation stage. Using a 300 mm focal length lens to focus the beam after it has been expanded and performing knife-edge measurements of the spot size at several points along the path of the beam shows that the M^2 value is actually about 1.1, and that the waist using this lens is 26.5 μm.

This beam waist is smaller than the 50 μm waist we were aiming for. Due to concerns that a small waist will inhibit atoms loading into the trap, we will start off using a lens with a focal length of 500mm instead of 300mm to ensure the waist is around 50 μm.

Damage Tests

The magnetic trap we focus the laser onto is positioned 0.5 mm below the chip, and the laser must miss the V-groove assemblies on either side of the chip that extend 1 mm below it. This restricts the minimum angle between chip and beam to 2°, and in practice the angle we use is 10°. As a result, the beam hits the chip several millimetres past its focus. To determine if this can damage the chip, we performed tests using chips from previous experiments.

Firstly, we tested the beam on a chip with a gold surface identical to that of the chip currently in use. The beam was aligned onto the chip (outside vacuum) at an angle of 32° and focussed using a 300 mm lens on a translation stage. The scatter from the laser spot on the chip was observed using a CCD camera identical to the one we use to image atoms in the vacuum, and we minimised the size of this spot with the lens translation stage to find the exact position of the focus. With the laser focussed on the chip at 7.3 W (giving a spot size of 26.5 μm and an intensity of 340 kWcm^{-2} at the chip according to the knife edge measurements performed earlier), no effect is visible for around 1s, at which point the shape of the spot changes suddenly and dramatically, scattering a lot more light and continuing to change shape in bursts for a few more seconds. Additionally, a small glowing point is visible on the chip with the naked eye[7] once the change starts.

This change also affects the profile of the beam after it is reflected from the surface, changing it from a Guassian shape to resemble an Airy pattern, suggesting the laser is damaging the gold surface over a circular area. Focussing the laser on the chip and stepping up the power every 3 minutes shows the first visible damage occurring at 5.3 W after 40s of exposure. Moving the focus to 3 mm in front of the chip (giving a spot size of 43.5 μm and an intensity of 126 kWcm^{-2}) still damages the surface, except the damage occurs after 30 s of exposure. Moving the focus to 4 mm away (giving a spot size of 53.1 μm and an intensity of 84 kWcm^{-2}) damages the chip in around 3.5 minutes, and moving it to 6 mm (giving a spot size of 74.0 μm and an intensity of 43.6 kWcm^{-2}) shows no damage after 10 minutes of exposure. Each measurement required some refocussing, as moving the spot across the chip to an undamaged location also moves it slightly away from the focus.

Following the damage tests we examined the chip using a microscope; Figure 5.5 shows several marks produced in a series of preliminary tests. The marks appear as elliptical rings with a dark centre, possibly indicating that the laser damage has removed the gold surface to expose the silica underneath. Tests were also performed with the chip positioned at a more grazing angle to the beam, at 13°. At this angle no burning was observed at the focus at 7.3 W.

To examine the effects of the laser hitting the silica, we subsequently performed damage tests on a chip similar to ours but with the gold surface (and the chromium beneath) removed using aqua regia. Focussing the laser onto the silica at 7.5 W for around 1s produces an increase in scattering like that observed on the gold, although with the silica the increase is not as abrupt, occurring over several seconds. Moving the focus away from the chip and repeating the test showed damage still occurring when the focus

---

[7] Through safety goggles, of course.

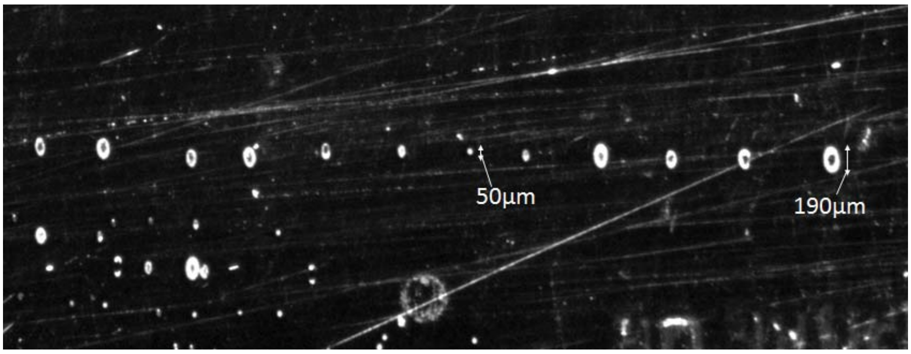

Figure 5.5.: Microscope image of the chip surface following preliminary damage tests. In these tests the laser was not refocussed after each run, and it can be clearly seen moving in and out of focus as it moves across the chip.

was 20 mm away, with the increase in scattering still starting after only a few seconds.

Examining the chip with a magnifying glass showed damage marks in the form of solid ellipses, which appear to be around 500 μm in diameter (larger than the laser spot). The marks did not appear to be cavities in the surface but instead areas of different refractive index. Since the waveguides in the chip are only 10 microns below the surface, this damage poses a significant danger to their operation.

The results of these tests show that we will need to take precautions to avoid damaging the gold directly above the waveguides, as this inevitably entails damaging the silica below. As it will only take a small misalignment of the beam to place its point of impact on the chip within 6 mm of its focus, we rotate the beam about the y axis to prevent it from heating the gold above the waveguides. Additionally, due to the low damage threshold of the silica it is essential to ensure that the dimple laser does not enter the trench at high power and damage the waveguide facets.

5.3. First Dipole Trap Signals

With the beam directed into the chamber, the next challenge was to align it with the magnetic trap. The lens used to focus the beam was mounted on two translation stages to permit fine adjustment of the alignment on two axes (chosen to be the x and y axes - the two axes in which the magnetic trap

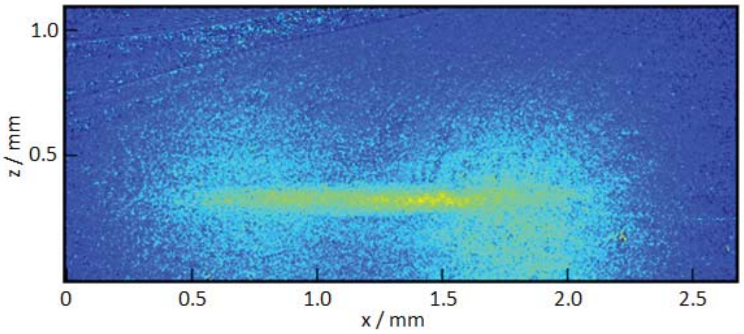

Figure 5.6.: Absorption image of one of the first MOT-loaded dipole traps produced using the dimple beam. The long horizontal cloud comes from the optical dipole trap. The clouds visible on the left and right of the dipole trap are the remnants of the MOT and its reflection respectively.

has its smallest dimensions). The beam path through the chamber could be roughly determined by looking at the position of the infrared scatter where the beam reflects off the chip, and the orientation of the beam as it passes out of the chamber. However, this does not provide anywhere near the precision needed to align the beam (which has a waist of 50 μm) with the compressed magnetic trap (which is around 600 μm long and 100 μm in diameter). To get a more precise idea of where the beam is, we aligned the beam roughly so that its focus lay just below the centre of the chip and then used the MOT to load the dipole trap at the beam focus in order to determine its exact position. Unlike the magnetic trap, the MOT can be moved around a large volume simply by ramping the magnetic fields after it has been loaded, allowing us to explore the entire region in which the beam focus lies.

After moving the MOT to the desired position, we tested for the presence of the optical dipole trap by switching off the MOT, then immediately switching on the dimple beam. The beam is held on for around 30 ms to give time for the MOT atoms that were not captured to fall away, so as not to obscure the atoms held in the dipole trap. It is then switched off and the atoms are imaged after 0.1 ms time-of-flight. One such image is shown in Figure 5.6. The path of the beam could be precisely determined from such images, along with the position of the beam focus and the axial trapping frequency (discussed further in Section 5.3.2).

5.3.1. Loading the Dimple from the Magnetic Trap

Loading from the compressed trap

Using images of MOT-loaded dipole traps, we were able to align the dimple beam with the centre of the compressed magnetic trap to within about 10 μm (limited by the resolution of the CCD camera used to take absorption images).

Unlike with the MOT, simply switching off the magnetic trap and immediately switching on the dipole trap did not trap enough atoms to see, presumably because the magnetically trapped cloud is much hotter than the MOT cloud (280 μK compared to 40 μK) and has fewer atoms (2×10^7 compared to 7×10^7). Overlapping the two traps for several seconds similarly did not show any loading taking place. Only when some evaporation was performed on the cloud (cooling it to around 50 μK in 3 s) with the dimple beam held on throughout did the dimple clearly load, with higher beam powers trapping more atoms, as shown in Figure 5.7.

To fine-tune the alignment of the dimple beam, we maximised the proportion of atoms loaded into the dimple (following an evaporation ramp that cooled the cloud to around 110 μK) by varying the lens position and the angle of the mirror that reflects the beam into the vacuum chamber. Less precise alignment was necessary along the long z axis of the magnetic trap and could therefore be achieved by simply examining absoprtion images of the hybrid trap. Figure 5.8 shows three such absorption images, taken *in situ* (i.e. both the optical trap and the magnetic trap were still present during imaging), from a hybrid trap with around 30% of the atoms loaded into the dimple. The Zeeman and Stark effects shift the resonant frequencies of the atoms, allowing some mapping of the shape of the hybrid potential, similar to that demonstrated by Brantut *et al.* in [80]. The part of the cloud with high resonant absorption frequencies occupies a region that is roughly 50 μm by 50 μm, around the spot size of the dimple beam. The highest frequencies at which atoms were visible were around 18 MHz above the free space resonance frequency.

Another potential method for optimising beam alignment involves maximising the increase in cloud temperature when the dimple beam is switched on - an effect that can be magnified by rapidly flashing the beam on and off at a frequency proportional to the axial trap frequency. While some

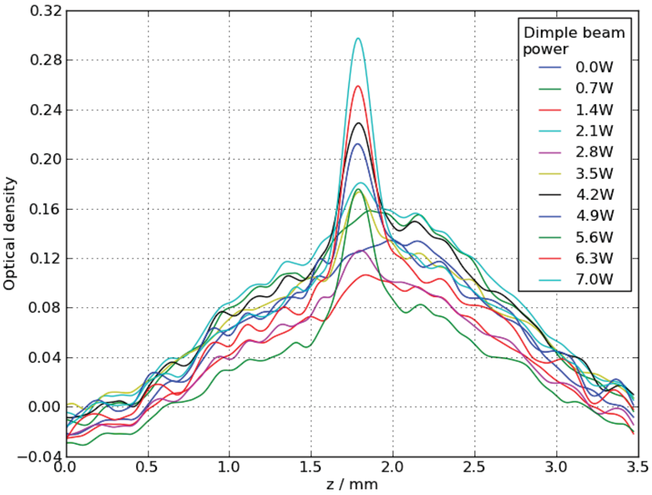

Figure 5.7.: The optical densities from absorption images taken perpendicular to the long axis of the magnetic trap, integrated over the transverse axis of the magnetic trap and averaged four times for ten different dimple beam powers. To make the signal from the dipole trap clearer the magnetic trap was switched off 5 ms before switching off the dimple beam, and the image was taken 0.5 ms after switching off the dimple beam. The remnants of the magnetic trap constitute a broad Gaussian distribution, and the atoms loaded into the dimple can be seen producing a much narrower peak (with a σ of 150 μm) at the centre of the Gaussian.

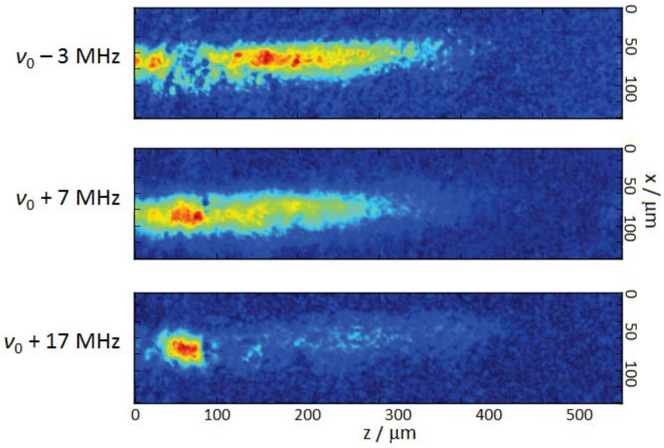

Figure 5.8.: *In situ* absorption images of a hybrid trap with loaded dimple at three different imaging light frequencies, here stated relative to ν_0, the free space resonant frequency of the $F_\mathrm{g} = 2 \rightarrow F_\mathrm{e} = 3$ transition. The dimple was formed within the compressed magnetic trap, so the trapping frequencies of the magnetic confinement here are $420 \times 420 \times 30$ Hz. Atoms in the dimple region have their resonant frequencies shifted by the Stark effect, rendering them transparent to the frequencies used to image the atoms in the purely magnetic regions of the trap (which are themselves shifted by the Zeeman effect), and vice versa.

measurements of this type appeared to show a maximum in temperature increase at certain lens positions, the results were ultimately too noisy to be of much use.

With the beam position aligned as closely as possible to the centre of the magnetic trap and a rf ramp optimised for loading, the maximum number of atoms we could load into the dimple was around 10^5. The number in the dimple can be found by simply switching off the magnetic trap while holding the dimple beam on. After around 20 ms all the untrapped atoms will have fallen away, leaving only those held by the dimple. These exhibit damped breathing oscillations around the beam focus.

Modelling Clouds in the Hybrid Trap at Thermal Equilibrium

To improve our understanding of the dimple loading process, it is useful to consider the thermal equilibrium state of an atom cloud confined in the combined trap system. The total hybrid trap potential U_D can be written as

$$U_\mathrm{D}(x, y, z) = U_\mathrm{MT}(x, y, z) + U_\mathrm{ODT}(x, y, z), \tag{5.11}$$

where U_{ODT} is the optical dipole trap potential and U_{MT} is the magnetic trap potential. The magnetic trap is assumed to be perfectly harmonic, so that

$$U_{\mathrm{MT}}\left(x,y,z\right)=\frac{m_{\mathrm{Rb}}}{2}\left(\omega_{\mathrm{r}}^{2}\left(x^{2}+y^{2}\right)+\omega_{\mathrm{z}}^{2}z^{2}\right). \tag{5.12}$$

U_{ODT} is given by

$$U_{\mathrm{ODT}}\left(x,y,z\right)=-\frac{1}{2\epsilon_{0}c}\mathrm{Re}\left(\alpha\right)I\left(x,y,z\right), \tag{5.13}$$

where α is the complex polarizability. For now, we can approximate α by integrating the equation of motion for an electron undergoing driven oscillation in an electric field[8], giving

$$\alpha=\frac{e^{2}}{m_{\mathrm{e}}}\frac{1}{\omega_{0}^{2}-\omega^{2}-i\omega\Gamma}. \tag{5.14}$$

where Γ is the linewidth of the transition, e is the electron charge and m_{e} the mass of the electron. Using this expression in equation 5.13 gives

$$U_{\mathrm{ODT}}\left(x,y,z\right)=-\frac{3\pi c^{2}}{2\omega_{0}^{3}}\left(\frac{\Gamma}{\omega_{0}-\omega}+\frac{\Gamma}{\omega_{0}+\omega}\right)\left(I\left(x,y,z\right)-I_{0}\right) \tag{5.15}$$

where ω_0 is the angular frequency of the rubidium D_2 transition, ω is the angular frequency of the trapping light, and I_0 is the peak intensity of the trapping light beam. $I\left(x,y,z\right)$ is the intensity of the trapping light. Assuming a Gaussian beam directed along x,

$$I\left(x,y,z\right)=I_{0}\left(\frac{w_{0}}{w\left(x\right)}\right)^{2}\exp\left[-\frac{2\left(y^{2}+z^{2}\right)}{w^{2}\left(x\right)}\right], \tag{5.16}$$

and

$$I_{0}=\frac{2P}{\pi w_{0}^{2}} \tag{5.17}$$

where P is the total beam power and w_0 is the beam waist. $w\left(x\right)$ is the spot size of the beam, given by

$$w\left(x\right)=w_{0}\sqrt{1+\left(\frac{x}{x_{\mathrm{R}}}\right)^{2}}, \tag{5.18}$$

---

[8] A more detailed treatment of polarizability is given in Section 6.4.4.

where the Rayleigh range of the beam $x_{\mathrm{R}} = \pi w_0^2/\lambda$ and λ is the wavelength.

We can obtain expressions for the trap frequency in dimension r of the optical trap[9] by performing a series expansion of U_{ODT} and comparing the r^2 term to the standard harmonic trap expression $U = \frac{1}{2}m\omega^2 r^2$. Using this approach we find the radial frequency (in y and z) to be

$$f_{\mathrm{r}} = \sqrt{\frac{\mathrm{Re}\,(\alpha)\,P}{m\pi^3 w0^4 \epsilon_0 c}}, \tag{5.19}$$

while the axial frequency (in x) is given by

$$f_{\mathrm{x}} = \sqrt{\frac{\mathrm{Re}\,(\alpha)\,P}{2m\pi^3 w_0^2 x_{\mathrm{R}}^2 \epsilon_0 c}}. \tag{5.20}$$

The trap depth is given by $\mathrm{Re}\,(\alpha)\,I_0/(2\epsilon_0 c) = \mathrm{Re}\,(\alpha)\,P/(\pi w0^2 \epsilon_0 c)$.

If the cloud is at thermal equilibrium, the number density distribution $n\,(x, y, z)$ is given by the Boltzmann distribution such that

$$n\,(x, y, z) = n_0 \; e^{-U_{\mathrm{D}}(x,y,z)/k_{\mathrm{B}}T}, \tag{5.21}$$

where T is the temperature and n_0 is the peak density, given by

$$n_0 = N \left(\int_{-\infty}^{\infty} dx \int_{-\infty}^{\infty} dy \int_{-\infty}^{\infty} dz \; e^{-U_{\mathrm{D}}(x,y,z)/k_{\mathrm{B}}T} \right)^{-1}, \tag{5.22}$$

thus normalising Equation (5.21). We evaluate Equation (5.22) numerically using the Python package `scipy.integrate.tplquad`, choosing appropriate (empirically determined) bounds for x, y and z.

Given the normalised density distribution $n\,(x, y, z)$ we can calculate the expectation value of a quantity $Q\,(x, y, z)$ per atom directly:

$$\langle Q \rangle = \frac{1}{N} \int_{-\infty}^{\infty} dx \int_{-\infty}^{\infty} dy \int_{-\infty}^{\infty} dz \; n\,(x, y, z)\, Q\,(x, y, z)\,. \tag{5.23}$$

We have used this method to calculate the elastic collision rate[10] and heating

---

[9] The trap is not harmonic, of course, so these frequencies are only valid at the centre of the trap.

[10] Given by $\Gamma_{\mathrm{coll}} = n\,(x, y, z)\,\sigma_{\mathrm{el}}\bar{v}_{\mathrm{rel}}$ where σ_{el} is the elastic scattering cross section (given in Equation (5.29)) and $\bar{v}_{\mathrm{rel}}$ is the average relative velocity, given by $\sqrt{2}v_{\mathrm{rms}} = \sqrt{6k_{\mathrm{B}}T/m_{\mathrm{Rb}}}$.

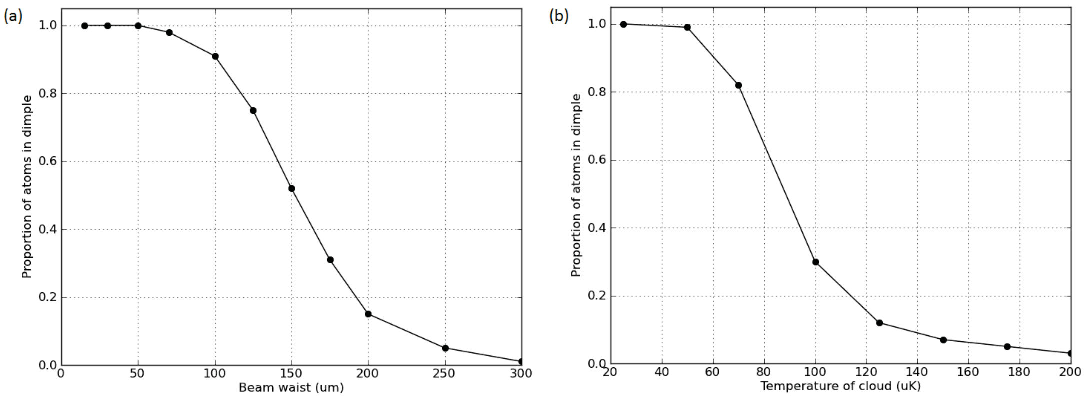

Figure 5.9.: Results from the thermal equilibrium model demonstrating the importance of (a) a small beam waist and (b) a cold cloud for high dimple populations. The temperature of the trap in (a) is 50 μK and the beam waist in (b) is 30 μm. The magnetic trap frequencies for both sets of calculations are 120 Hz radially and 30 Hz axially.

rate due to spontaneous emission[11] in the hybrid trap. The number of atoms loaded into the dimple can also be ascertained, by integrating over the density of atoms with potential energy less than $\frac{3\pi c^2}{2\omega_0^3}\left(\frac{\Gamma}{\omega_0-\omega}+\frac{\Gamma}{\omega_0+\omega}\right)I_0$.

This model does not quite match the results obtained so far with the dimple in the compressed magnetic trap, suggesting that either the system is not reaching thermal equilibrium over the time we can observe it (before most of the atoms are lost to background gas collisions) or the alignment is not optimal. However, we can still draw some general conclusions from the results. It is clear that a tighter beam waist results in a higher proportion of atoms being loaded. Additionally, the model shows that the temperature of the cloud before the traps are overlapped is of crucial importance in loading the dimple, with cold clouds loading a far greater proportion of their atoms into the dimple than hot clouds. These effects are shown in Figure 5.9.

Loading from a decompressed trap

Following the results of the thermal equilibrium model, the experimental procedure was altered so that after loading the magnetic trap from the MOT, the Z bias field is ramped up adiabatically, decreasing the radial trap frequency and cooling the cloud. The dimple beam was realigned so that the

---

[11] Given by $G(x,y,z)\times E_{\mathrm{rec}}/k_{\mathrm{B}}$ where E_{rec} is the recoil energy and $G(x,y,z)$ is the photon scattering rate, equal to $(\hbar\epsilon_0 c)^{-1}\mathrm{Im}(\alpha)\,I(x,y,z)$.

focus now intersected this decompressed trap rather than the compressed trap close to the chip surface. Additionally, the beam waist was reduced by replacing the 500 mm focal length lens with a 250 mm lens, the shortest focal length possible given the dimensions of our vacuum chamber. The alignment was much less sensitive with the decompressed trap due to the larger cloud size. Brief experiments that looked at loading the tighter dipole trap from the MOT showed trapped atoms remaining held for 600 ms — much longer than with the 500 mm lens, which were not visible for longer than 100 ms.

Using this new procedure, rf cooling was no longer necessary; just overlapping the two traps and leaving some time for the atoms to rethermalize was enough to load a substantial number into the dimple. Figure 5.10 shows that the dimple population increases rapidly at first as rethermalization occurs, followed by a slower decay once the rethermalization rate drops below the background loss rate. Similar behaviour was observed by Sofikitis *et al.*[81].

Decreasing the trap frequency to cool the trap also entails reducing the collision rate of the trap, which increases the rethermalization time, thereby reducing the maximum number of atoms that can be loaded into the dimple. The need for a tradeoff between collision rate and temperature suggests there is an optimal radial frequency for loading. Figure 5.11 shows the number loaded into the dimple after 3 s of overlap time for a range of magnetic trap radial frequencies, with a clear maximum occurring at around 120 Hz, where the magnetically trapped cloud has a temperature of 85 μK and a collision rate of about 3 s^{-1}. This radial frequency is achieved by decreasing the Z bias field by 13 G over 50 ms, after the magnetic trap has been loaded.

The results are compared with results from thermal equilibrium model, which agree at higher frequencies but differ dramatically at lower frequencies, suggesting that here the trap is not reaching thermal equilibrium in the 3 s of overlap time. It is therefore unsurprising that the optimal frequency is close to the point at which experiment and theory diverge, where the overlap time is only just long enough to let the cloud get close to thermal equilibrium. These measurements were performed for a range of overlap times; the global optimum is at 3 s overlap time and 120 Hz radial frequency.

Using the decompressed trap we were able to load around 10^6 atoms

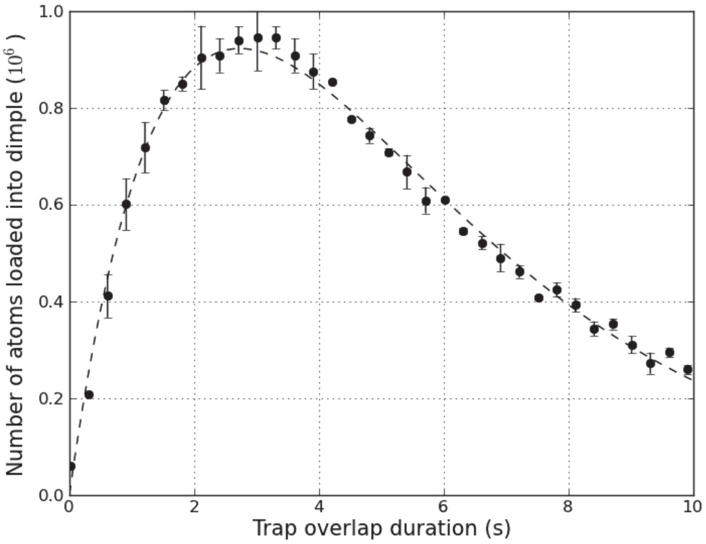

Figure 5.10.: Experimental results showing the dimple loading via rethermalization. No rf was applied, the magnetic trap and dipole trap were simply overlapped and the number in the dimple was measured 20 ms after releasing the magnetic trap. The data are fitted to the equation $N(t) = N_0 \left(1 - e^{-t/\tau_{\mathrm{RT}}}\right) e^{-t/\tau_{\mathrm{loss}}}$ where N_0 is the thermal equilibrium dimple population, τ_{RT} is the rethermalization time and τ_{loss} is the trap lifetime. For this fit $\tau_{\mathrm{RT}} = 1.1 \pm 0.1$ s and $\tau_{\mathrm{loss}} = 5.1 \pm 0.2$ s.

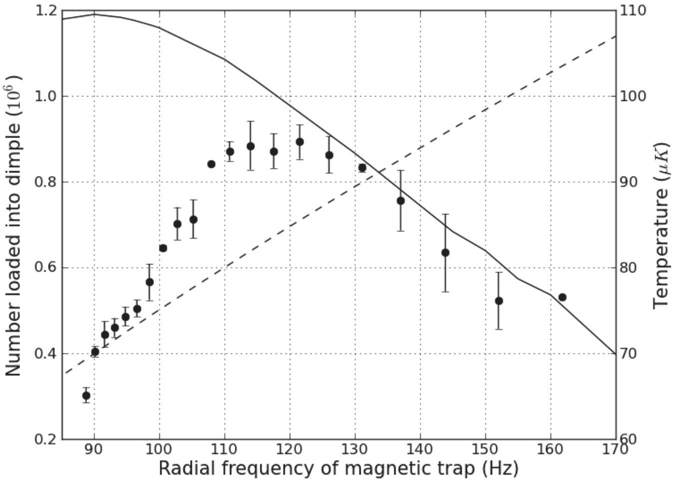

Figure 5.11.: Experimental results showing the number of atoms loaded into the dimple after 3 s of trap overlap for various radial trap frequencies, compared with results from the thermal equilibrium model (black line). The temperature of the cloud at each trap frequency is also shown (dashed line).

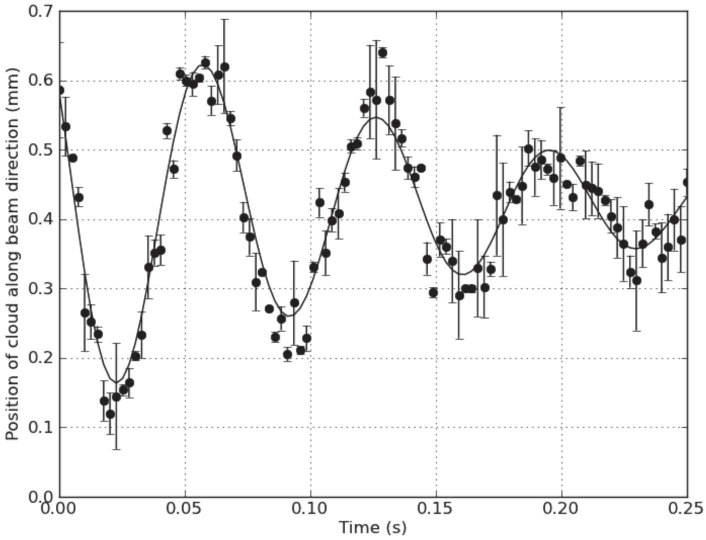

Figure 5.12.: Results of a measurement of the axial frequency of the dipole trap with a beam power of 8 W. The data are fitted to the curve $A \sin(2\pi f t) \exp(-t/\tau)$ where $A = 0.3$ mm, $f = 14.8$ Hz and $\tau = 0.147$ s.

into the dimple, a factor of 10 more than we achieved using the compressed trap.

5.3.2. Dipole Trap Characterisation

The axial frequency of the dipole trap can be determined by simply imaging the atom cloud held in the beam once it has been loaded from a MOT or magnetic trap positioned slightly away from the beam focus, and measuring how the centre of the cloud moves over time. The cloud centre oscillates around the beam focus at a frequency of 14.8 Hz with a decaying amplitude as dephasing occurs, as shown in Figure 5.12.

We were unable to observe oscillations in the transverse direction, probably due to their high frequency and small amplitude. However, the transverse frequency could be measured by oscillating the beam power once the trap was loaded, and measuring the heating rate as a function of oscillation frequency. Oscillating the beam power at twice the frequency of the trap should produce the highest heating rate[82].

With the beam propagating horizontally, we also expect a peak in the heating rate when the beam power is oscillated at the trap frequency, arising from the dependence of the trap centre's position on beam power; if the beam power is increased the optical force opposes the downwards force from gravity more, so the trap centre moves upwards (in y), and as the power is decreased the trap centre moves down. Oscillating the power therefore oscillates the trap's position in y, which will heat the cloud if performed at the trap's radial frequency.

Due to control software limitations we were unable to oscillate the power at frequencies above 2.5 kHz — frequencies around this cutoff value were measured as the beam power approached 3 W. However, measurements at powers between 0.5 W and 2.5 W show clear peaks in heating rate. Despite expecting peaks at both the trap frequency and twice the trap frequency, we only observe one peak experimentally, indicating that one of the heating processes described above is much stronger than the other. Comparing the peak positions with predicted results (using equation (5.19)) suggests that the movement of the trap centre is the dominant effect, so the visible peaks are at the trap frequency. We expect the frequency to vary as the square root of the beam power, and by fitting a curve to these points and extrapolating, we find the expected frequency at 8 W to be 3.7 kHz. The results of these measurements are shown in Figure 5.13.

The axial and transverse frequency measurements suggest a beam waist of about 33 μm (using equations (5.19) and (5.20)), larger than expected, given the initial waist of 3.46 mm and the 250 mm focal length lens. This waist corresponds to an M^2 value of around 1.4 instead of 1.0, suggesting the beam is being somewhat distorted as it enters the chamber, possibly by the vacuum chamber window.

5.4. Cooling in the Hybrid Trap

A number of cooling strategies are possible once the dimple has been loaded. This section compares four strategies we have investigated.

5.4.1. All-Optical Cooling

The most straightforward strategy is to adiabatically switch off the magnetic trap, leaving only the atoms loaded into the dimple and then cooling these

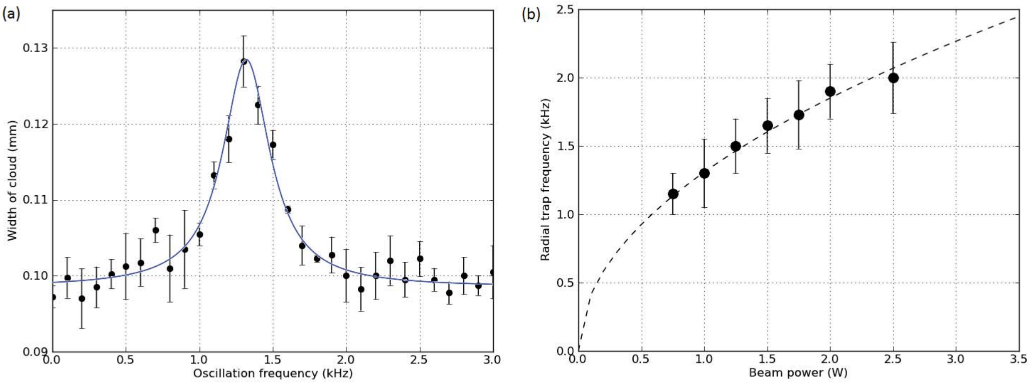

Figure 5.13.: Measuring the radial frequency of the dipole trap. (a) The width of the cloud (which is proportional to its temperature) 8 ms after the trap has been switched off. Prior to switching off the beam power was oscillated by ±0.1 W for 500 ms. The measurement here was performed for a 1 W trap. A lorentzian curve (blue) is fit to the data , with a FWHM of 180 MHz. (b) Several trap frequency measurements for different beam powers. The frequencies fit a square root curve (dashed line) which suggests the frequency at 8 W is 3.7 kHz.

atoms by carefully reducing the beam power, using the reduction in trap depth to truncate the energy distribution, as described in Section 5.1.1.

With around 10^6 atoms in the dimple, ramping down the currents in the bias and Z wires causes atoms held in the magnetic trap to fall away, leaving the atoms in the dimple at a temperature of around 100 μK. However, the number in the dimple also rapidly decreases following the switch off of the magnetic trap; in only 500 ms, the number has reduced to 5×10^5. This is the result of the reduction in trap depth — the magnetic trap has a depth of a few mK, whereas the dipole trap's depth at 8 W is only 500 μK, only 5 times greater than the temperature of the cloud. This leads to rapid loss and some cooling.

The dipole trap's effective depth is 500 μK because of the effect of gravity; to avoid the V-groove structures and intersect the magnetic trap, the beam is oriented at 10° to the horizontal. This means that a force of $m\ g \sin(10°)$ acts along its axis, directed towards the lower end, reducing the trap depth (at this end) from around 750 μK to around 500 μK at 8 W[12]. The variation of the depth of the dipole trap with power for a num-

---

[12] The effect of gravity on the potential also shifted the centre of the atom cloud held in the dipole trap away from the focus. This had to be taken into account earlier, when the beam was aligned with the magnetic trap.

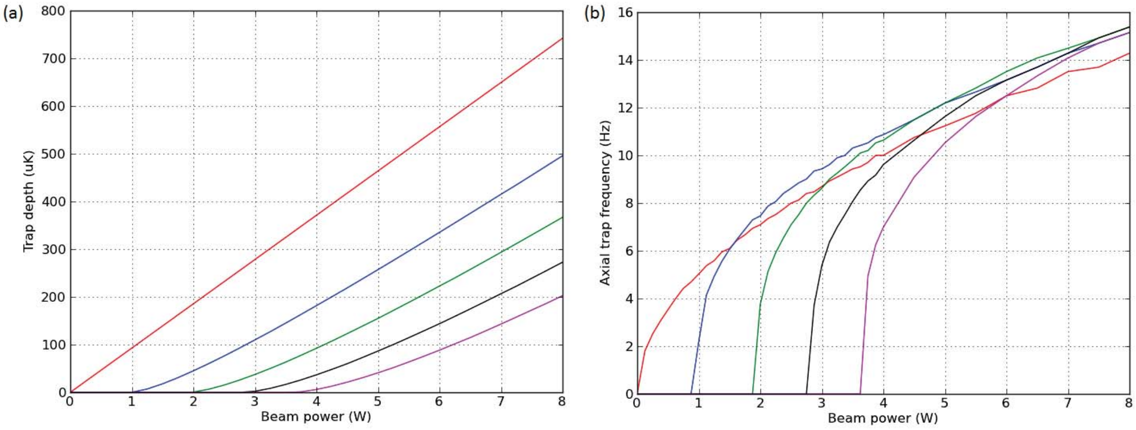

Figure 5.14.: Results obtained from a simple Gaussian beam model showing (a) the depth of our dipole trap with power and (b) the axial trap frequency with power. The calculations were performed for five angles between the beam and the horizontal axis; 0° (red), 10° (blue), 20° (green), 30° (black) and 40° (magenta). With an angle of 90° the beam will only form a trap when its power is greater than 6 W.

ber of beam angles relative to the horizontal axis is shown in Figure 5.14a. The effective axial trap frequency is also reduced by gravity, as shown in Figure 5.14b.

The current imaging system probes the chamber perpendicular to the direction of the beam, so an atom cloud held in the dipole trap will not be imaged along its long axis as with the magnetic trap, meaning optical densities are around 0.5 after 0.5 ms time-of-flight, significantly lower than those achievable with the magnetic trap (which once loaded has an optical density of around 4.5 after 3 ms time-of-flight). The low optical density means that time-of-flight temperature measurements are difficult to perform (and the rf spectroscopy method is unavailable for a purely optical trap).

This combined with the initial dramatic atom loss makes optimizing an evaporation process using just the dipole trap very difficult. Evaporating entails removing more atoms from the trap as well as decompressing the cloud, reducing the optical density even further. The coldest temperature achieved using this all-optical method was about 50 μK, beyond which the optical density was too low to produce reliable images. An additional drawback of this method if used as part of a larger experiment involving use of the trench is that the cloud would have to be loaded back into the magnetic trap once cooled, likely resulting in heating and requiring movement of the beam focus during the experiment.

5.4.2. Cooling using Isentropic Trap Deformation

Relating Phase Space Density to Trap Shape

As mentioned in Section 5.4.1 the temperature of the cloud in the dimple is about 100 μK, about the same temperature as the magnetically trapped cloud. With 10^6 atoms in the trap, this corresponds to a phase space density of around 1.5×10^{-4}, significantly higher than the phase space density of the cloud before the dimple is loaded (3×10^{-7}).

This increase in phase space density occurs as a result of the change in shape of the trapping potential, as first discussed by Ketterle and Pritchard[83]. Pinkse *et al.* have shown that interatomic collisions are essential if such changes are to affect phase space density[84].

We can quantify the shape of a trapping potential by introducing a 'deformation parameter' γ, which is related to the total energy E of a cloud of N trapped atoms;

$$E = N k_{\mathrm{B}} T \left(\gamma + \frac{3}{2}\right). \tag{5.24}$$

where T is the temperature of the cloud. Rearranging equation (5.24), we see that γ represents the mean potential energy per particle in units of the thermal energy. Its value depends on the shape of the trapping potential and is a global property of the system.

If we define an effective volume V_{e} for the system so that $V_{\mathrm{e}} = n_0/N$ where n_0 is the peak density of the cloud, we can also write γ as

$$\gamma = \frac{T}{V_{\mathrm{e}}} \frac{\partial V_{\mathrm{e}}}{\partial T}. \tag{5.25}$$

Crucially, we can relate the phase space density $n_0 \lambda_{\mathrm{dB}}^3$ to γ;

$$n_0 \lambda_{\mathrm{dB}}^3 = \exp\left(\gamma + \frac{5}{2} - \frac{S}{N k_{\mathrm{B}}}\right), \tag{5.26}$$

where S is the entropy of the cloud. This suggests that if γ can be increased without increasing S or decreasing N that much, we can increase $n_0 \lambda_{\mathrm{dB}}^3$. Specifically, if $\gamma - \frac{S}{N k_{\mathrm{B}}}$ can be increased by δ, $n_0 \lambda_{\mathrm{dB}}^3$ will increase by a factor of $\exp(\delta)$. The derivation of this relationship along with a more detailed introduction to the deformation parameter are given in Appendix A.

To avoid large increases in S we need to ensure that our changes to the system are slow enough to be adiabatic and reversible (i.e. isentropic). Changes to trapping potentials are generally adiabatic if they are performed over a time greater than the oscillation period of the trap τ_{osc}[85] — this ensures the change does not drive transitions between bound states. For the change to be reversible we need to ensure that the system stays close to thermal equilibrium throughout the change, so there is another time scale that must be taken into account; the rethermalization time, τ_{RT}. If the change is performed over a time much greater than τ_{RT} then the system should remain at thermal equilibrium throughout, without an increase in entropy. The rethermalization time is a few times the collisional lifetime: $\tau_{\mathrm{RT}} \approx 4\tau_{\mathrm{el}}$. The constant of proportionality is not exact, and different studies on evaporative cooling suggest values in the range 2 - 4[86, 87, 75, 88, 89].

Calculating the Deformation Parameter for a Given Trap

For a given single particle trapping potential $U(\mathbf{r})$, γ can be found by calculating the mean potential energy, so that

$$\gamma = \frac{\int \mathrm{d}^3\mathbf{r}\ [U(\mathbf{r}) - U_0]\ e^{-[U(\mathbf{r})-U_0]/k_{\mathrm{B}}T}}{k_{\mathrm{B}}T \int \mathrm{d}^3\mathbf{r}\ e^{-[U(\mathbf{r})-U_0]/k_{\mathrm{B}}T}}, \tag{5.27}$$

where U_0 is the minimum of the trapping potential.

For power law traps this integral can be calculated analytically; for a harmonic trap γ is $3/2$, and independent of temperature[13]. In the case of our hybrid trap γ can only be calculated numerically, and it is a function of temperature, beam power, beam waist and magnetic trap frequencies. For a magnetic trap with $f_{\mathrm{r}} = 120$ Hz,$f_{\mathrm{z}} = 30$ Hz at a temperature of 100 μK with an 8 W beam with a 33 μm waist, γ is about 8.5.

Trap Deformation in Practice

These results suggest that if the dimple can be introduced isentropically, the phase space density should increase by a factor of $\exp(8.5 - 1.5) = \exp(7) \approx 10^3$. However, using the loading procedure described in Section

---

[13] A more general result is that for a power law potential of power m, $\gamma = 3/m$

5.3.1 we obtain a factor of about 500. The discrepancy between the expected value and the experimental value is mostly the result of atom loss during loading, as well as a contribution from the rapid switch-on of the dimple beam — we would expect a higher final phase space density if the beam power could be ramped up slowly, but the high pressure in our vacuum chamber prevents this.

The part of the atom cloud that remains in the purely magnetic regions of the trap loses atoms throughout the loading process, while staying at the same temperature. As a result, the value of $n\left(\mathbf{r}\right)\lambda_{\mathrm{dB}}^{3}$ is much lower in these regions than in the dimple. To retain only the atoms in the dimple it would be useful to have a way of removing the magnetically trapped cloud while avoiding the gravity-related atom loss that occurs in the purely optical trap, as described in Section 5.4.1. We find that ramping down only the Z wire current by about 20 A over 50 ms moves the magnetic trap away from the dimple beam and towards the atom chip, causing all the atoms not confined by the dimple to collide with the room temperature chip surface, ejecting them from the trap. As the magnetic trap centre does not move too far from the beam focus, some magnetic confinement is maintained along the beam axis, preventing gravity from forcing atoms out of the trap. Following this, the Z wire current is ramped back up over the next 50 ms to its original value of 50 A to restore full confinement along the x axis of the dimple beam. If this process is performed slowly enough, the atom population contained in the dimple is almost entirely unaffected, experiencing only a slight isentropic axial relaxation along the x axis followed by an isentropic compression. During this 'purification' process there is negligible atom loss from inside the dimple.

Following the removal of the atoms outside the dimple, the remaining 10^6 atoms inside the dimple experience a quasi-harmonic potential, and depending on their temperature, γ now ranges from 1.5-2.0 — at 100 μK γ is about 1.8. As we need the atoms to be in a purely magnetic trap in order to bring them into the trench, the dimple has to now be removed while maintaining (or ideally increasing) the phase space density. Isentropically ramping down the dimple from 8 W to 0 W over 2 s so that only the magnetic trap remains results in the cloud cooling to 10 μK with around 6×10^5 atoms remaining, with a phase space density of 2×10^{-5}, consistent with the drop in γ and atom loss over the 2 s. This phase space density is about the same as the highest we were able to achieve with evaporative cooling in the purely magnetic trap. We can, however, obtain increases in γ as the dimple power is reduced to 0 W, increasing the final phase space density.

Assuming the dimple beam power ramp is isentropic, we can look at how the value of γ changes throughout the ramp to 0 W using equation (5.27); the results are shown in Figure 5.15. γ increases during the first stage of the ramp as atoms repopulate the magnetic regions of the trap, reaching a value of 4 once the beam power is around 2.5 W, where around 60% of atoms remain in the dimple. γ subsequently decreases to 1.5 as the beam power reaches 0 W and the trap returns to a harmonic shape. We can therefore obtain an increase in final phase space density by repeating the purification process when the beam power reaches 2.5 W; this reduces γ back to 1.8, while preserving the increased phase space density at the centre of the trap. γ can then be raised again by continuing the reduction in dimple beam power, allowing the process to be repeated with successive increases in phase space density.

There are a few drawbacks to this approach. In practice the procedure eventually reaches a limit when the dimple power is sufficiently low that the movement of the centre of the magnetic trap during the purification process begins to overcome the confinement by the dimple, resulting in the removal of some of the atoms from the dimple instead of just the higher energy magnetically trapped atoms. At beam powers less than 0.45 W the dimple confinement is completely overcome by the magnetic force, and all atoms are removed from the system. We therefore observe a decrease in efficiency as the procedure continues, eventually reaching zero efficiency once the dimple power is less than 0.45 W.

There are also diminishing returns in the value of γ that is achievable by dimple power reduction. The initial loading of the dimple raises γ to around 8.5, but as the cloud cools and the dimple confinement reduces, the size of the magnetically trapped cloud approaches the size of the cloud in the dimple. This leads to a better mode-matching between the two regions and thus a lower value of γ. Equation (5.27) suggests this can be mitigated somewhat by decreasing the beam waist (which would require rebuilding the dimple setup with a zoom lens) or by decompressing the magnetic trap to expand the cloud (by decreasing the trap frequencies). Decompressing the

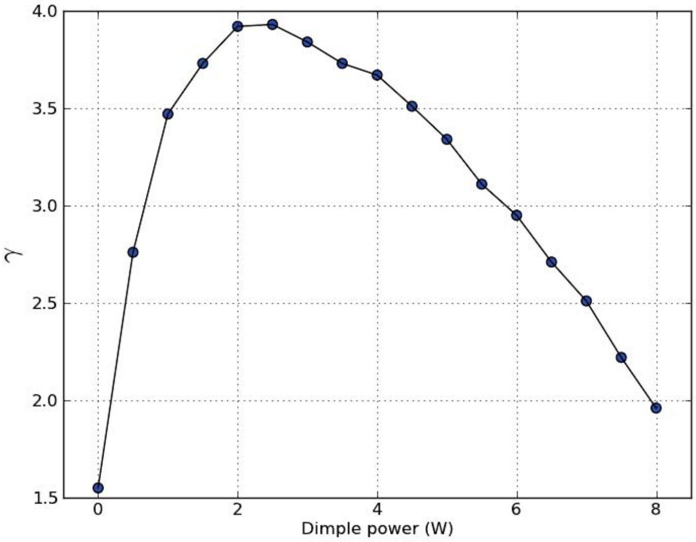

Figure 5.15.: Values of γ determined by numerically evaluating equation (5.27) for a range of dimple beam powers in the purified trap. The values of γ at 8 W and 0 W are around 3/2, reflecting the harmonicity of the populated regions of the trap at these powers. At intermediate powers, atoms populate both the dimple region and the magnetic region, resulting in a higher value of γ.

magnetic trap does not have a large effect, however, as the trap is also cooled by the decompression, partially counteracting the expansion. In addition to the reduction in maximum γ, the need for the beam ramps to be isentropic sets a limit on how fast the procedure can be performed, which is significant given the high rate of atom loss in our vacuum chamber.

We have developed a sequence of dimple power ramps and purifications using semi-analytical results from equation (5.27) and a Monte Carlo simulation (described in Section 5.5). This sequence uses 4 purifications in total, which are performed at dimple powers of 8 W, 3 W, 1 W and 0.7 W. Despite the constraints described above, this gives a final phase space density of 1.5×10^{-4} with 10^5 atoms remaining at a temperature of 3 μK. This phase space density is a factor of 10 higher than the highest we were able to achieve with evaporative cooling in the purely magnetic trap, and has 10 times more atoms remaining, potentially allowing for further evaporative cooling. The overall evaporation efficiency of this procedure up to this point is about 1.2 (where the initial state is taken as the initial magnetic trap before the loading of the dimple, so $N_{\text{initial}} = 2 \times 10^7$ and $D_{\text{initial}} = 3 \times 10^{-7}$). This is a factor of three times higher than the efficiency of 0.4 achieved with the rf-driven evaporative cooling described in Section 5.1.2.

5.4.3. Cooling the Cloud in the Hybrid Trap using rf Radiation

If the hybrid trap is purified after loading, all the atoms occupy the dimple region, and the cloud has a cigar shape where the light beam provides tight radial confinement with a trap frequency of 3.7 kHz and the magnetic trap provides 120 Hz axial confinement. The presence of magnetic confinement means that rf radiation could be used to cool the trap — if radiation of the right frequency is applied, atoms at a certain magnetic field strength can be coupled to untrapped states and thus be ejected along the long axis of the optical trap.

For the hybrid potential, the effect of the rf radiation is not as straightforward as it is in a purely magnetic trap. The shape of our purely magnetic potential without the dimple present is shown in Figure 5.16a. Figure 5.16b shows how the potential experienced by the atoms changes if rf radiation is applied; in the dressed atom picture, above a certain magnetic potential the sign of the magnetic force changes, so that atoms that reach this potential escape from the system. The contour of magnetic potential at which atoms escape is also a contour of the trapping potential.

The shape of the hybrid potential, with both magnetic and optical traps present, is shown in Figure 5.16c. The presence of the optical trap means that the contours of magnetic potential are not also contours of the trapping potential. If we apply rf radiation, the magnetic component of the trap changes shape (as in Figure 5.16b) but the optical trap is unaffected, so the total potential takes the shape shown in Figure 5.16d.

As mentioned above, following loading and purification, all the atoms occupy the central dimple region. As a result, the magnetic potential that is addressed by the rf can only be reached by atoms that reach the ends of the dimple region — the rf radiation does not eject atoms from the sides of the dimple. This makes our evaporation process one-dimensional, so that only the longitudinal motion of the atoms determines their escape from the trap. This limits the evaporation rate and therefore limits the evaporative cooling efficiency, as discussed by Surkov *et al.*[90] and Pinkse *et al.*[91].

Additionally, the mismatch between the escape contour and the trapping contours means the rf knife loses its selectivity - atoms with a range of potential energies are ejected from the trap. If we use a rf knife that ejects atoms at potential energy E_{RF} from the purely magnetic trapped cloud, the same knife applied to the purified hybrid trap will eject atoms at all potential energies between E_{RF} and $E_{\mathrm{RF}} + U_{\mathrm{D}}$ where U_{D} is the depth of the dimple potential[14]. This lack of selectivity also reduces our efficiency.

We find that the optimal procedure is to ramp down both the rf frequency and the dimple beam power simultaneously, such that E_{RF} is always roughly equal to U_{D}. This ensures that only atoms with enough energy to escape the dimple region are removed from the system. This way, we maintain a high interatomic collision rate while removing only the hottest atoms, resulting in efficient cooling and an increase in phase space density. This procedure resembles the typical evaporative cooling process used on all-optical systems (achieved by relaxation of the optical trap, allowing the escape of hot atoms) with the magnetic trap providing additional confine-

---

[14] This expression assumes that the Rayleigh length of the beam is significantly larger than the radial size of the magnetic trap, so that the depth of the dimple potential is relatively constant across the trap. For our system the Rayleigh length is 3.3 mm — significantly larger than the largest magnetically trapped cloud used in our experiment, which has a $1/e$ size of around 0.1 mm.

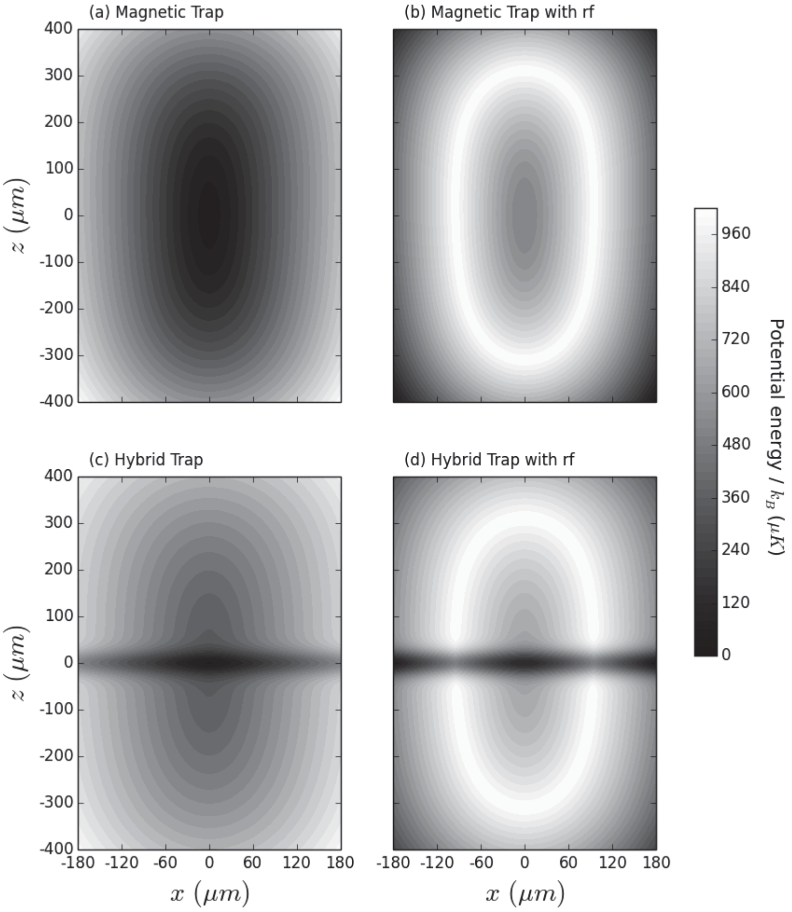

Figure 5.16.: 2D slice through the centre of the purely magnetic and hybrid potentials, when dressed with rf radiation (right) and with no rf radiation present (left). Lighter areas represent areas of higher potential energy. In (b) atoms need energy greater than E_{RF} to escape the system in any direction. In (d), the energy required to escape the system is $E_{\mathrm{RF}} + U_{\mathrm{D}}$ along the contour of the magnetic trap, where U_{D} is the depth of the dimple. Along the axis of the dimple beam, the energy required is lowered to just E_{RF}.

ment along the axis of the beam, and atom ejection boosted by the effects of rf radiation.

Optimising this procedure (using piecewise simultaneous ramps of both rf radiation frequency and dimple power) following the initial loading and purification and continuing it until the dimple power reaches 0 W results in 1×10^5 atoms remaining in the purely magnetic trap at a temperature of 5 μK, with a phase space density of around 5×10^{-4}. Following the initial purification, the magnetic trap is compressed back to its original trap frequency of 170 Hz, so this final phase space density is higher than the 1.5×10^{-4} achieved in Section 5.4.2 (where the frequency was 120 Hz throughout) despite the slightly higher temperature of 5 μK vs 3 μK. Simulations of this evaporation sequence show that γ remains at a relatively constant value of 2.0 throughout, implying the phase space density increase is primarily a result of the rf radiation ejecting atoms, rather than the changing shape of the trap. The evolution of atom number and temperature is shown in Figure 5.17. The selectivity of the rf knife increases as the power of the dimple beam decreases, resulting in an increase in evaporation efficiency. The overall efficiency of this procedure is 1.4.

5.4.4. Cooling the Cloud by offsetting the Traps.

Hung *et al.*[77] have demonstrated that an atom cloud in an optical trap can be efficiently cooled by 'tilting' the trap by superimposing a magnetic field gradient across the trap, lowering the trap depth at one side of the trap allowing energy truncation without the need for relaxation of the confinement. Clement *et al.* have developed a similar method using a misaligned crossed-beam trap configuration[78].

We can achieve something similar on our experiment. Once the hybrid trap has been loaded and purified, we can increase the Z wire current to 80 A to shift the centre of the magnetic trap away from the chip, introducing a magnetic field gradient across the dimple while maintaining some magnetic confinement along the axis of the beam, as shown in Figure 5.18. As the Z wire current is increased the depth of the dimple decreases on the side further from the chip, and atoms with sufficiently high energy escape the dimple and fall into the magnetic trap. We apply a constant frequency rf knife resonant with the bottom of the magnetic trap, so that atoms which

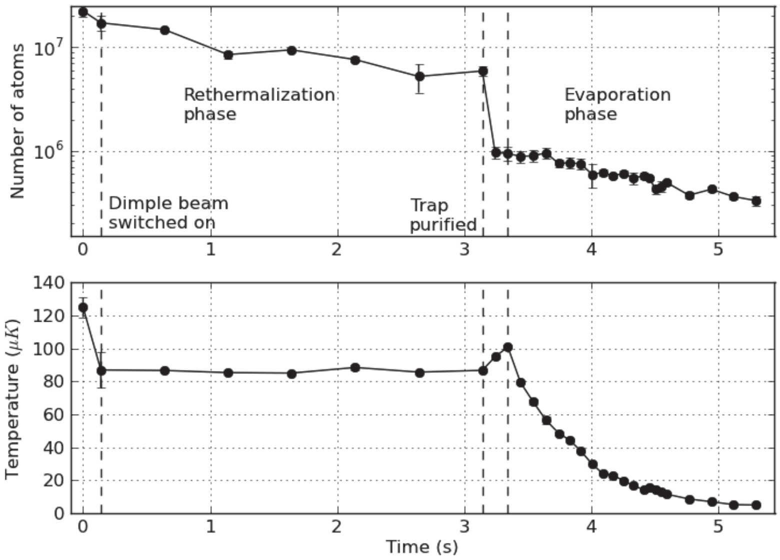

Figure 5.17.: Experimental results showing the evolution of atom number and cloud temperature during the optimised rf and dimple power evaporation ramp. The initial drop in temperature is due to the magnetic trap being decompressed over 0.14 s, where the radial frequency is reduced from 170 Hz to 120 Hz. Following the trap purification, the radial frequency is increased back to 170 Hz over 0.2 s to boost the collision rate, hence the rise in temperature at 3 s.

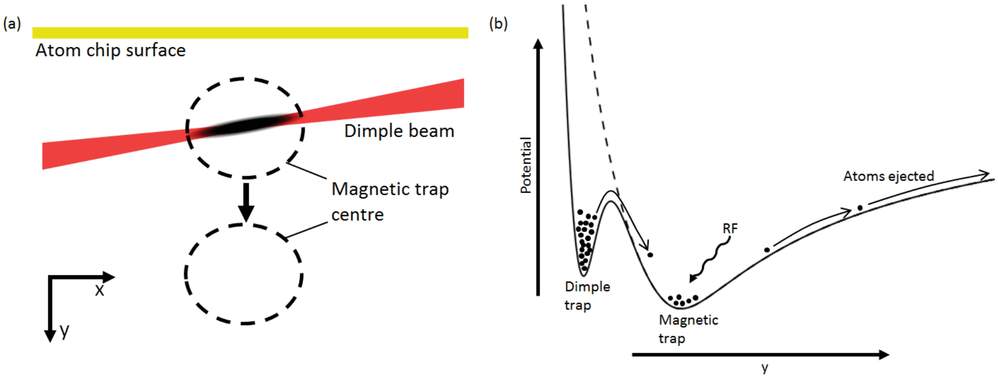

Figure 5.18.: (a) The offset-trap configuration that we use to 'tilt' the dimple trap. (b) The shape of the potential along the y direction once the traps are offset. The shape of the magnetic potential alone is shown with a dashed line. rf radiation resonant with the bottom of the magnetic trap is applied to remove atoms that escape the dimple from the system. Gravity is ignored for this diagram.

escape from the dimple are eventually removed from the system entirely.

The gradient can only be increased so far, as we cannot increase the Z wire current above 80 A due to heating concerns, as discussed in Chapter 3. Further evaporation can be achieved by reducing the dimple power (as always, this has the additional undesirable effect of lowering the collision rate). The dimple power cannot go lower than around 0.5 W with the Z wire at 80 A, as the gradient at that point completely overcomes the trapping potential and all the atoms are lost.

Optimization of the gradient introduction process and subsequent dimple relaxation shows this to be the most efficient of all cooling strategies discussed so far, eventually producing a magnetically trapped cloud of 10^4 atoms at a temperature of only 0.3 μK, corresponding to a phase space density of around 4×10^{-2}. This is higher than was achievable in the purely magnetic trap by a factor of 2000, and represents an overall evaporation efficiency of 1.6. The success of this strategy is presumably due to the evaporation acting out of the side of the dimple. This is still one-dimensional, but the trap frequency in this direction is very high, so that atoms with enough energy to escape will do so very quickly. Experimental results showing the final temperature of the cloud are shown in Figure 5.19.

5.5. A Monte Carlo Simulation of the Hybrid Trap

Loading and cooling the hybrid trap typically involves non-equilibrium processes, so the thermal equilibrium models discussed in sections 5.1.1 and 5.3.1 can miss some important details. Some additional insight into the system's dynamics can be obtained using a Monte Carlo simulation. We have written a Monte Carlo simulation that can simulate general systems of trapped atoms, modelling the atoms as particles moving classically under the influence of the trapping potential, with interactions between the atoms as elastic hard sphere collisions.

The magnetic trap in our experiment can be modelled to good approximation by an infinitely deep 3-dimensional harmonic trap. The optical trap is modelled using the Gaussian beam equations given in Section 5.3.1. The Monte Carlo simulation begins by generating a set of particles in the magnetic trap with a Boltzmann distribution of positions and velocities. To save on computing time and memory we follow the approach of Ma *et al.*[48],

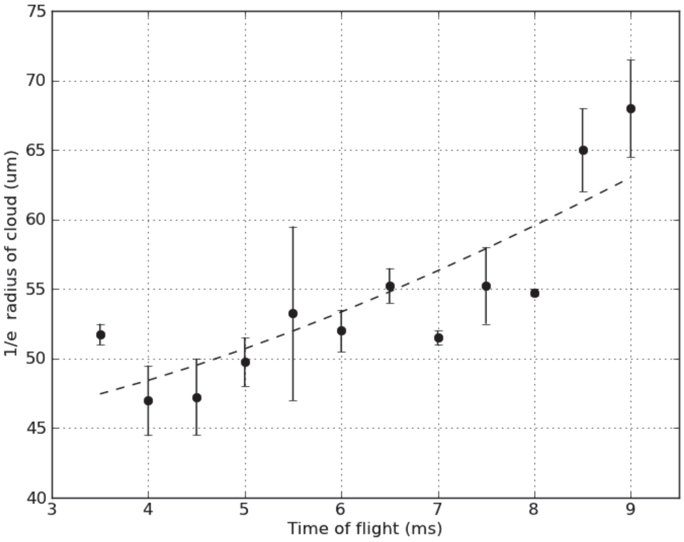

Figure 5.19.: Experimental results showing the final cloud temperature achieved with the trap-tilting method, as measured by time-of-flight expansion. The data are fitted to the curve $\sqrt{\frac{k_\mathrm{B}T}{m}\tau^2+\sigma_0}$ (dashed) where T is the temperature, τ is the time of flight and σ_0 is the size of cloud prior to expansion. The fit suggests T = 0.28 μK and σ_0 = 44 μm. rf spectroscopy measurements of the temperature give the same result.

where groups of N atoms are represented by around 4000 ‘macro-atoms’ with scattering cross sections N times greater than the single atom elastic scattering cross section σ_{el}. The program then iterates over the following steps until the set end time has been reached.

1. A cuboidal volume around the trap is defined and divided into around 10^7 3-dimensional cells of equal volume. To avoid the computationally intensive task of comparing every particle’s position with the position of every other, we consider collisions only between particles that occupy the same cell. As the cloud shrinks and (typically) becomes increasingly dense throughout the evaporation process, the number of cells is held constant while the total size of the cuboid is reduced according to

   $$\begin{aligned}\text{Cuboid extent in dimension } i &= 10 \times 1/\text{e radius of cloud in dimension } i\\ &= 10\sqrt{\frac{k_{\text{B}}T}{m}\frac{1}{\omega_{\text{i}}}}\end{aligned}$$

   where k_{B} is the Boltzmann constant, T is the temperature of the cloud (inferred here from the average velocity of the particles), m is the atomic mass and ω_{i} is the angular trap frequency in dimension i.

2. Once the particles have been grouped into cells, collision probabilities are determined for each cell that contains more than one particle. If each particle represents N atoms, the probability of a collision occurring in a cell of volume V containing N_{p} particles in a time dt is given by

   $$\text{Probability of collision} = NN_{\text{p}}\bar{\sigma}_{\text{el}}\bar{v}_{\text{rel}}\frac{dt}{V}. \tag{5.28}$$

   where $\bar{v}_{\text{rel}}$ is the average relative velocity of atoms in the cell, given by $\sqrt{\frac{6k_{\text{B}}T}{m}}$ and $\bar{\sigma}_{\text{el}}$ is the average scattering cross section for the atoms in the cell, given by

   $$\bar{\sigma}_{\text{el}} = \frac{8\pi a_{\text{Rb}}^2}{1+\bar{k}_{\text{dB}}^2 a_{\text{Rb}}^2}. \tag{5.29}$$

   where a_{Rb} is the s-wave scattering length for rubidium-87 (around 5.6 nm). $\bar{k}_{\text{dB}}$ is the average relative de Broglie wavelength for the cell, given by

   $$\bar{k}_{\text{dB}} = \frac{m\bar{v}_{\text{rel,COM}}}{\hbar}, \tag{5.30}$$

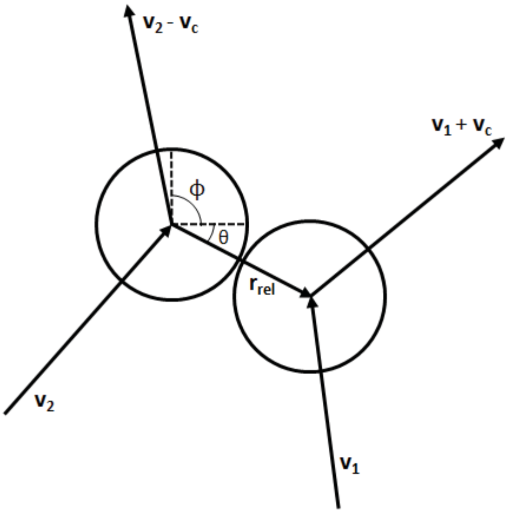

Figure 5.20.: The hard spheres collision model. The angles ϕ and θ are randomly selected from a uniform distribution and define the point on the sphere where the particles collide. The collision imparts a velocity of $+\mathbf{v}_\mathrm{c}$ to one particle and $-\mathbf{v}_\mathrm{c}$ to the other.

where $\bar{v}_{\mathrm{rel,COM}}$ is the average velocity of the atoms in the cell relative to their centre of mass. We only model one collision per cell per time step, so the size of the cells is chosen to ensure that the probability of two collisions occurring is low.

3. The cells in which collisions occur are selected according to the probabilities calculated in step 2. In each collision cell two random particles are chosen to collide. This simulation models collisions as hard sphere collisions with randomly selected impact parameters, as shown in Figure 5.20.

   If the velocities of the particles before the collision are $\mathbf{v}_1$ and $\mathbf{v}_2$, conservation of momentum requires that the final velocities are $\mathbf{v}_1 + k\hat{\mathbf{r}}_{\mathrm{rel}}$ and $\mathbf{v}_2 - k\hat{\mathbf{r}}_{\mathrm{rel}}$ where k is a constant and $\hat{\mathbf{r}}_{\mathrm{rel}} = \frac{\mathbf{r}_2-\mathbf{r}_1}{\sqrt{\mathbf{r}_1^2+\mathbf{r}_2^2-2\mathbf{r}_1\cdot\mathbf{r}_2}}$. Following conservation of energy:

$$\frac{1}{2}m\mathbf{v}_1^2 + \frac{1}{2}m\mathbf{v}_2^2 = \frac{1}{2}m(\mathbf{v}_1 + k\hat{\mathbf{r}}_{\mathrm{rel}})^2 + \frac{1}{2}m(\mathbf{v}_2 - k\hat{\mathbf{r}}_{\mathrm{rel}})^2 \tag{5.31}$$

$$\mathbf{v}_1^2 + \mathbf{v}_2^2 = \mathbf{v}_1^2 + 2k\mathbf{v}_1 \cdot \hat{\mathbf{r}}_{\mathrm{rel}} + k^2 + \mathbf{v}_2^2 - 2k\mathbf{v}_2 \cdot \hat{\mathbf{r}}_{\mathrm{rel}} + k^2 \tag{5.32}$$

$$k = \mathbf{v}_{\mathrm{rel}} \cdot \hat{\mathbf{r}}_{\mathrm{rel}}. \tag{5.33}$$

Therefore, the final velocities after the collision are given by

$$\mathbf{v}_1 \to \mathbf{v}_1 + (\mathbf{v}_{\mathrm{rel}} \cdot \hat{\mathbf{r}}_{\mathrm{rel}})\hat{\mathbf{r}}_{\mathrm{rel}} \tag{5.34}$$

$$\mathbf{v}_2 \to \mathbf{v}_2 - (\mathbf{v}_{\mathrm{rel}} \cdot \hat{\mathbf{r}}_{\mathrm{rel}})\hat{\mathbf{r}}_{\mathrm{rel}}. \tag{5.35}$$

The point of impact is defined with two angular spherical coordinates, θ and ϕ, such that

$$\hat{\mathbf{r}}_{\mathrm{rel}} = \sin(\theta)\cos(\phi)\hat{\mathbf{e}}_{\mathrm{x}} + \sin(\theta)\sin(\phi)\hat{\mathbf{e}}_{\mathrm{y}} + \cos(\theta)\hat{\mathbf{e}}_{\mathrm{z}} \tag{5.36}$$

and to ensure a randomised impact parameter θ and ϕ are set to values between 0 and π, randomly selected from a uniform distribution.

4. Once the velocity changes due to collisions have been calculated, the Python package `scipy.integrate.odeint`[15] is used to integrate the differential equations governing the particles' motion due to the magnetic and optical forces. This integration does not include collisions between particles, and to mitigate the loss of accuracy caused by this omission the time integrated over is set to $0.001\tau_{\mathrm{el}}$, where τ_{el} is the elastic collision lifetime of the atom cloud. This can be obtained directly from the simulation as it progresses, or if that is not an option it can be estimated by assuming the atom cloud has a Maxwell-Boltzmann distribution in a harmonic trap, in which case it is given by

$$\tau_{\mathrm{el}} = \frac{1}{\gamma_{\mathrm{el}}} = \frac{1}{n_{\mathrm{avg}}\bar{v}_{\mathrm{rel}}\bar{\sigma}_{\mathrm{el}}} = \frac{k_B}{\sqrt{6}m\pi^{3/2}f_{\mathrm{r}}^2 f_{\mathrm{z}}\bar{\sigma}_{\mathrm{el}}}\frac{T}{NN_{\mathrm{p}}}, \tag{5.37}$$

   where n_{avg} is the average density of the atom cloud and $f_{\mathrm{r}}^2 f_{\mathrm{z}}$ is the product of the frequencies of the trap in each dimension.

5. The next step simulates rf-driven evaporation. Particles with magnetic potential energies above a given cutoff energy are removed from the population. We can vary this cutoff energy with time to simulate an evaporative cooling ramp. As this removes particles from the simulation, precision is maintained by 'splitting' the particles in two

---

[15] `odeint` solves a system of ordinary differential equations using LSODA from the FORTRAN library odepack.

every time their number drops to half the initial number. Both of the particles produced by a split have the same position and velocity as their parent particle, essentially remaining one particle until one of them is separated from the other by a collision. Correspondingly, the number of atoms represented by each particle is halved. If the number of atoms represented by each particle reaches a value less than or equal to 1, the halving process is stopped.

6. The final step of the simulation deals with the possibility of background collisions. As the number of atoms lost during one time step due to such collisions is typically much less than the number of atoms represented by one particle, this step is performed not by removing whole particles but rather by decreasing the number of atoms represented by each particle by a factor of $1 - \exp(-dt/\tau_{\text{loss}})$, where dt is the duration of the time step and τ_{loss} is the trap lifetime.

5.5.1. Simulation results

Using the simple example of atoms confined in a harmonic trap with no dimple, we optimised the size of the cells and the integration time to ensure simulation behaviour matched the expected collision rate of the cloud. Following this optimization, the simulation reflects experimental results very well. Figure 5.21 compares simulation results with experimental results for the rf evaporation detailed in Section 5.4.3. The simulation allows us to infer the behaviour of quantities that are difficult or impossible to directly measure in experiments, such as the phase space density, collision rate, γ and so on.

As stated in Section 5.2.2, there were concerns that small waist sizes of the dimple beam would inhibit loading of the dimple, as in order to be loaded an atom must undergo a collision while in the light beam, which is increasingly unlikely the smaller the waist. However, the probability of such a collision successfully loading the atom is proportional to the dimple depth, which is itself proportional to the (beam waist)$^{-2}$. This suggests there is an optimal beam waist. The thermal equilibrium model only takes into account the trap depth and neglects loading dynamics, so it suggests that the smaller the beam waist, the more atoms will be rethermalize into it. Results from the Monte Carlo simulation are shown in Figure 5.22, and

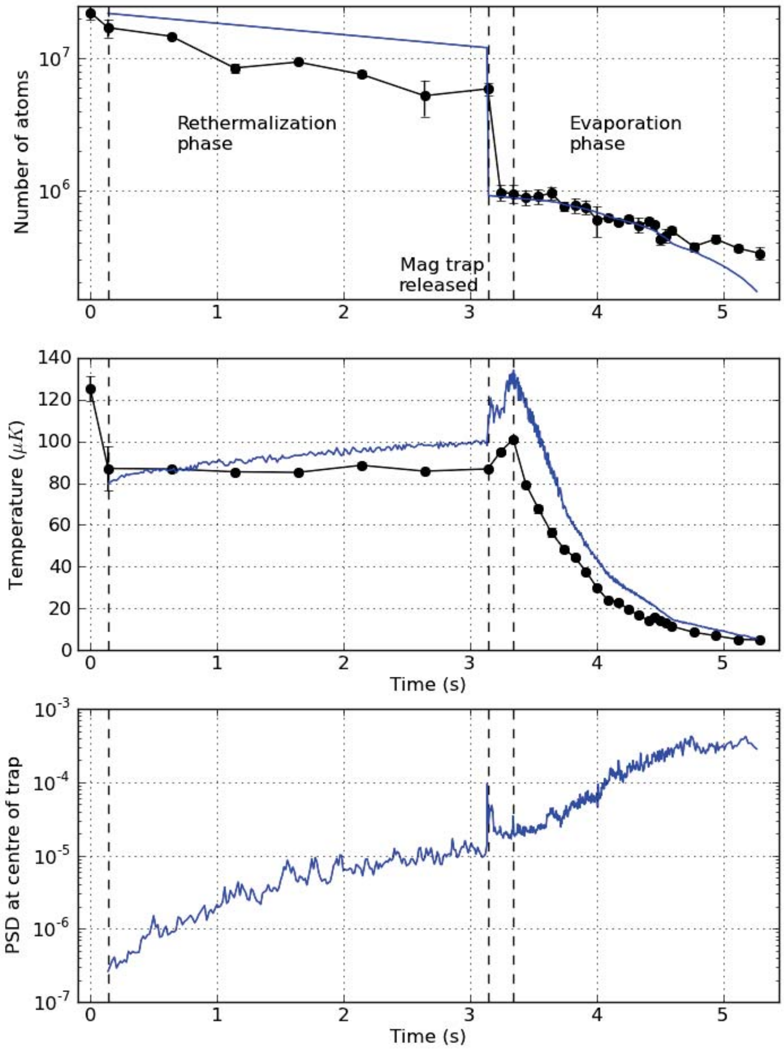

Figure 5.21.: Comparison of simulation (blue) and experimental results (black), using the ramp found in Section 5.4.3. The evolution of the peak phase space density in the simulation is also shown.

give the full picture. Dimple beams with large waists reach their maximum population quickly, but this maximum population is not very large. Beams with small waists take longer to load, but appear to have higher maximum populations (in the absence of background loss). The optimal beam waist where these effects balance (given a trap lifetime of 5 s) is around 30 μm, which fortunately coincides with the smallest beam waist achievable on our experiment.

The evaporation strategy discussed in 5.4.2 uses ramps in dimple power and trap purifications to gain successive increases in phase-space density. The phase-space density and γ are crucial quantities in this strategy, but are not directly measurable. The simulation can demonstrate how these quantities evolve. Although γ is defined at thermal equilibrium, equation (A.13) can be rewritten to give $\gamma = \frac{3}{2}\frac{U}{K}$, where $\frac{U}{K}$ is the ratio of potential energy to kinetic energy of the cloud. This quantity is defined off-equilibrium and can be easily obtained from the simulation. Figure 5.23 shows how effective the strategy could be in an idealised lossless environment, where we can ensure the trap changes are isentropic.

Equation (5.2) cannot be solved analytically to give the density of states $\rho(\epsilon)$ for a hybrid trap, but we can use the simulation to see how the energy distribution $P(\epsilon)$ changes as the dimple loads. The purely harmonic trap distribution shown in Figure 5.1a changes to a bimodal distribution, shown in Figure 5.24, reflecting the proportion of atoms in the purely magnetic regions of the trap and those trapped in the dimple.

5.6. Summary

The addition of the dimple beam has hugely improved our evaporative cooling efficiency. Using rf-driven evaporative cooling in the purely magnetic trap, we could only achieve an efficiency of 0.4. With the dimple, we can achieve efficiencies up to 1.6. Using the trap-tilting method described in Section 5.4.4, we have a cloud of 10^4 atoms at a temperature of 0.3 μK in a 170 Hz purely magnetic trap. In the introduction to this chapter, we stated that we need the cloud in the trench to have a temperature of around 1 μK in a 1 kHz trap if it is to fit inside the trench. If the 0.3 μK cloud in the 170 Hz trap can be compressed adiabatically to a 1 kHz trap, we would expect its temperature to rise to 1.0 μK (using the adiabatic compression

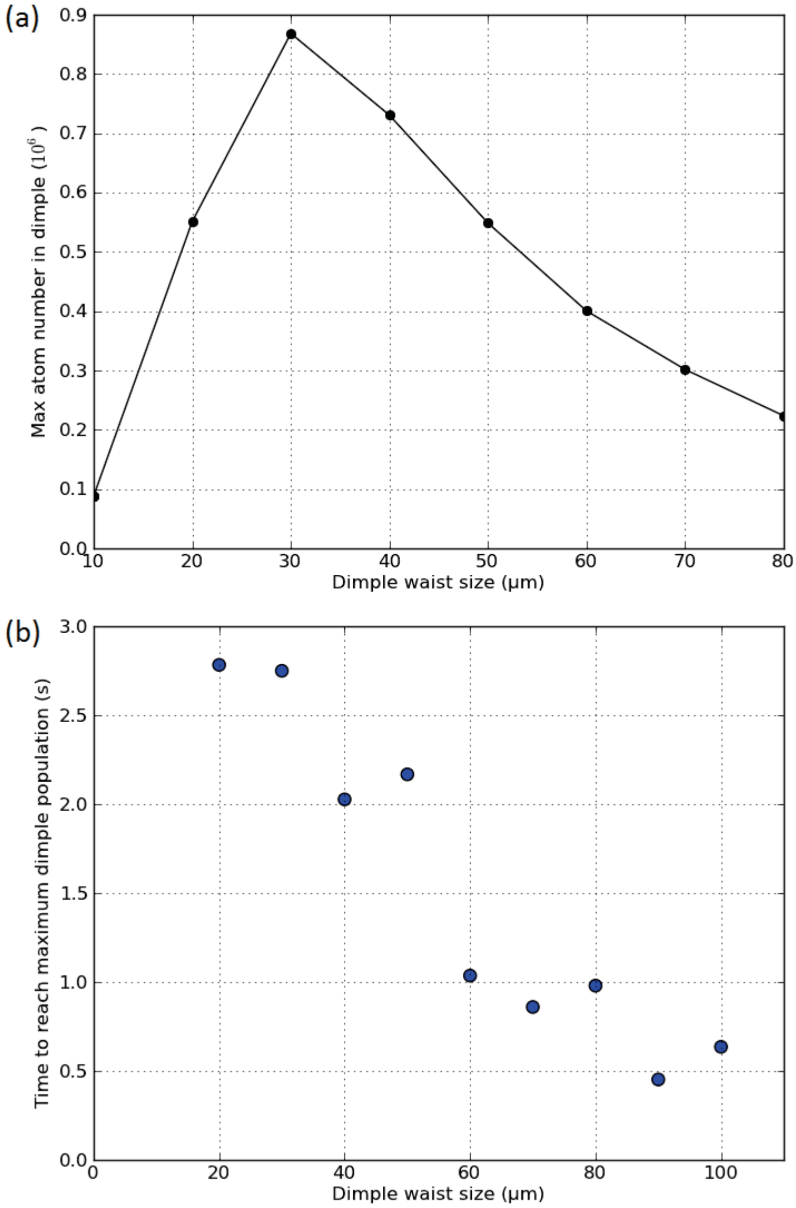

Figure 5.22.: (a) Results from the Monte Carlo simulation showing the maximum number of atoms that can be loaded into the dimple by rethermalization for a variety of dimple waists. The beam power was kept constant at 8 W, and the magnetic trap had 2×10^7 atoms at 100 μK, with a radial frequency of 120 Hz and an axial frequency of 30 Hz. (b) Different beam waists showed the maximum dimple population occurring at different times — larger waists reached the maximum population earlier than smaller waists.

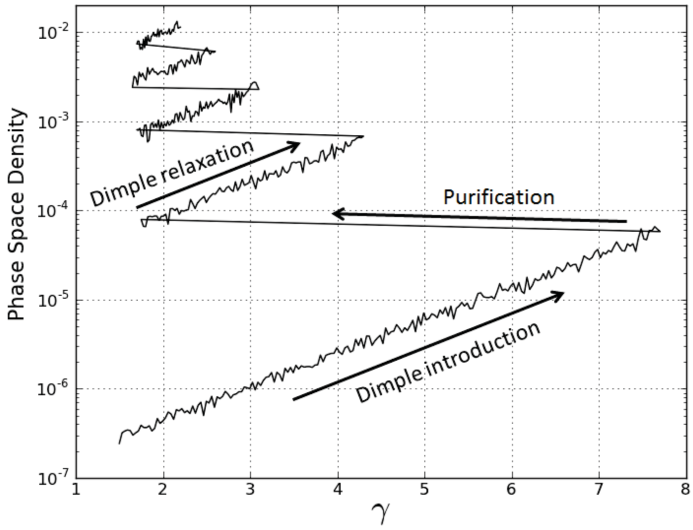

Figure 5.23.: Simulation results showing the evolution of γ and the phase-space density of the atom cloud in the hybrid trap during a procedure of initial dimple loading followed by beam power decrease and repeated purifications. The phase-space density clearly increases as $\exp(\gamma)$, and the maximum achievable γ decreases as the cloud cools. Background gas collisions have been disabled in this simulation.

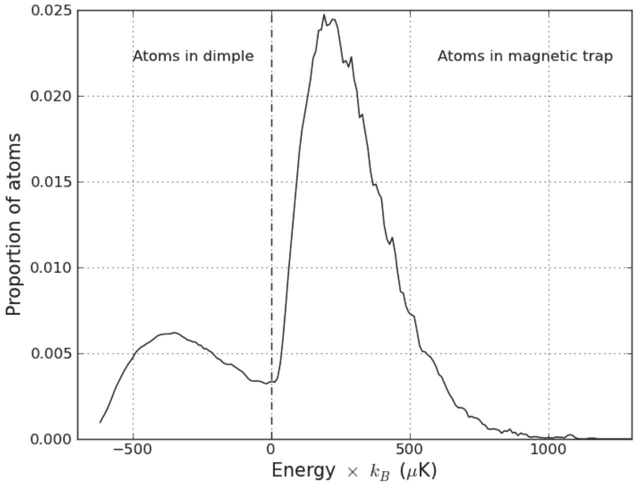

Figure 5.24.: The energy distribution of the atom cloud held in a 120 Hz magnetic trap and loaded 8 W dimple, once the traps have been overlapped for 3 s. The temperature of the atom cloud is about 100 K at this point.

equations given in Section 5.1.2), which is ideal.

6. Experiments with a Cold Cloud in the Trench

After using the trap-tilting evaporation strategy detailed in Section 5.4.4, we end up with a cloud at 0.3 μK with 10^4 atoms in the 170 Hz magnetic trap, 1 mm below the chip. This chapter details our efforts to adiabatically transport the cloud to the chip, the expected behaviour of the cloud in the trench, measurements of the cloud in the trench using the waveguides, and the potential use of the waveguides to exert optical-dipole forces on atoms in the trench.

6.1. Moving the cloud towards the trench

6.1.1. Required currents

An absorption image of the cloud in the 170 × 170 × 30 Hz trap after it has been cooled with the trap-tilting strategy is shown in Figure 6.1. The cloud is around 1 mm from the trench in the y direction. As mentioned in Chapter 4, the trench is not directly below the Z-wire, it is offset in x by about 210 μm and in z by about 200 μm. This offset was not an issue when using the non-cooled cloud, as the cloud's size in x and z meant that the trap centre did not need to be perfectly aligned with the trench to get atoms inside. The colder cloud is much smaller, however, and using the same sequence of current ramps means a very small number of the atoms will enter the trench. Aligning the cloud with the trench requires a much larger bias field in the y direction to move the cloud in x, and a field gradient in z to move the cloud in z.

Producing a larger y bias field required a new current controller and power supply. The gradient required in z is too large to produce by adding

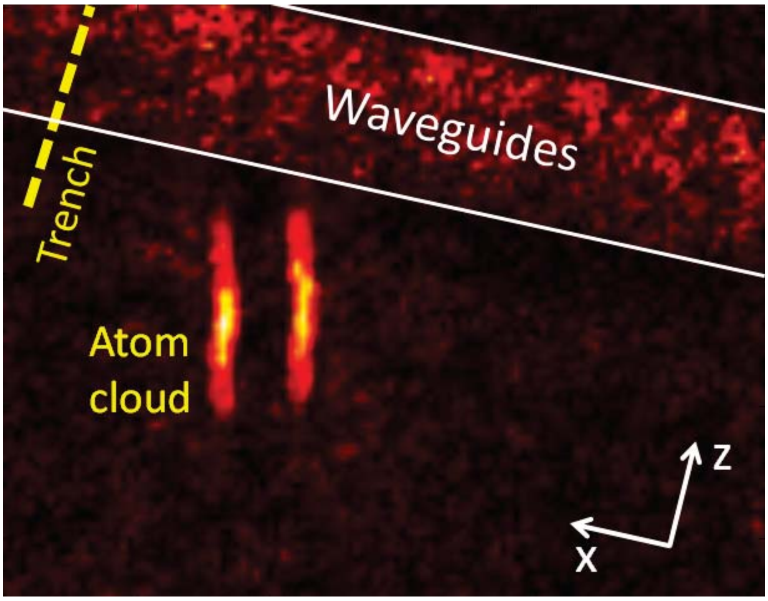

Figure 6.1.: Absorption image taken using the 45° imaging system showing the cloud (and its reflection, on the right) after it has been cooled and moved close to the chip, using the same current ramps as used to generate absorption signals in Chapter 4, adjusted slightly to keep the cloud slightly below the chip surface so it remains visible. The positions of the waveguide array and the trench are shown. The cloud is significantly offset from the trench in x and z. The image shows a 460 μm × 380 μm area.

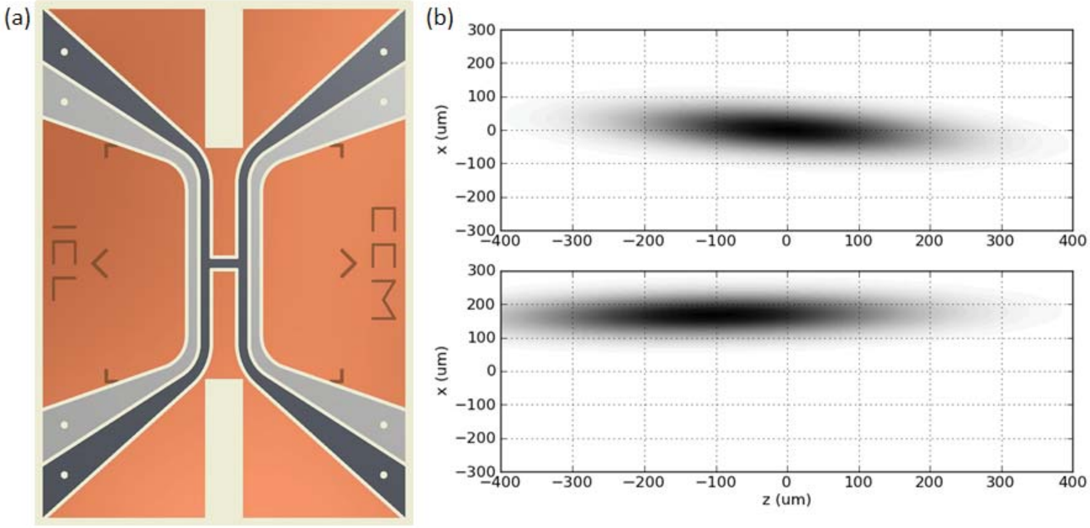

Figure 6.2.: (a) Diagram of our subchip structure showing the location of the end wires (grey) relative to the Z wire (dark grey). (b) Results from our magnetic field simulation showing the expected number distribution of a 10 μK magnetically trapped cloud in the $x - z$ plane with current only in the Z wire and bias wires (top), and including differing currents of 35 A and 65 A in the end wires (bottom). With the end wires active the trap centre is shifted in the x and z directions, the trap axis rotates around the y axis, and the axial trapping frequency is reduced.

a pair of anti-Helmholtz coils to the experiment, but can be produced by sending different currents through the end wires in the subchip; two wires on either side of the Z-wire that are perpendicular to the central Z strut, as shown in Figure 6.2a.

Running currents in the end wires also rotates the trap around the y axis, and reduces the trap bottom and axial trapping frequency. These quantities are dependent on the mean current through the wires, while the translation of the trap centre in z is dependent on the difference in current.

As in Chapter 4 we move the cloud close to the trench in y by increasing the bias wire current to 80 A and decreasing the Z wire current to 40 A. This leaves the trap centre about 10 μm below the chip surface. Then, by comparing absorption images of the compressed cloud with the position of the trench we find end wire currents of 35 A and 65 A move the trap in z to just below the trench, with a y bias field of 1.9 A to achieve the necessary movement in x. According to our model of the magnetic fields, at these currents the axial frequency of the trap has decreased to 15 Hz and the trap axis has rotated by around 0.1 rad, which we believe makes it parallel to the trench (the initial trap is not parallel, due to the magnetic field contributions from the arms of the Z wire). The exact rotation and position of the trap relative to the trench cannot be determined from the 45° imaging, as the shape of the trench is not resolvable. According to the model, the transverse trap frequency at these currents is about 700 Hz.

6.1.2. Moving the Cloud with minimal Heating

Cooling the magnetically trapped cloud to 0.3 μK and ramping the initial magnetic trap currents to these values over 0.5 s results in a cloud near the trench at a temperature of 65 μK, as measured using RF spectroscopy, indicating that some aspect of the ramp has heated the cloud substantially. RF measurements of temperature[1] were used here because the low optical densities and close proximity to the chip prevented accurate time-of-flight measurements. Since we were imaging the cloud while it was held in the trap, the inhomogeneous Zeeman shift makes determining the total atom number difficult. We therefore find the temperature by fitting equation (5.10) to the central optical density of the cloud as measured *in situ* — a quantity that is proportional to the total atom number.

Following some investigation we observed the temperature of the cloud rising rapidly as the transverse trap frequency reached 200 Hz, suggesting current noise at this frequency in one of the current controllers or power supplies. Keeping the trap at 200 Hz and imaging it after various hold times showed rapid expansion in the y direction (and eventually complete loss as atoms are thrown out of the trap), suggesting that the field with the noise is oriented in the x direction, narrowing possibilities down to the bias wire supply, the Z wire supply, or the x bias supply. The x bias turned out to be the culprit; a small x bias field was held on throughout the ramp, and switching this off beforehand removed the current noise and therefore removed the parametric heating.

With the parametric heating fixed, we again measured the energy distribution of the compressed cloud by performing RF spectroscopy, applying the radiation for 1 s. However, this time we obtained results that deviated from the expected shape (given by equation (5.10)). These results are

---

[1] As described in Section 5.1.2.

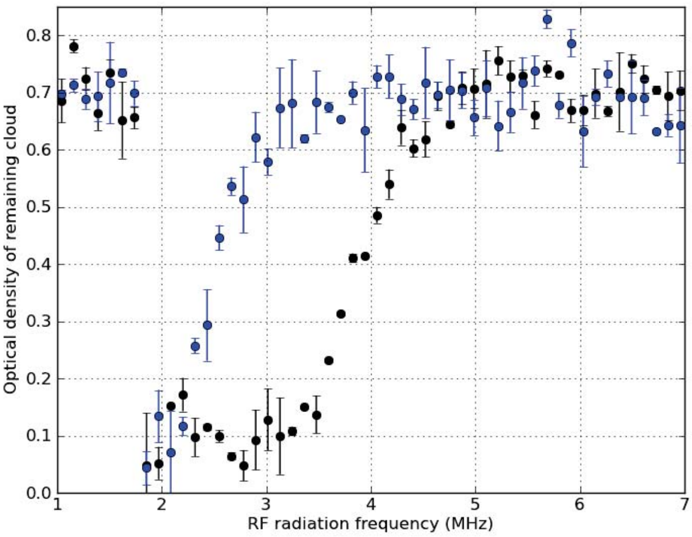

Figure 6.3.: Results of an RF spectroscopy measurement of the cooled cloud after it has been compressed and moved close to the chip by ramping the bias, Z and end wire currents (black). The results deviate from the expression given by equation (5.10); here, all the atoms are ejected from the trap over a range of radiation frequencies. This suggests that the cloud is not at thermal equilibrium, and atoms with a range of initial energies are reaching the magnetic potential where spin flips are induced. This behaviour was found to be caused by the compression ramps setting off a centre-of-mass oscillation in the trap. After this problem was fixed, the measurement was repeated and the results followed the expected shape (blue).

shown in Figure 6.3. Unlike previous measurements, here the entire atom cloud is lost over a range of frequencies from 1.8 MHz to around 3.0 MHz, instead of only at the frequency corresponding to the minimum field in the trap. This behaviour has two plausible explanations; either the cloud is being continuously heated, or is undergoing centre-of-mass oscillations in the trap.

We can use some simple considerations to explain why heating or oscillations would have this effect on the spectroscopy signal. Firstly, if the cloud is being continuously heated at a rate γ_{t} and the rf radiation is applied for a time t, atoms with energy E will be heated to $E + k_{\mathrm{B}}\gamma_{\mathrm{t}}t$ during the measurement, and if this brings them above a magnetic potential of hf_{RF} they will be lost from the trap. We would therefore expect there to be no atoms remaining for all frequencies

$$f_{\mathrm{TB}} \leq f_{\mathrm{RF}} \leq f_{\mathrm{TB}} + \frac{k_{\mathrm{B}}}{h}\gamma_{\mathrm{t}} t. \tag{6.1}$$

The experimental results show that total atom loss occurs over a frequency range of 1.2 MHz when the radiation is applied for 1 s, which suggests that $\gamma_{\mathrm{t}} = 57\ \mu\mathrm{K/s}$.

In any case, the time dependence in equation (6.1) allows us to make a direct test, since applying the RF radiation for longer durations should increase the cloud loss frequency range if the cloud is being continuously heated. Measurement showed that the frequency range did not change with duration, implying that the cloud is not being continuously heated.

If the cloud is undergoing centre-of-mass oscillations of amplitude A then, on average, atoms with energy E relative to the cloud's centre of mass will have an energy $E + \frac{1}{2}m\left(\omega A\right)^2$ relative to the trap centre, where ω is the angular frequency of the trap. The atom can therefore explore higher potentials than if there were no oscillation, being lost from the trap if it reaches a magnetic potential of hf_{RF}. We would therefore expect most of the cloud to be lost when the radiation frequency

$$f_{\mathrm{TB}} \leq f_{\mathrm{RF}} \leq f_{\mathrm{TB}} + \frac{1}{2h}m\left(\omega A\right)^2. \tag{6.2}$$

The 1.2 MHz frequency range obsered in experiment suggests that $A \approx 14\ \mu\mathrm{m}$.

Observing the oscillation with absorption imaging was difficult given the cloud's proximity to the chip and low atom number. Some image sequences appeared to show signs of oscillation in the x axis, but the signals have too much noise to draw a definitive conclusion. Nonetheless, if the cloud is oscillating in the compressed trap it is presumably receiving a kick at some point in the ramp that sets off the oscillation.

Measuring the current ramps used for the y bias field and in each end wire showed no sudden changes except for a small jump in the ramp used in one of the end wires — correcting this did not remove the oscillation. The problem was finally fixed by changing the shape of our ramps from linear to a curved shape (defined by the *tanh* function); this smooths out the time differential of the ramp, which appears to remove the oscillation, as the RF spectroscopy signal obtained from the compressed cloud now fits the model.

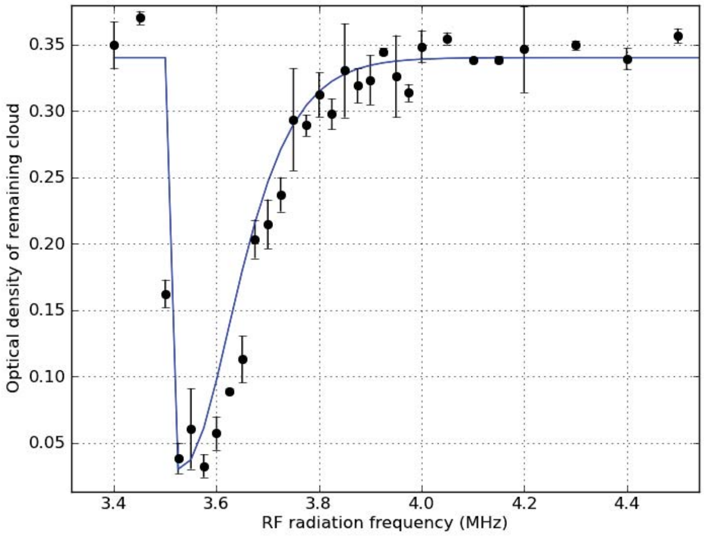

Figure 6.4.: Results from RF spectroscopy of the compressed cloud just below the trench once the sources of heating during the compression ramp were removed. The data are fitted to equation (5.10), suggesting a temperature of about 2 μK.

This signal is shown in Figure 6.4. The shape of the signal suggests the cloud's temperature is now about 2 μK, which in a 700 $\times$ 700 $\times$ 15 Hz trap with 10^4 atoms remaining suggests a phase space density of about 10^{-3}. This is lower than the uncompressed cloud by a factor of about 40, showing that the compression is clearly still not adiabatic. However, the low temperature means the $1/e$ radius of the cloud should now be around 3.1 μm, small enough to fit in the trench without significant loss.

6.2. Trench absorption signals from the cold cloud

The final movement of the cloud into the trench was performed by ramping down the Z wire current by 2 A over 2 ms, which moves the trap centre by about 30 μm. We again measure absorption by sending light through the waveguides that we expect to be resonant with atoms in the centre of the magnetic trap. When the cooled cloud enters the trench, we measure absorption of around 50%, 5 times larger than was achieved using the non-cooled cloud. The drop in transmission is shown in Figure 6.5a. Us-

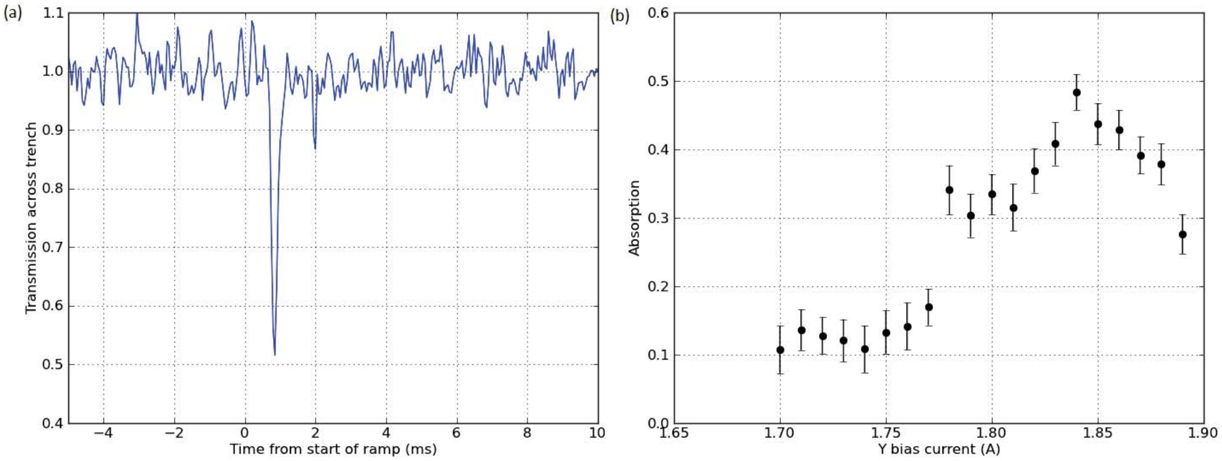

Figure 6.5.: (a) Signal of in-trench absorption observed on the APD as the cooled cloud was moved into the trench. The signal lasts for about 600 μs and has a magnitude of around 50%, suggesting the cloud has a number density of 0.15 /μm^3 in the beam mode. The graph shows the averaged results from 3 experimental runs. (b) The variation in the depth of the dip as the y bias field is changed prior to trench entry, moving the cloud in x. No averaging was performed for these measurements.

ing the simple model described in Chapter 4 that assumes a homogeneous atom number density n inside the trench, the 50% absorption implies $n = 1.5\times10^{17}/\text{m}^3$, close to the expected peak density of the cloud, $4\times10^{17}/\text{m}^3$. The number of atoms in the mode is then $\pi w_0^2 w_\text{t} n = 36$. Despite the $1/e$ diameter of the cloud being similar to the spot size of the beam, taking the spatial variation of the number density into account in these calculations does not significantly change the results[2].

Figure 6.5b shows the variation of the absorption as the y bias field is changed (altering the cloud's position in x) prior to entry. We know from experiment that changing the y bias current by 0.1 A moves the cloud in x by around 12 μm, which explains why the absorption is only visible in a range of about 0.15 A. The size of the absorption signal is now large enough that it can be observed in the results of a single experimental run, unlike the signals from the MOT and magnetic traps, which required at least 10 averages to be clearly visible against the noise.

---

[2] If the cloud had a diameter less than about 1 μm, we would expect the absorption to drop, despite the high density, as more of the beam would miss the cloud completely as it crosses the trench.

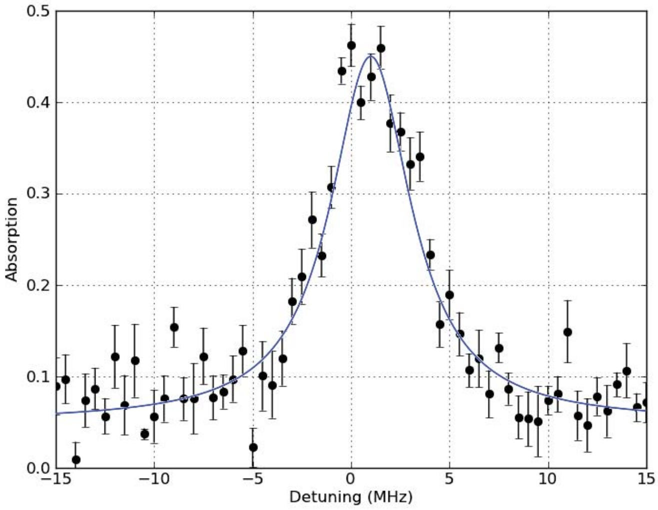

Figure 6.6.: The variation of the in-trench absorption with detection light detuning, for the 2 μK cloud. A lorentzian curve has been fit to the data (blue). The linewidth of the transition is the same as it is outside the trench, as expected.

Figure 6.6 shows the in-trench absorption spectrum of the cold cloud. Polarization-dependent effects such as those described in Section 4.3.1 are not visible in this case, as the magnetic fields present during entry are much smaller, around 1.7 G (in Section 4.3.1 the field was 14 G).

6.3. Attempts to hold the cloud in the trench

With a temperature of 2 μK the cloud has a $1/e$ radius of 3.1 μm and a $1/e$ length of around 150 μm. Simulation results showing the evolution of atom number with duration once the cloud is inside the trench are shown in Figure 6.7. Assuming the cloud is positioned in the exact centre of the trench, we expect around 70% of the atoms to have energies low enough to avoid hitting the walls.

We therefore expect to be able to move the cloud slowly into the trench and hold it there without significant loss, measuring continuous absorption in the trench until the cloud is completely destroyed by photon scattering. However, attempts so far have not shown any signals that last longer than 0.6 ms. Figure 6.8 shows how the absorption signal decays with time after

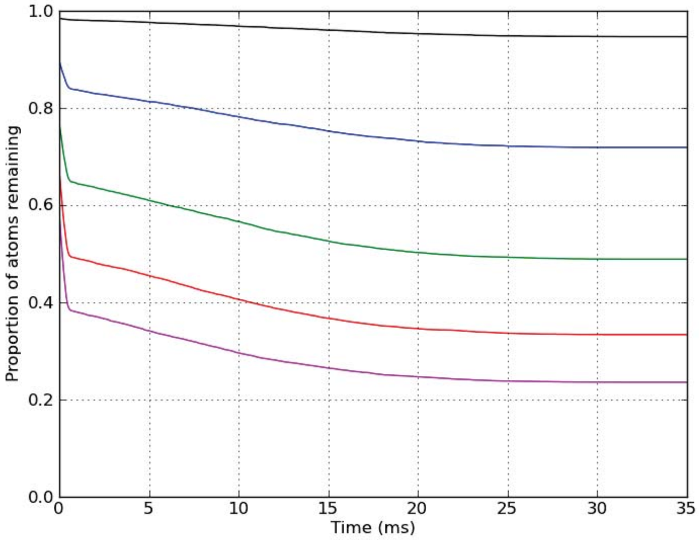

Figure 6.7.: Simulation results showing the evolution of total atom number in the trench over time for cloud temperatures of 1 μK (black), 2 μK (blue), 3 μK (green), 4 μK (red) and 5 μK (magenta). These results were obtained from the Monte Carlo simulation detailed in Chapter 5, modified to include the shape of the trench and so that particles that move into the trench walls are removed from the system. The simulation was started with the cloud already inside the trench, so atoms in the outer regions of the cloud are instantly lost, followed by further loss over a time scale the order of the trap's transverse oscillation period, and then more gradually over the trap's axial oscillation period. The clouds with initial temperatures higher than 2 μK were cooled by the loss, all eventually reaching 2.5 μK.

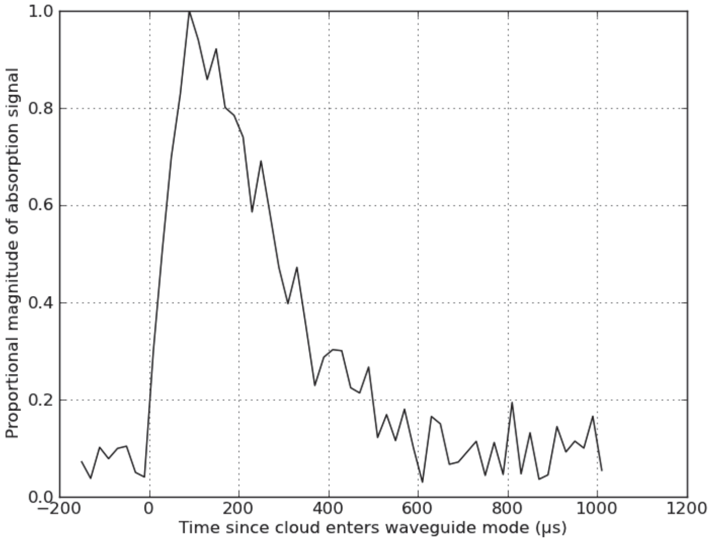

Figure 6.8.: Looking at the variation of absorption as the cold cloud enters the trench. The absorption is shown as a proportion of its maximum value, about 50%. The movement of the trap is the same as was used for the measurement in Figure 6.5a but was measured on the APD using smaller 10 μs time bins. As each time bin now contains fewer photon counts the signal-to-noise ratio is lower — the graph shows the averaged results of 15 experimental runs.

the cloud enters the trench. This graph was taken using the same current ramps as were used to obtain the results of Figure 6.5a, but with the photon counts on the APD grouped into smaller time bins (10 μs instead of 50 μs) to allow for better time resolution.

This section examines potential reasons why we were not able to hold the cloud in the trench.

6.3.1. Speed of Trench Entry and Adiabatic Movement

The ramp used to generate the absorption signals shown in Figure 6.5 changed the current in the Z wire by 2 A, which we expect to move the trap centre by 30 μm. Given the ramp time of 2 ms, this corresponds to a trap centre movement speed of 15 mm/s. The mean speed of the atoms in a 2 μK cloud is 20 mm/s, implying the kinetic energy introduced to the cloud by the movement of the trap is similar in magnitude to the kinetic energy of the atoms. We therefore expect the ramp to kick off oscillations in the y

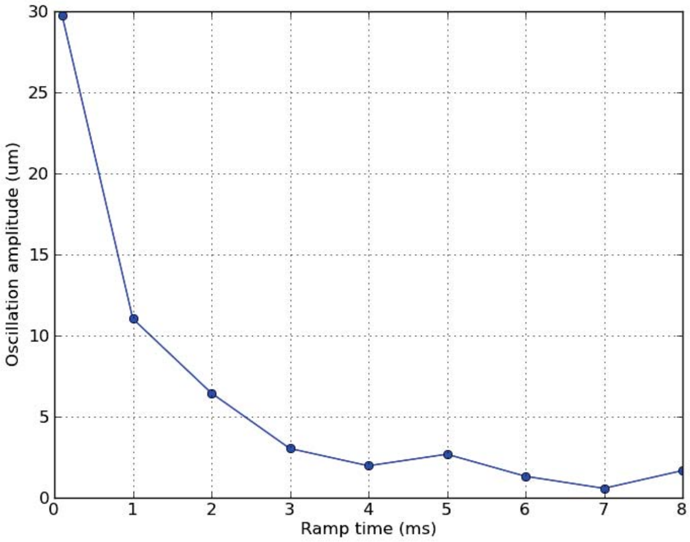

Figure 6.9.: Simulation results showing the amplitude of the oscillations of the centre of mass of a 2 μK cloud held in a 700 × 700 × 15 Hz trap, after the trap centre has been moved 30 μm over a range of times.

axis, heating the cloud and possibly causing the cloud to hit the top of the trench. Figure 6.9 shows simulation results demonstrating how the centre of mass of a 2 μK cloud oscillates in y after it has been moved 30 μm using a range of movement speeds.

If we want to hold the cloud in the trench, we will have to use slower ramps, moving the trap centre into the trench over times the order of 10 ms. However, in practice, using slower ramps only seems to drastically reduce the absorption measured in the trench. Only fast ramps work well, suggesting that some other effect is rapidly removing atoms from the trap before they enter the waveguide mode.

6.3.2. Cloud Position and Orientation

The small x dimensions of both cloud (6 microns wide) and trench (16 microns wide) mean that positioning the cloud correctly in x is crucial if we want to get a large proportion of the atoms inside as the cloud is moved upwards into the trench. If the cloud is being held in the trench, an off-centre x position lowers the magnetic trap potential at the trench wall, meaning a lower proportion of atoms will remain trapped after half an oscillation period — for our 700 Hz trap this is about 0.7 ms, similar to the duration of our measured absorption signal. As shown in Figure 6.5b, we can tune the x position of the cloud by altering the y-bias field, but varying this does not seem to produce longer-lasting absorption signals.

If the cloud is offset from the centre of the trench in z, then atoms will hit one of the ends of the trench after half an axial oscillation period, which is 30 ms assuming the trap frequency is 15 Hz. The loss we observe occurs much faster than this, so it is unlikely that a z offset is the source of the problem. If the cloud is centered in the trench but not parallel in the $x-z$ plane, atoms can be lost at either end of the trap as atoms hit the sides of the trench, so we would expect loss over a quarter of the trap oscillation period, again much slower than the loss rate we observe. Nonetheless, we have performed an extensive scan over the two end wire currents (which control the trap position in z and the angle of the trap axis) to try and increase the cloud's lifetime in the trench, compensating for the end wire effect on the trap's x position using the y-bias field. The magnitude of the absorption varied slightly as the cloud moved in z, but no increases in the cloud's in-trench lifetime were observed.

6.3.3. Cloud size

If the trap frequency is lower than the expected 700 Hz or the cloud temperature is higher than the 2 μK we measure using RF spectroscopy, then atoms can escape on either side of the trap, so we would expect to lose atoms over a quarter of a transverse oscillation — around 0.35 ms.

We can measure the oscillation frequency of the atoms in the magnetic trap using the same technique we used to measure their frequency in the optical trap, as described in Section 5.3.2. For the magnetic trap just outside the trench we induce resonant excitations by oscillating the current in the Z-wire by ±0.2 A. The cloud's maximum optical density in the $x-y$ plane is plotted in Figure 6.10 as a function of the Z-wire current oscillation frequency. If the cloud has been heated, the optical density decreases. The strongest decrease is around 650 Hz, implying that this is the oscillation frequency of the trap. This is slightly lower than the expected frequency of 700 Hz, but not enough to explain the loss we observe.

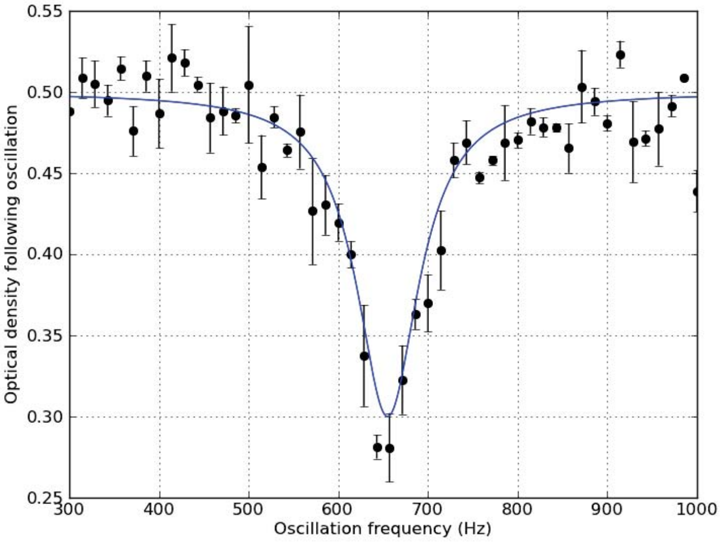

Figure 6.10.: Experimental results showing the optical density of the 2 μK cloud just outside the trench after the position of the trap centre has been oscillated in the y direction. When the oscillation frequency is close to the trap frequency the cloud is heated, causing a drop in its optical density. A lorentzian curve (blue) with a FWHM of 84 Hz is fitted to the data.

6.3.4. Effects of Photon Scattering

There is a possibility that the resonant light used to obtain the absorption signals is destroying the atom sample, as the atoms spontaneously emitting photons receive a momentum kick, which may heat them enough to eject them from the trap or cause them to collide with the walls of the trench.

An atom absorbing and re-emitting a photon receives a momentum kick of $\hbar\left(\mathbf{k}_1 + \mathbf{k}_2\right)$ where k_1 and k_2 are the wave numbers of the absorbed and re-emitted photons respectively. If the emission is spontaneous $\mathbf{k}_2$ is oriented randomly, so assuming many photons are scattered we can ignore its contribution and consider only the contribution from the absorbed photon.

For 780 nm light $\hbar|\mathbf{k}| \approx 1.6$ eV/c. In our trench the light propagates in the $+X$ direction, so we can approximate the effect of continuous photon scattering with a constant acceleration $\gamma_{\mathrm{s}}\hbar|\mathbf{k}|/m$, where γ_{s} is the scattering rate, which on resonance is $\frac{\Gamma}{2}\frac{I}{I_{\mathrm{sat}}}$ where Γ is the transition linewidth.

Considering the simple case of an atom initially at rest in the centre of the trench and in the centre of the beam mode (with the power set so that $I/I_{\mathrm{sat}} = 0.1$), we would expect repeated photon scattering to push it 8 μm into the trench wall in a time

$$t_{\mathrm{wall}} = \sqrt{\frac{2m(8\ \mu\mathrm{m})}{\hbar\gamma_{\mathrm{s}}|\mathbf{k}|}} = 95\ \mu\mathrm{s}. \tag{6.3}$$

The timescale implies 95 μs $\times\ \gamma_{\mathrm{s}} \approx 29$ photons have been scattered, and the final velocity as the atom hits the wall is around 0.17 ms^{-1}. The random nature of the emission adds an uncertainty of ± 10 μs to the timescale.

In practice we have a distribution of atom positions and velocities in the beam mode, which means the absorption signal is not abruptly lost at 95 μs but instead over a period of time. Considering a cloud with an atom distribution in X given by

$$f(x) = A \exp\left[-\frac{(x - x_0)^2}{\sigma_{\mathrm{x}}^2}\right], \tag{6.4}$$

where A is a normalisation constant, x_0 is the centre of the cloud and σ_{x} is the $1/e$ radius of the cloud in X, we can determine the distribution of wall

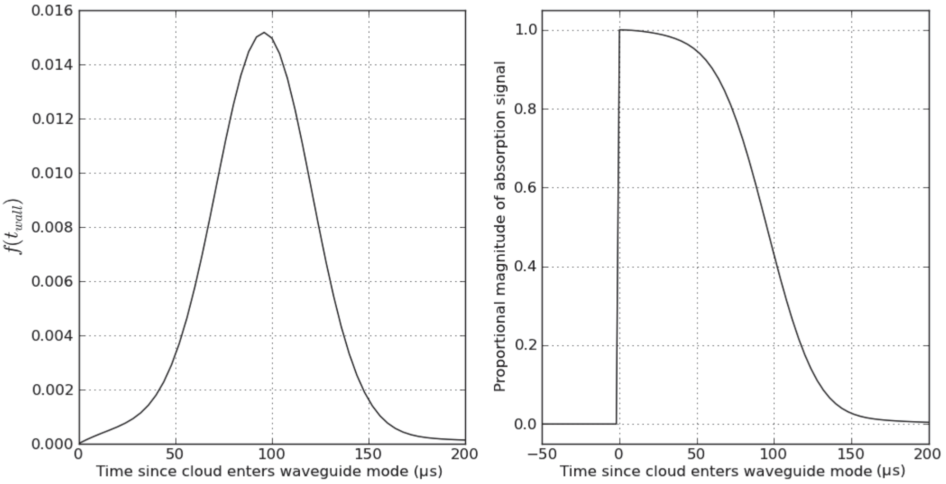

Figure 6.11.: (a) Results from a simple model showing the time taken for atoms in the trench to be lost when illuminated with resonant light from a waveguide at an intensity of $0.1 I_{\mathrm{sat}}$. The distribution of loss times are shown for a cloud of atoms at 2 μK. (b) The time evolution of the absorption signal we would expect if photon scattering is the cause of the loss. The signal is shown as a proportion of its initial value.

collision times;

$$f(t_{\mathrm{wall}}) = B t_{\mathrm{wall}} \exp\left[-\frac{(x_0 - w_{\mathrm{T}} + a t_{\mathrm{wall}}^2)^2}{\sigma_{\mathrm{x}}^2}\right], \tag{6.5}$$

where B is a normalisation constant, w_{T} is the width of the trench and a is the constant acceleration due to photon absorption — the effects of spontaneous emission are ignored here. If we take into account the cloud's velocity distribution in addition to the position distribution, along with the magnetic trap forces and the intensity distribution of the light beam, $f(t_{\mathrm{wall}})$ is no longer analytic but can be found numerically. These results are shown in Figure 6.11. If photon scattering is causing atom loss, the atom number would decrease over time as

$$N_0 \left(1 - \int_0^t f(t_{\mathrm{wall}}) dt\right), \tag{6.6}$$

as shown in Figure 6.11b.

We would therefore expect a drop in the number of atoms in the waveguide mode over this time scale, unless atoms just outside the waveguide mode are refilling it faster than they can be lost. Assuming the waveguide mode is positioned at the centre of the trap, we expect the average atom speed here to be $\sqrt{3k_\mathrm{B}T/m}$, which at 2 μK is 24 mm/s, meaning an atom 2.1 μm outside the waveguide mode can travel to its centre in around 88 μs.

These theoretical considerations suggest that atoms can refill the waveguide mode faster than it can be emptied by photon scattering. In experiment, the loss we observe occurs over 600 μs (as seen in Figure 6.8) rather than around 150 μs (as in Figure 6.11), suggesting that photon scattering is not responsible for the lack of a persistent absorption signal.

We can also test this by incorporating photon scattering into the Monte Carlo simulation described in Section 5.5. Starting with a cold cloud already held in the trench, and measuring the number of atoms in the waveguide mode, there is an initial drop in number when the waveguide light is switched on, but soon the rate at which atoms are driven into the trench wall equalises with the rate at which atoms enter the waveguide mode, leading to a constant number in the mode that is about half the initial number. These results support the idea that photon scattering is not the reason that the absorption signal is being lost.

We can test this behaviour experimentally. Instead of switching the waveguide light on a few milliseconds before the cloud enters the trench and then leaving it on throughout the entry, we can use just one short-pulse of light once the cloud has already entered. If this pulse is significantly shorter than the 100 μs loss time, the effect of photon scattering on the atom number in the mode will be negligible. By performing a series of experiments, each with a short pulse at a different time, we can measure how the number of atoms in the trench changes over time with minimal effect on the atoms themselves.

Absorption signals measured using a sequence of short-pulse measurements are compared with the signal measured using a single continuous measurement in Figure 6.13. Both techniques give the same results for the variation in absorption as the atoms enter the trench, proving that photon scattering during the continuous measurement is not the cause of the loss observed in experiment.

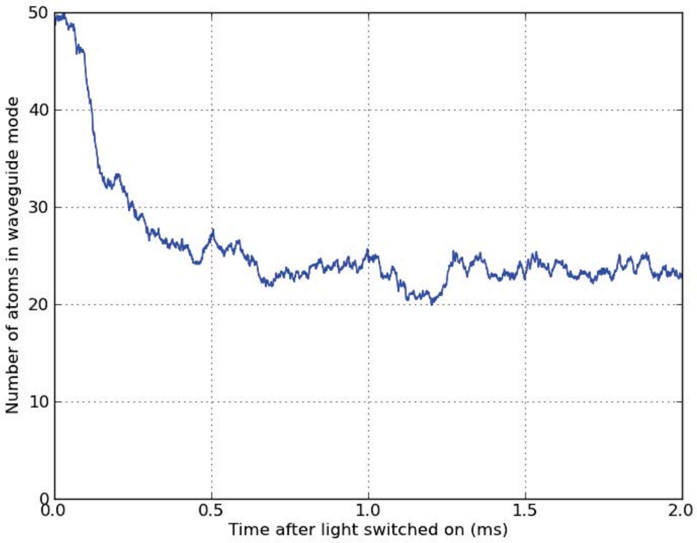

Figure 6.12.: Simulation results showing the evolution of atom number in the waveguide mode after the light is switched on. An initial rapid loss occurs over around 150 μs as atoms in the mode are driven into the trench wall, but subsequently the loss rate drops equalises with the rate at which other atoms fill the mode, giving a stable number (until the total trap population drops significantly).

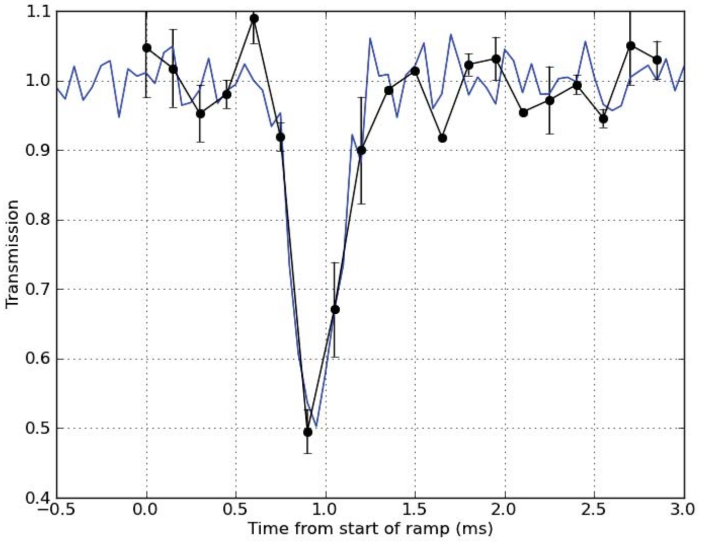

Figure 6.13.: Experimental results showing the change in cross-trench transmission as the 2 μK cloud enters the trench, as measured using an experimental run in which the detection light that stays on throughout (blue). These results are compared to results from a series of experimental runs (black), each one using one 50 μs pulse of light at various times, 150 μs apart.

6.3.5. Conclusions

None of the explanations in this section above can account for the loss rate we observe in experiment. There is a fundamental difficulty in experimentally diagnosing the problem; atom clouds inside the trench cannot be imaged using CCD cameras — the only way we can examine them is by measuring waveguide light absorption. With only the magnitude and duration of the signal to work with, it is very difficult to differentiate between various loss mechanisms.

One way of obtaining further information about the cloud's behaviour in the trench would be to perform absorption measurements of the same experimental sequence using all twelve waveguides, instead of just one. This would show us the cloud's density distribution in z, along the length of the trench, which may shed light on the loss mechanism. At the time of writing this experiment has yet to be performed.

6.4. In-Trench Dipole Forces

Despite the lack of a persistent absorption signal, the large number of atoms in the waveguide mode could still prove useful for other experiments in the trench. One possibility is the use of off-resonant light sent through the waveguide being used to exert dipole forces on atoms, potentially even trapping them. The sensitivity of the in-trench absorption measurements means that we should be able to measure a persistent absorption signal even if only one atom (out of the 36 in the mode) is trapped.

6.4.1. Concept

Generating a trapping potential in the trench can be achieved by sending off-resonant light into a pair of facing waveguides. For trench widths below 19 μm (ours is 16 μm), two non-interfering beams emitted from the waveguides into the trench will create an intensity maximum in the centre of the trench, as shown in Figure 6.14a.

Red-detuned light will therefore create a trap minimum in the centre of our trench. The loose confinement along the axis of the beam (in the X direction) means the depth of the trap is limited by the presence of the trench walls — much higher confinement in this axis can be achieved if the beams can be made to interfere, by ensuring they have the same frequency and polarization. The interference pattern results in a 1-dimensional lattice potential, as shown in Figure 6.14b.

We use light with a wavelength of 805 nm, to the red of the rubidium D_2 transition. Two non-interfering 1 mW beams emerging from each waveguide with an initial spot size of 2.1 μm will generate a trap $k_\mathrm{B}\times 18$ μK deep (atoms hotter than 18 μK will collide with the trench walls), with trap frequencies $f_\mathrm{y} = f_\mathrm{z} = 22$ kHz, $f_\mathrm{x} = 1$ kHz. If we can ensure the beams have the same polarization in the trench, they will interfere, creating a stack of 50 pancake-shaped traps, which near the centre of the trench have a depth of $k_\mathrm{B} \times 530$ μK and trap frequencies $f_\mathrm{y} = f_\mathrm{z} = 31$ kHz, $f_\mathrm{x} = 395$ kHz.

In either case, the trap depths are much greater than the thermal energy of the 2 μK cloud, suggesting they should be capable of trapping multiple atoms. Given that we are currently unable to hold the cloud steady in the trench, the only available strategy for loading an in-trench dipole trap is a quick trench entry, with the trapping light switched on at the time we expect the highest number of atoms to be in the mode volume. Modelling this process using the Monte Carlo simulation suggests that we should be able to capture around 25 atoms using a pair of non-interfering 1 mW beams.

6.4.2. Implementation

A Thorlabs diode laser is used to generate the 805 nm trapping light. The laser has a maximum power of 140 mW, and using the current controller we can switch it on to full power in around 2 μs. Figure 6.15 shows the apparatus. We are still only using one waveguide; the same waveguide used throughout this chapter, which is near the centre of the trench, but now we are coupling trapping light into it in both directions.

Combining and splitting the 780 nm and 805 nm light requires two dichroic mirrors that reflect 780 nm light and transmit 805 nm light. We use Semrock longpass edge filters[3], which have a stated extinction ratio of 10^{-7}. The 805 nm trapping light is much more intense than the 780 nm detection light, so even the small amount reflected from the filter is enough to damage the APD. We therefore have to add another filter before the APD to filter out any remaining 805 nm light. Another threat to the APD

---

[3] Specifically, Semrock LP02-785RU-25 filters.

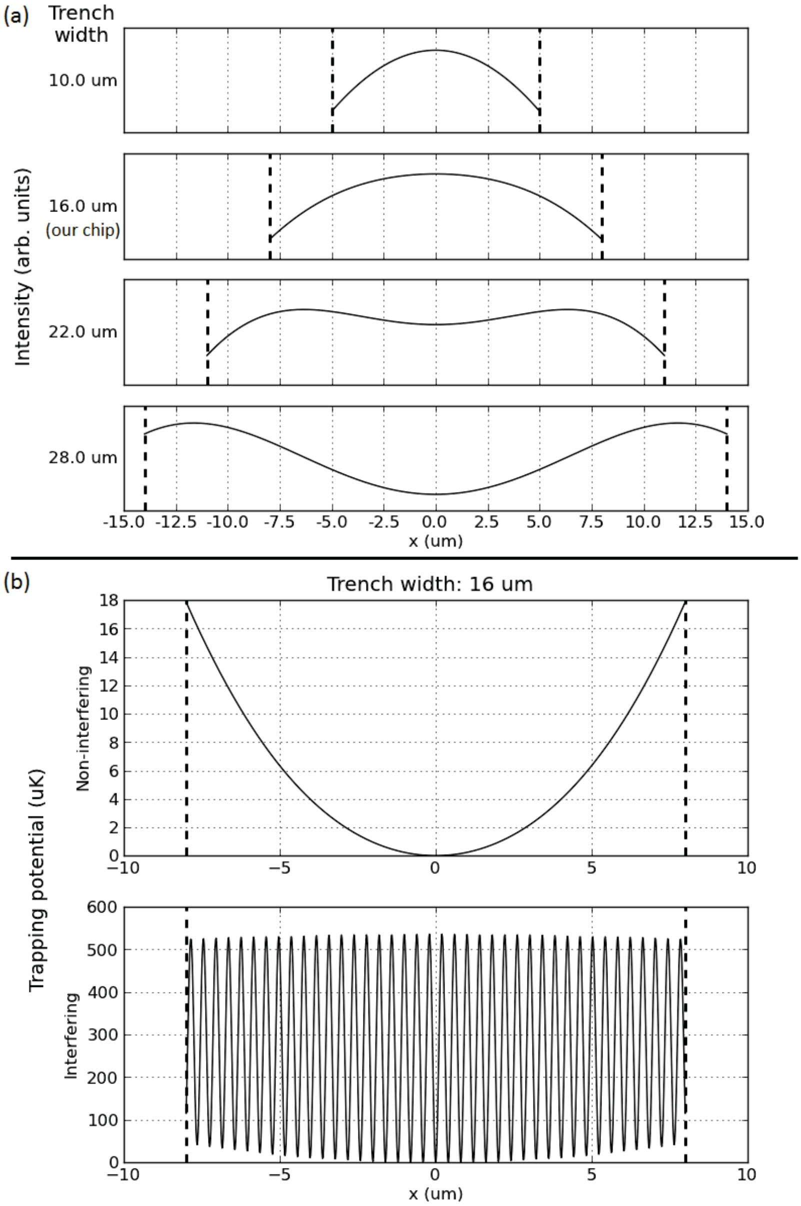

Figure 6.14.: (a) The intensity distribution along the beam axis produced when two counter-propagating, non-interfering beams enter the trench from waveguides on opposite sides of the trench, for four different trench widths. For widths less than 19 μm there is only one intensity maximum, at the centre of the trench. (b) Comparison of the trapping potentials generated by counter-propagating pairs of non-interfering (top) and interfering (bottom) red-detuned waveguide beams. The trench width here is 16 μm and the light wavelength is 805 nm. When using non-interfering beams, the small variation in intensity across the trench greatly limits the trap depth along the beam axis - hot atoms will hit the walls and be ejected from the trap.

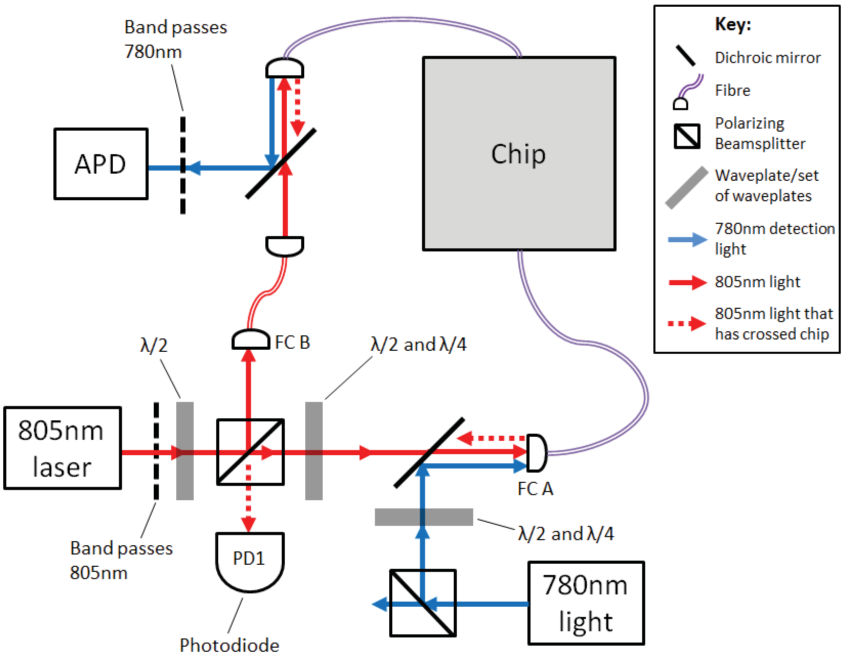

Figure 6.15.: The experimental setup used to inject trapping light and detection light into the chip waveguides.

is posed by spontaneous emission from the 805 nm laser — we find that enough 780 nm light is emitted to damage the APD, so we have to use a fourth filter immediately outside the laser aperture to remove all but the desired 805 nm light. We stabilise the polarization of the detection light by reflecting it off a polarizing beamsplitter.

We can couple at most 40% of the 805 nm light into a single mode fibre, as the beam's profile as it leaves the laser is quite distorted — attempts to improve the coupling efficiency by reshaping the beam with anamorphic prisms were unsuccessful. Once the light is coupled into fibres we measure the total transmission across the chip to be 0.4% in both directions, lower than the transmission of 780 nm light. Assuming the loss rate is uniform across the system we would expect around 6% of the input power to reach the trench. If the total 140 mW out of the laser is split into two 70 mW beams which are then coupled into fibres to give 30 mW entering the chip, this suggests 1.9 mW is entering the trench from either side, which we believe is enough to trap atoms. In reality, the loss from laser to trench will be different for each side, so balancing the powers at the trench will require experimental optimization — we cannot rely on the powers as measured before the light enters the chip. For now we can roughly balance the powers by examining the amount of light scattered out of the trench for each beam. In this configuration we measure a count rate of 1.1 /μs on the APD, and this count rate does not vary much as the power balance is adjusted. We label the two fibre couplers that we use to inject light into the chip fibres as FC A and FC B, as shown in Figure 6.15; FC A collects detection light and 805 nm light, while FC B just collects 805 nm light.

6.4.3. Producing Interference in the Trench

As stated above, we expect greater confinement if the two light beams in the trench interfere, which requires that they have the same polarization. A schematic of how the light polarization changes through the system is shown in Figure 6.16. The polarizing beamsplitter used to adjust the power balance splits the light into vertical and horizontal polarizations, which we write in vector form as $\mathbf{z}$ and $\mathbf{y}$ respectively. We can then control the polarization of the $\mathbf{z}$ light before it is injected into FC A using a $\lambda/4$ waveplate and a $\lambda/2$ waveplate. We can describe the change in polarization from the waveplates with a matrix $\hat{\mathbf{W}}$. Passing through the chip and both fibres will again change the polarization, and we describe this change with a second matrix $\hat{\mathbf{C}}$. Thus the light from FC A will have a polarization $\hat{\mathbf{C}}\hat{\mathbf{W}}\mathbf{z}$ after leaving the chip. This light then leaves FC B and returns to the polarizing beamsplitter, where a component $\hat{\mathbf{C}}\hat{\mathbf{W}}\mathbf{z} \cdot \mathbf{z}$ is reflected into a photodiode PD1.

Light injected into FC B will experience the inverse of these polarization changes, so that when it returns to the beamsplitter, a component $\hat{\mathbf{W}}^{-1}\hat{\mathbf{C}}^{-1}\mathbf{y} \cdot \mathbf{y}$ is transmitted and hits PD1. Thus the total light power hitting PD1 is proportional to

$$\hat{\mathbf{W}}^{-1}\hat{\mathbf{C}}^{-1}\mathbf{y} \cdot \mathbf{y} + \hat{\mathbf{C}}\hat{\mathbf{W}}\mathbf{z} \cdot \mathbf{z}. \tag{6.7}$$

We expect the polarization of the two beams in the chip to be the same if

$$\hat{\mathbf{W}}\mathbf{z} = \hat{\mathbf{C}}^{-1}\mathbf{y}, \tag{6.8}$$

which means that

$$\hat{\mathbf{C}}\hat{\mathbf{W}}\mathbf{z} = \mathbf{y} \tag{6.9}$$

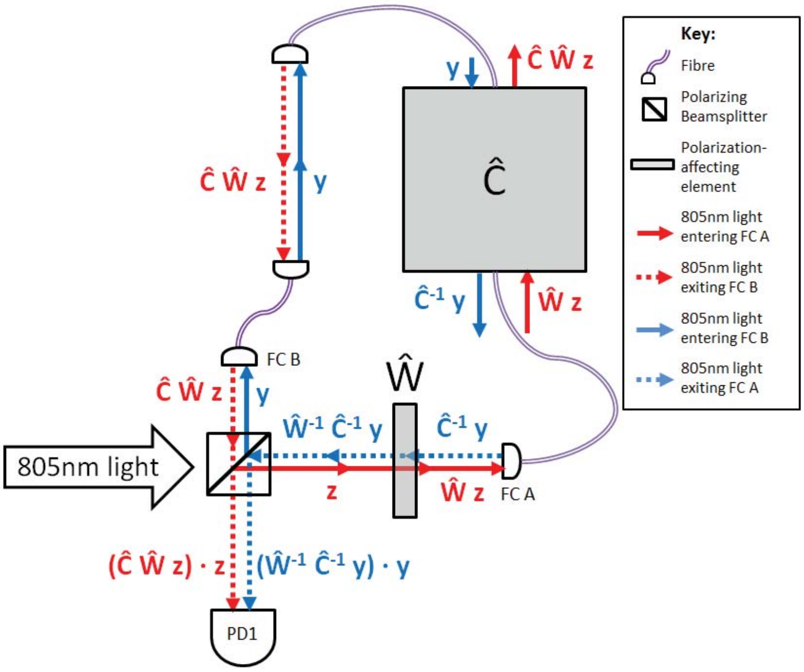

Figure 6.16.: Diagram of how the polarization of the 805 nm light changes through the system. The polarizing beamsplitter splits the light from the laser into two beams of orthogonal polarizations, **z** and **y**. The matrix $\hat{\mathbf{C}}$ represents the effect on these polarizations caused by the chip, and the effect from the $\lambda/4$ and $\lambda/2$ waveplates is represented by a second matrix $\hat{\mathbf{W}}$.

and

$$\hat{\mathbf{W}}^{-1}\hat{\mathbf{C}}^{-1}\mathbf{y} = \mathbf{z}. \tag{6.10}$$

In this case, expression (6.7) is equal to $\mathbf{z}\cdot\mathbf{y} + \mathbf{y}\cdot\mathbf{z} = 0$. Therefore minimising the light power at PD1 by changing $\hat{\mathbf{W}}$ should mean the two beams in the trench have the same polarization, and should generate an interference pattern.

As mentioned in Section 4.3.1 the fibres are not polarization-maintaining, but after attaching them to a heatsink the polarization appears stable over a timescale of a few hours. We can continuously measure the power at PD1 while performing experiments and manually adjust $\hat{\mathbf{W}}$ to keep it low.

6.4.4. Light Shifts in the Trench

A good way to measure the optical dipole trapping potential is through the frequency shift of the resonance transition. We calculate the connection between these following the approach of Steck[92].

We can describe the effect of an electric field $\mathbf{E}$ on an atom's energy levels using perturbation theory - the perturbation operator here is

$$V = -\mathbf{E}\cdot\mathbf{d}, \tag{6.11}$$

where $\mathbf{d}$ is the electric dipole moment of the atom.

Assuming the electric field has a polarization unit vector $\boldsymbol{\epsilon}$ and is monochromatic with an angular frequency of ω, we write it as

$$\mathbf{E}(\mathbf{r},t) = \boldsymbol{\epsilon}\left(E(\mathbf{r})e^{-i\omega t} + E^*(\mathbf{r})e^{i\omega t}\right). \tag{6.12}$$

The AC Stark shift of the ground state of a two level atom is then

$$\begin{aligned}\Delta E_{\mathrm{g}} &= \frac{|\langle g|\,\mathbf{E}\cdot\mathbf{d}\,|e\rangle|^2}{\hbar(\omega+\omega_0)} - \frac{|\langle g|\,\mathbf{E}\cdot\mathbf{d}\,|e\rangle|^2}{\hbar(\omega-\omega_0)}\\ &= -\frac{2\omega_0\,|\langle g|\,\mathbf{E}\cdot\mathbf{d}\,|e\rangle|^2}{\hbar(\omega_0^2-\omega^2)}\\ &= -\frac{2\omega_0\,|\langle g|\,\boldsymbol{\epsilon}\cdot\mathbf{d}\,|e\rangle|^2\,|E(\mathbf{r})|^2}{\hbar(\omega_0^2-\omega^2)}.\end{aligned}$$

where ω_0 is equal to $(E_{\mathrm{e}} - E_{\mathrm{g}})/\hbar$.

We can extend this to an atom with more than two energy levels by summing over all the other states of the system;

$$\Delta E_{\mathrm{g}} = -\sum_{\mathrm{e}} \frac{2\omega_0 \left|\langle g|\,\boldsymbol{\epsilon}\cdot\mathbf{d}\,|e\rangle\right|^2 \left|E(\mathbf{r})\right|^2}{\hbar(\omega_0^2-\omega^2)}. \tag{6.13}$$

This can be rewritten as $\Delta E_{\mathrm{g}} = -\alpha(\omega)\left|E(\mathbf{r})\right|^2$ where $\alpha(\omega)$ here is the Kramers-Heisenberg polarizability for $|g\rangle$;

$$\alpha(\omega) = \sum_{\mathrm{e}} \frac{2\omega_0 \left|\langle g|\,\boldsymbol{\epsilon}\cdot\mathbf{d}\,|e\rangle\right|^2}{\hbar(\omega_0^2-\omega^2)}. \tag{6.14}$$

We can write $\mathbf{d}$ and $\boldsymbol{\epsilon}$ in terms of their angular momentum components about some quantisation axis, so that $\boldsymbol{\epsilon}\cdot\mathbf{d} = \sum_{\mathrm{q}} \epsilon_{\mathrm{q}} d_{\mathrm{q}}$. Incorporating this into equation (6.14) gives

$$\alpha(\omega) = \sum_{\mathrm{q}} \epsilon_{\mathrm{q}} \sum_{\mathrm{e}} \frac{2\omega_0 \left|\langle g|\,d_{\mathrm{q}}\,|e\rangle\right|^2}{\hbar(\omega_0^2-\omega^2)}. \tag{6.15}$$

The states involved in equation (6.14) can be labelled in terms of their quantum numbers[4], such that $|g\rangle \to |n\;S\;L\;J\;I\;F m_{\mathrm{F}}\rangle$ and $|e\rangle \to |n'S'L'J'I'F'm'_{\mathrm{F}}\rangle$. We therefore need to calculate the matrix elements

$$\langle n\;S\;L\;J\;I\;F\;m_{\mathrm{F}}|\,d_{\mathrm{q}}\,\left|n'S'L'J'I'F'm'_{\mathrm{F}}\right\rangle. \tag{6.16}$$

We can simplify using the Wigner-Eckart theorem[93] to separate equation (6.16) into two factors; a reduced matrix element

$$(2F+1)^{-1/2}\,\langle n\;S\;L\;J\;I\;F|\,d_{\mathrm{q}}\,\left|n'S'L'J'I'F'\right\rangle, \tag{6.17}$$

and the Clebsch-Gordon coefficient $\langle F'1m'_{\mathrm{F}}q\,|\,Fm_{\mathrm{F}}\rangle$, which can be calculated using Wigner-3j symbols[93]. We can simplify further, removing I and F from the reduced matrix element, to arrive at an expression in terms of the matrix element $\langle n\;S\;L\;J|\,d_{\mathrm{q}}\,|n'S'L'J'\rangle$, the values of which have been calculated for rubidium by Safranova *et al.*[94]. Details of these simplifications are given in Appendix B.

---

[4] The quantum numbers used here are; the principal quantum number n, the electron spin $\mathbf{S}$, the electron orbital angular momentum $\mathbf{L}$, the total angular momentum $\mathbf{J}=\mathbf{L}+\mathbf{S}$, the nuclear spin $\mathbf{I}$, the total atomic angular momentum $\mathbf{F}=\mathbf{J}+\mathbf{I}$, and the projection of $\mathbf{F}$ onto some quantisation axis m_{F}.

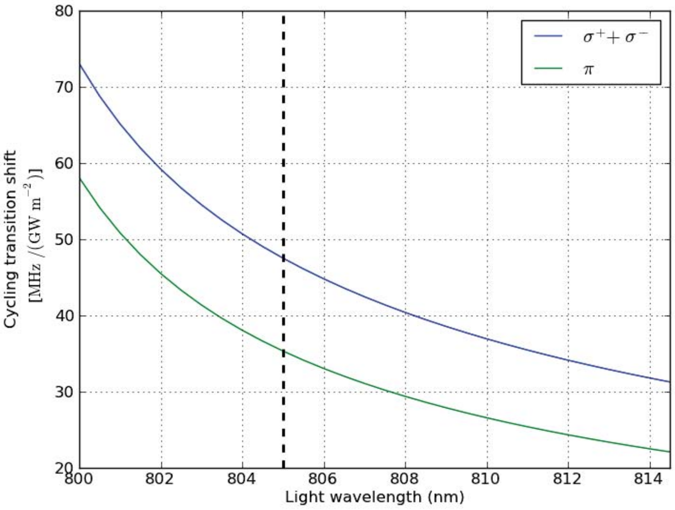

Figure 6.17.: The AC Stark shift in the cycling transition $|F = 2, m_\mathrm{F} = +2\rangle \rightarrow |F = 3, m_\mathrm{F} = +3\rangle$ for a range of wavelengths of trapping light, for π-polarised light and light with equal components of σ^+ and σ^-. The 805 nm wavelength of the in-trench trapping light is marked with a dashed line.

Using these simplifications we can evaluate equation (6.13) for the ground and excited states of the cycling transition; in terms of $|n\, S\, L\, J\, I\, F\, m_\mathrm{F}\rangle$ these are $\left|5, \frac{1}{2}, 0, \frac{1}{2}, \frac{3}{2}, 2, 2\right\rangle$ and $\left|5, \frac{1}{2}, 1, \frac{3}{2}, \frac{3}{2}, 3, 3\right\rangle$ respectively. The total shift in the transition frequency for a range of light wavelengths is shown in Figure 6.17, for π-polarised light and for light with equal components of σ^+ and σ^- polarizations. For 805 nm light, we find the shifts for these polarizations are 35.3 MHz/(GW m^{-2}) and 47.5 MHz/(GW m^{-2}) respectively. The potential experienced by the atoms is dependent only on the shift of the ground state, which we calculate to be -1.69 mK/(GW m^{-2}) $\times\, k_\mathrm{B}$ for both polarizations. Two 1 mW, non-interfering beams counterpropagating in the trench will have a peak intensity of 0.13 GW m^{-2} at the centre of the trench, so the shift here is -220 μK $\times k_\mathrm{B}$.

Using these calculations we can also determine the AC Stark shift for the π-polarised 1030 nm light used for the dimple trap, obtaining a value of 5.68 MHz/(GW m^{-2}), which at the beam's maximum intensity corresponds to a shift of 11.6 MHz. This is in good agreement with experimental measurements.

6.4.5. Expected Absorption Spectra in the Trench

Knowing the light shift in the trench, we can predict the shape of the absorption spectra we expect when we send detection light and trapping light through the same pair of waveguides. Assuming the detection light intensity is much lower than the saturation intensity, the absorption cross section σ_{abs} changes with the detuning Δ as

$$\sigma_{\text{abs}}(\Delta) = \frac{\frac{\Gamma^2}{4}\sigma_0}{\frac{\Gamma^2}{4} + \Delta^2} \tag{6.18}$$

where σ_0 is the cross section on resonance and Γ is the cycling transition linewidth, $2\pi \times 6$ MHz. Δ here is $\omega' - \omega$ where ω' is the angular frequency of the transition and ω is the angular frequency of the detection light. To account for the effect of the 805 nm light we write ω' in terms of the intensity of the 805 nm light $I_{\text{t}}(x, y, z)$ as $\omega_0 + 2\pi \left[f_{\text{shift}} I_{\text{t}}(x, y, z)\right]$, where ω_0 is the angular frequency of the unshifted transition and f_{shift} is the light shift per unit intensity as determined in the previous section.

σ_{abs} is therefore a function of $I_{\text{t}}(x, y, z)$ and the detection light frequency ω. The total absorption coefficient is $a(x, y, z) = n(x, y, z)\sigma_{\text{abs}}(I_{\text{t}}(x, y, z))$ where $n(x, y, z)$ is the atom number density. We can use this to work out the absorption across the trench. If a beam of detection light is emitted by a waveguide at $x = 0$ with an initial Gaussian profile of $I_{(0)}(y, z)$ and propagates in the $+x$ direction, the profile a distance x' from the waveguide is given by

$$I_{(\text{x}')}(y, z) = I_{(0)}(y, z) \exp\left[-\int_0^{x'} a(x, y, z) dx\right]. \tag{6.19}$$

The proportion of the light that reaches the waveguide on the other side of the trench is then

$$\frac{\int_{-\infty}^{+\infty}\int_{-\infty}^{+\infty} I_{(w_{\text{T}})}\, dy\, dz}{\int_{-\infty}^{+\infty}\int_{-\infty}^{+\infty} I_{(0)}\, dy\, dz} \tag{6.20}$$

where w_{T} is the width of the trench. We are ignoring the divergence of the beam and the mode-matching between beam and waveguide here. We make the assumption that the atom density $n(x, y, z)$ is not affected by the presence of the 805 nm light, and is determined only by the shape of the magnetic trap. We have evaluated equation (6.19) numerically for a range

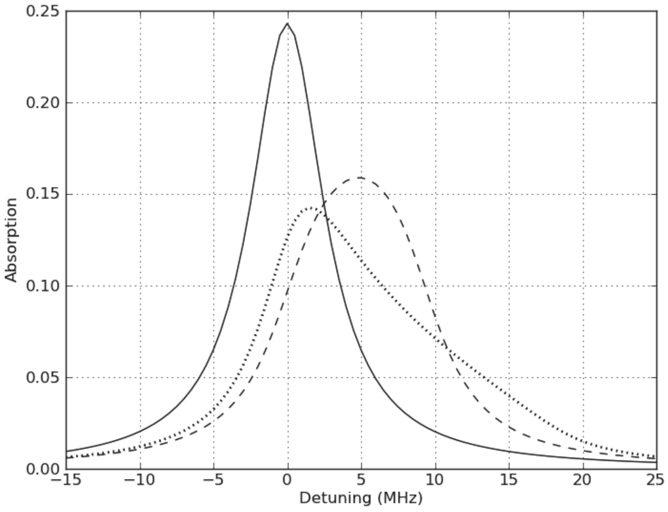

Figure 6.18.: The expected spectra for in-trench absorption measurements with no 805 nm light present (solid), and with two non-interfering 805 nm beams (dashed), and with two interfering beams (dotted). In both cases the 805 nm light is π-polarised and each beam has a power of 1 mW. The atom cloud density is chosen so that around 20 atoms are in the beam mode. We are ignoring the Zeeman shifts due to the presence of the magnetic trap for these calculations.

of detection light frequencies, for non-interfering and interfering 805 nm beams, as shown in Figure 6.18. As illustrated in Figure 6.14 the range of intensities across the trap is much greater when the beams interfere, and as a result the absorption spectrum is broader than it is with non-interfering beams, and is clearly asymmetric. The asymmetry is due to there being more atoms in the low-intensity outer regions of the beam and the nodes of interference pattern than in the high intensity anti-nodes of the interference pattern.

We can therefore hope to determine whether the 805 nm beams are interfering in the trench or not by looking at the shape of the measured absorption spectrum.

6.4.6. Experimental results

We measure the in-trench Stark-shifted absorption spectrum by switching on the 805 nm light before the atoms enter the trench. A typical APD

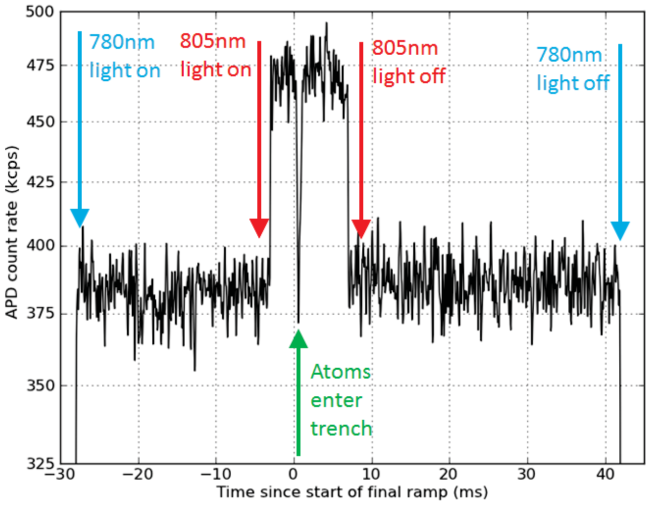

Figure 6.19.: Experimental results showing how the count rate measured by the APD (black) changes during the procedure used to obtain Stark-shifted absorption spectra from clouds in the trench. The 805 nm light is switched on shortly before atoms enter the trench and held on for 10 ms. Some 805 nm light reaches the APD despite the presence of a dichroic mirror and a filter, increasing the count rate by around 100 kcps.

signal obtained using this experimental procedure is shown in Figure 6.19. The shape of the APD signal required the analysis algorithm described in Section 4.2.1 to be modified, so that it was capable of taking into account the period of higher count rate that was measured while the 805 nm light was on.

In Figure 6.20a the measured in-trench absorption spectrum for atoms with no trapping light present is compared with the spectra when 805 nm light enters the trench from each side. Measuring the light shift for light coming from each side allows us to experimentally check that the beam powers are balanced in the trench (in Figure 6.20a they are clearly not balanced). Once we have the powers balanced, we send both beams into the trench and attempt to generate interference in the trench by adjusting the waveplates (labelled $\hat{\mathbf{W}}$ in Section 6.4.3) before the light is coupled into FC A to ensure that the light at PD1 is minimum.

An absorption spectrum with the light in this configuration is shown in Figure 6.20b in red. Comparing these spectra to the expected spectra, it appears that either the beams each have a power of 2.0 mW in the trench and are π-polarised, or that each has a power of 1.5 mW and both are circularly polarised. Adjusting the polarization of both 805 nm beams while maintaining a low power at PD1 and retaking the spectra gives a smaller shift (shown in blue in Figure 6.20b), which suggests that we have moved from circular polarization to π-polarization, and the power is 1.5 mW. However, the shape of both spectra suggests the beams are not interfering in either case. If we adjust $\hat{\mathbf{W}}$ so that the power at PD1 is maximised instead of minimised, there is no clear change in the shape of the spectra.

We can also adjust the polarization of the detection light before it enters FC A, but this only has a small effect on the absorption spectrum. In both light-shifted spectra and unshifted spectra, changing the polarization of the detection light moves the peak by about 2 MHz. As discussed in Chapter 4, if a magnetic field is present during the in-trench absorption measurement, then altering the light polarization allows us to select between σ^+, σ^- and π transitions. The minimum field of the trap here is about 1.7 G, which would separate the π and σ^+ transitions by 2 MHz, so the apparent movement of the peak is presumably actually the disappearance of the π peak and the appearance of the σ^+ peak (and vice versa). The σ^- peak was not visible in the spectrum obtained using circularly polarised detection light.

We have as yet not managed to generate an absorption spectrum that clearly indicates in-trench interference. The slow polarization drift combined with the long time needed to generate clear absorption spectra (around 30 minutes) makes it difficult to perform measurements repeatably, and as with the attempts to stabilise the trapped cloud in the trench, we are again limited in the information we can obtain about the behaviour of atoms and light inside the trench.

Despite the lack of the asymmetric spectrum we expected for interfering trap beams, we have attempted to trap atoms using the 805 nm light, maximising the light shift and then changing the experimental procedure so that the 805 nm light switches on at the time of maximum in-trench absorption. If we have 1.5 mW of non-interfering light entering the trench from each side, we expect a trap depth of 26.6 μK $\times k_{\mathrm{B}}$, which should be able to capture several atoms from the 2 μK cloud as it enters the trench. We have not yet been able to measure a persistent absorption signal from these efforts. This may be the result of too much heating as the cloud enters the trench, or could be due to the same loss mechanism that we were unable

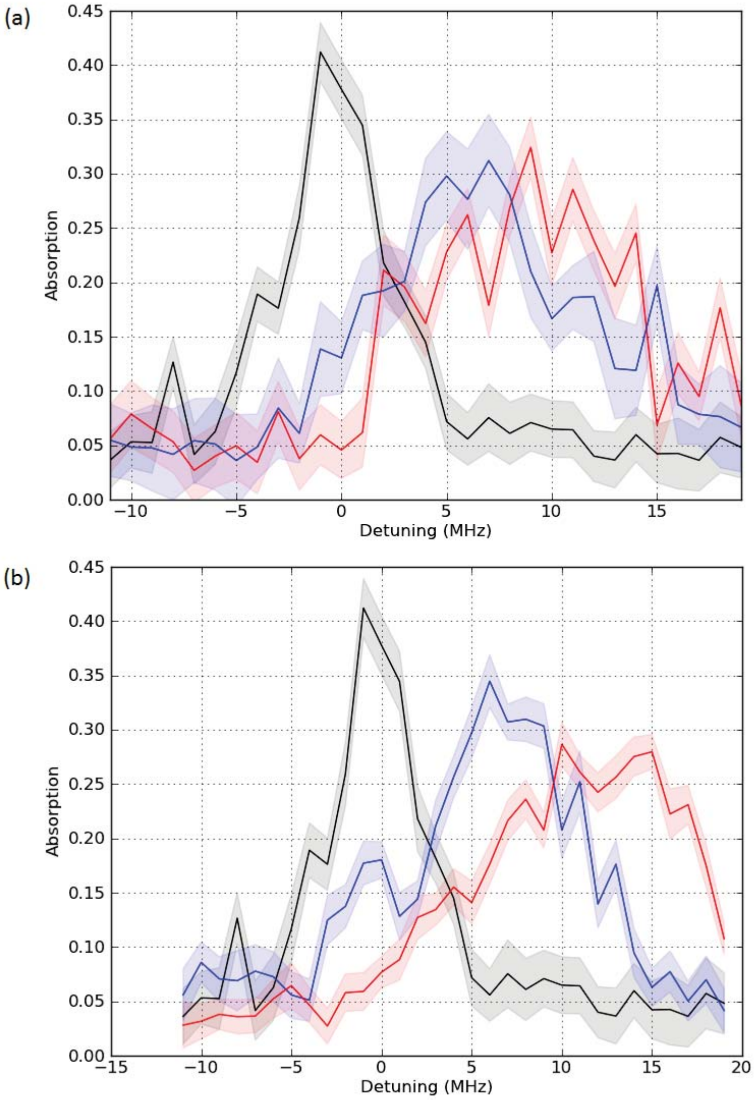

Figure 6.20.: Experimental results showing the absorption spectra obtained using 780 nm detection light and 805 nm light in the trench. (a) shows the spectrum in the absence of 805 nm light (black) and with 805 nm light entering FC A (red) and entering FC B (blue). The shaded area around the lines represents the standard error on the absorption. We can compare the shift caused by light from each fibre to balance the powers in the trench — by comparison with our light shift calculations, it appears that the FC A light is about 0.6 mW more powerful than the FC B light in this case. (b) shows the same unshifted spectrum as in (a) (black), compared with spectra with light entering both FC A and FC B simultaneously (red and blue). For both of these spectra we expect the beams to have the same polarization as each other; we believe that for one spectrum this polarization is linear (blue) while for the other it is circular (red). Neither spectrum has the asymmetric shape expected for interfering beams.

to identify in Section 6.3. We have used short-pulse measurements to check for optically trapped atoms to rule out the possibility of photon scattering destroying the trapped cloud. There is a possibility that the 2 μs switch-on of the 805 nm light is too slow, given the high oscillation frequencies of the trap it produces.

The spectra predicted in Section 6.4.5 do not apply for optically trapped atoms, which we expect to occupy only high-intensity regions of the trap, giving a narrower spectrum centered at a higher frequency shift. The exact spectrum is dependent on temperature; for a cloud at 100 μK in the 1 mW lattice trap we expect the absorption to peak at a frequency 20 MHz above the free space resonance.

Time constraints have prevented further experimental investigation into in-trench trapping. Using an 805 nm laser with a higher maximum power would remove the possibility that the trap is simply not deep enough, and passing the light through an AOM could allow for a much shorter switch-on time. Additionally, if the magnetically trapped cloud could be held stable in the trench, we could try loading the optical trap in a more controlled fashion, removing a potential source of error. The logical next step towards optically trapping atoms would therefore be performing the multiple-waveguide measurement described in Section 6.3.5.

7. Conclusions and Outlook

This thesis has covered significant progress in the waveguide chip experiment. The addition of the dimple beam to the experiment has allowed us to evaporatively cool atom clouds with much better efficiency than was previously achievable. Purely rf-driven evaporation in our magnetic trap gave a maximum achievable phase space density of around 2×10^{-5}, but using the dimple we achieved 4×10^{-2}, achieving an increase in evaporation efficiency by a factor of 4 without having to break vacuum. Using a higher power laser for our dimple beam would allow for even higher phase space densities, potentially enabling the creation of a BEC. Rebuilding the chip using much less glue could also give a lower vacuum pressure in the chamber, which will allow for more efficient cooling.

The dimple cooling process has enabled much higher atom densities inside the trench; we now observe absorption signals of 50%, compared to earlier experiments which measured signals of 1% and 8% for the MOT and magnetically trapped clouds respectively. The 50% absorption signals are visible in the results of only one run of the experiment, in contrast to the earlier signals, which required many sets of results to be averaged together before the absorption signals could be discerned from the noise.

The higher densities allow for the prospect of optical trapping in the trench. By measuring light shifts in atoms in the trench we can, to an extent, characterise the trapping light as it crosses the trench. The magnitude of the light shift suggests that enough light is present in the trench for trapping to occur — if the cloud's movement into the trench can be slowed down without significant atom loss occurring, the interaction between the atoms and the optical dipole potential will be more straightforward, and optical trapping would presumably not be far off. Chances of successfully trapping could be improved if a trapping laser with a higher power is used. Currently, we achieve 1.5 mW of 805 nm light in the trench, which is enough power to trap atoms according to theory and simulation, but not by a large margin.

If optical trapping using one pair of waveguides is feasible, it would be a simple matter to couple the trapping light into other waveguides, potentially resulting in an array of 12 microscopic optical traps, each containing a small number of atoms. This has potential applications in quantum information processing[40]. A Rydberg excitation in one microtrap can block excitations in the adjacent microtrap, 10 μm away, via the Rydberg blockade[95]. Blockade ranges of 10 μm have been have already been demonstrated experimentally, using principle quantum numbers $n \approx 100$[96]. This blockade interaction means the optical traps could be used to form a two-qubit quantum gate[97].

Some interesting experiments are also possible if cavities can be integrated into the waveguide setup. Recent experiments have demonstrated 'photon blockade' occurring in an optical microcavity containing a single atom[98], where excitation of the atom-cavity system by one photon blocks the transmission of a second photon, leading to antibunching in the transmission through the cavity. Shi *et al.* have shown that the same effect could be observed in a cavity coupled to a waveguide[99], with the cavity either off to the side of the waveguide or directly in the path of the waveguide, forming a gap similar in size to our trench. Turning our gap into a cavity by making the waveguide facets reflective would be difficult using our current fabrication process, although one group has managed to build a waveguide-with-gap setup into a microcavity by adding dielectric mirrors to the outer ends of the waveguides[100, 101].

If a cold cloud can be held in the trench for an extended period of time, there is the potential to implement a feedback system. If the parameters of the cloud in the trench can be obtained in real-time, using multiple-waveguide measurements (this could be achieved using the non-destructive detection system described in [102]), then we can implement a feedback loop that adjusts the trap parameters based on this data. The introduction of a feedback loop to a quantum system opens up a variety of experimental possibilities, such as feedback cooling (as demonstrated for a single atom by Kubanek *et al.*[103]) and realisation of non-trivial quantum states[104]. For BECs, Szigeti *et al.* have shown that feedback can be used to drive a BEC towards a stable spatial mode, which can help to reduce noise in the system[105].

Our work on the waveguide chip device clearly shows the scientific potential for devices that bring together photonic technologies and techniques in atomic physics, not just in quantum information processing but in quantum physics as a whole.

List of Figures

Bibliography

[1] T. M. Roach, H. Abele, M. G. Boshier, H. L. Grossman, K. P. Zetie, and E. A. Hinds. Realization of a Magnetic Mirror for Cold Atoms. *Phys. Rev. Lett.*, 75(4):629–632, Jul 1995.

[2] A. I. Sidorov, R. J. McLean, W. J. Rowlands, D. C. Lau, J. E. Murphy, M. Walkiewicz, G. I. Opat, and P. Hannaford. Specular reflection of cold caesium atoms from a magnetostatic mirror. *Quant. Semiclass. Opt.*, 8, Jun 1996.

[3] I G Hughes, P A Barton, T M Roach, M G Boshier, and E A Hinds. Atom optics with magnetic surfaces: I. Storage of cold atoms in a curved 'floppy disk'. *Journal of Physics B: Atomic, Molecular and Optical Physics*, 30(3):647, 1997.

[4] A. I. Sidorov, R. J. McLean, B. A. Sexton, D. S. Gough, T. J. Davis, A. Akulshin, G. I. Opat, and P. Hannaford. Micron-scale magnetic structures for atom optics. *Comptes Rendus de l'Acadamie des Sciences - Series IV - Physics*, 2(4):565 – 571, 2001.

[5] V. Vuletic, T. Fischer, M. Praeger, T. W. Hänsch, and C. Zimmermann. Microscopic Magnetic Quadrupole Trap for Neutral Atoms with Extreme Adiabatic Compression. *Phys. Rev. Lett.*, 80(8):1634–1637, Feb 1998.

[6] J. Fortágh, A. Grossmann, C. Zimmermann, and T. W. Hänsch. Miniaturized Wire Trap for Neutral Atoms. *Phys. Rev. Lett.*, 81(24):5310–5313, Dec 1998.

[7] Dirk Müller, Dana Z. Anderson, Randal J. Grow, Peter D. D. Schwindt, and Eric A. Cornell. Guiding neutral atoms around curves with lithographically patterned current-carrying wires. *Phys. Rev. Lett.*, 83:5194–5197, Dec 1999.

[8] J. Denschlag, D. Cassettari, A. Chenet, S. Schneider, and J. Schmiedmayer. A neutral atom and a wire: towards mesoscopic atom optics. *Applied Physics B*, 69(4):291–301, 1999.

[9] Ron Folman, Peter Krüger, Donatella Cassettari, Björn Hessmo, Thomas Maier, and Jörg Schmiedmayer. Controlling Cold Atoms using Nanofabricated Surfaces: Atom Chips. *Phys. Rev. Lett.*, 84(20):4749–4752, May 2000.

[10] J. Reichel, W. Hänsel, and T. W. Hänsch. Atomic Micromanipulation with Magnetic Surface Traps. *Phys. Rev. Lett.*, 83(17):3398–3401, Oct 1999.

[11] K. B. Davis, M. O. Mewes, M. R. Andrews, N. J. van Druten, D. S. Durfee, D. M. Kurn, and W. Ketterle. Bose-Einstein Condensation in a Gas of Sodium Atoms. *Phys. Rev. Lett.*, 75(22):3969–3973, Nov 1995.

[12] M. H. Anderson, J. R. Ensher, M. R. Matthews, C. E. Wieman, and E. A. Cornell. Observation of Bose-Einstein Condensation in a Dilute Atomic Vapor. *Science*, 269(5221):198–201, 1995.

[13] H. Ott, J. Fortágh, G. Schlotterbeck, A. Grossmann, and C. Zimmermann. Bose-Einstein Condensation in a Surface Microtrap. *Phys. Rev. Lett.*, 87(23):230401, Nov 2001.

[14] W. Hänsel, P. Hommelhoff, T. W. Hänsch, and J. Reichel. Bose-Einstein condensation on a microelectronic chip. *Nature*, 413:498–501, Oct 2001.

[15] S. Schneider, A. Kasper, Ch. vom Hagen, M. Bartenstein, B. Engeser, T. Schumm, I. Bar-Joseph, R. Folman, L. Feenstra, and J. Schmiedmayer. Bose-Einstein condensation in a simple microtrap. *Phys. Rev. A*, 67(2):023612, Feb 2003.

[16] C. Zimmermann, J. Fortágh, H. Ott, S. Kraft, and A. Günther. Bose-Einstein Condensates in Magnetic Micro Traps. *The Expanding Frontier of Atomic Physics: Proceedings of the XVIII International Conference on Atomic Physics*, pages 47–54, 2003.

[17] M. P. A. Jones, C. J. Vale, D. Sahagun, B. V. Hall, and E. A. Hinds. Spin coupling between cold atoms and the thermal fluctuations of a metal surface. *Phys. Rev. Lett.*, 91:080401, Aug 2003.

[18] C. D. J. Sinclair, E. A. Curtis, I. Llorente Garcia, J. A. Retter, B. V. Hall, S. Eriksson, B. E. Sauer, and E. A. Hinds. Bose-Einstein condensation on a permanent-magnet atom chip. *Phys. Rev. A*, 72(3):031603, Sep 2005.

[19] S. Aubin, S. Myrskog, M. H. T. Extavour, L. J. LeBlanc, D. McKay, A. Stummer, and J. H. Thywissen. Rapid sympathetic cooling to Fermi degeneracy on a chip. *Nature Physics*, 2:384–387, May 2006.

[20] T. Schumm, S. Hofferberth, L. M. Andersson, S. Wildermuth, S. Groth, I. Bar-Joseph, J. Schmiedmayer, and P. Kruger. Matter-wave interferometry in a double well on an atom chip. *Nature Physics*, 1:57–62, September 2005.

[21] Ying-Ju Wang, Dana Z. Anderson, Victor M. Bright, Eric A. Cornell, Quentin Diot, Tetsuo Kishimoto, Mara Prentiss, R. A. Saravanan, Stephen R. Segal, and Saijun Wu. Atom Michelson Interferometer on a Chip Using a Bose-Einstein Condensate. *Phys. Rev. Lett.*, 94:090405, Mar 2005.

[22] Peter Krüger, Albrecht Haase, Ron Folman, and Jörg Schmiedmayer. *Quantum Information Processing with Neutral Atoms on Atom Chips*, pages 257–265. Wiley-VCH Verlag GmbH and Co. KGaA, 2005.

[23] Antonio Negretti, Philipp Treutlein, and Tommaso Calarco. Quantum computing implementations with neutral particles. *Quantum Information Processing*, 10(6):721–753, 2011.

[24] D. Cano, B. Kasch, H. Hattermann, R. Kleiner, C. Zimmermann, D. Koelle, and J. Fortágh. Meissner Effect in Superconducting Microtraps. *Phys. Rev. Lett.*, 101(18):183006, Oct 2008.

[25] Mandip Singh. Macroscopic entanglement between a Bose Einstein condensate and a superconducting loop. *Opt. Express*, 17(4):2600–2610, Feb 2009.

[26] Peter Horak, Bruce G. Klappauf, Albrecht Haase, Ron Folman, Jörg Schmiedmayer, Peter Domokos, and E. A. Hinds. Possibility of single-atom detection on a chip. *Phys. Rev. A*, 67:043806, Apr 2003.

[27] S. Eriksson, M. Trupke, H. F. Powell, D. Sahagun, C. D.J. Sinclair, E. A. Curtis, B. E. Sauer, E. A. Hinds, Z. Moktadir, C. O. Gollasch, and M. Kraft. Integrated optical components on atom chips. *The European Physical Journal D - Atomic, Molecular, Optical and Plasma Physics*, 35(1):135–139, 2005.

[28] M. Trupke, E. A. Hinds, S. Eriksson, E. A. Curtis, Z. Moktadir, E. Kukharenka, and M. Kraft. Microfabricated high-finesse optical cavity with open access and small volume. *Applied Physics Letters*, 87(21):–, 2005.

[29] M. Trupke, J. Goldwin, B. Darquié, G. Dutier, S. Eriksson, J. Ashmore, and E. A. Hinds. Atom detection and photon production in a scalable, open, optical microcavity. *Phys. Rev. Lett.*, 99:063601, Aug 2007.

[30] J. Goldwin, M. Trupke, J. Kenner, A. Ratnapala, and E.A.. Hinds. Fast cavity-enhanced atom detection with low noise and high fidelity. *Nature Communications*, 2:418, Jul 2011.

[31] Albrecht Haase, Björn Hessmo, and Jörg Schmiedmayer. Detecting magnetically guided atoms with an optical cavity. *Opt. Lett.*, 31(2):268–270, Jan 2006.

[32] YanQiang Guo, Gang Li, YanFeng Zhang, PengFei Zhang, JunMin Wang, and TianCai Zhang. Efficient fluorescence detection of a single neutral atom with low background in a microscopic optical dipole trap. *Science China Physics, Mechanics and Astronomy*, 55(9):1523–1528, 2012.

[33] T. Puppe, I. Schuster, A. Grothe, A. Kubanek, K. Murr, P. W. H. Pinkse, and G. Rempe. Trapping and observing single atoms in a blue-detuned intracavity dipole trap. *Phys. Rev. Lett.*, 99:013002, Jul 2007.

[34] P. Quinto-Su, M. Tscherneck, M. Holmes, and N. Bigelow. On-chip optical detection of laser cooled atoms. *Opt. Express*, 12(21):5098–5103, Oct 2004.

[35] Meng Khoon Tey, Zilong Chen, Syed Abdullah Aljunid, Brenda Chng, Florian Huber, Gleb Maslennikov, and Christian Kurtsiefer. Strong interaction between light and a single trapped atom without the need for a cavity. *Nature Physics*, 4:924–927, 2008.

[36] Akifumi Takamizawa, Tilo Steinmetz, Rémi Delhuille, Theodor W. Hänsch, and Jakob Reichel. Miniature fluorescence detector for single atom observation on a microchip. *Opt. Express*, 14(23):10976–10983, Nov 2006.

[37] Marco Wilzbach, Dennis Heine, Sönke Groth, Xiyuan Liu, Thomas Raub, Björn Hessmo, and Jörg Schmiedmayer. Simple integrated single-atom detector. *Opt. Lett.*, 34(3):259–261, Feb 2009.

[38] M. Wilzbach, A. Haase, M. Schwarz, D. Heine, K. Wicker, X. Liu, K.-H. Brenner, S. Groth, Th. Fernholz, B. Hessmo, and J. Schmiedmayer. Detecting neutral atoms on an atom chip. *Fortschritte der Physik*, 54(8-10):746–764, 2006.

[39] D Heine, W Rohringer, D Fischer, M Wilzbach, T Raub, S Loziczky, XiYuan Liu, S Groth, B Hessmo, and J Schmiedmayer. A single-atom detector integrated on an atom chip: fabrication, characterization and application. *New Journal of Physics*, 12(9):095005, 2010.

[40] R.A. Nyman, S. Scheel, and E.A. Hinds. Prospects for using integrated atom-photon junctions for quantum information processing. *Quantum Information Processing*, 10(6):941–953, 2011.

[41] P W H Pinkse, A Mosk, M Weidemüller, M W Reynolds, T W Hijmans, and J T M Walraven. Adiabatically changing the phase-space density of a trapped Bose gas. *Physical Review Letters*, 78(6):4, 1996.

[42] D. M. Stamper-Kurn, H.-J. Miesner, A. P. Chikkatur, S. Inouye, J. Stenger, and W. Ketterle. Reversible Formation of a Bose-Einstein Condensate. *Phys. Rev. Lett.*, 81:2194–2197, Sep 1998.

[43] Michael C. Garrett, Adrian Ratnapala, Eikbert D. van Ooijen, Christopher J. Vale, Kristian Weegink, Sebastian K. Schnelle, Otto Vainio, Norman R. Heckenberg, Halina Rubinsztein-Dunlop, and Matthew J. Davis. Growth dynamics of a Bose-Einstein condensate in a dimple trap without cooling. *Phys. Rev. A*, 83:013630, Jan 2011.

[44] Tino Weber, Jens Herbig, Michael Mark, Hanns-Christoph Nägerl, and Rudolf Grimm. Bose-Einstein Condensation of Cesium. *Science*, 299(5604):232–235, 2003.

[45] Zhao-Yuan Ma, Christopher J Foot, and Simon L Cornish. Optimized evaporative cooling using a dimple potential: an efficient route to Bose-Einstein condensation. *Journal of Physics B: Atomic, Molecular and Optical Physics*, 37(15):3187, 2004.

[46] Q. Beaufils, R. Chicireanu, T. Zanon, B. Laburthe-Tolra, E. Maréchal, L. Vernac, J.-C. Keller, and O. Gorceix. All-optical production of chromium Bose-Einstein condensates. *Phys. Rev. A*, 77:061601, Jun 2008.

[47] D Jacob, E Mimoun, L De Sarlo, M Weitz, J Dalibard, and F Gerbier. Production of sodium Bose-Einstein condensates in an optical dimple trap. *New Journal of Physics*, 13(6):065022, 2011.

[48] Zhao-Yuan Ma, Christopher J Foot, and Simon L Cornish. Optimized evaporative cooling using a dimple potential: an efficient route to Bose-Einstein condensation. *Journal of Physics B: Atomic, Molecular and Optical Physics*, 37(15):3187, 2004.

[49] Z-Y Ma, A M Thomas, C J Foot, and S L Cornish. The evaporative cooling of a gas of caesium atoms in the hydrodynamic regime. *Journal of Physics B: Atomic, Molecular and Optical Physics*, 36(16):3533, 2003.

[50] N. P. Proukakis, J. Schmiedmayer, and H. T. C. Stoof. Quasicondensate growth on an atom chip. *Phys. Rev. A*, 73:053603, May 2006.

[51] M. Horikoshi and K. Nakagawa. Atom chip based fast production of Bose-Einstein condensate. *Applied Physics B: Lasers and Optics*, 82:363–366, 2006. 10.1007/s00340-005-2083-z.

[52] Y.-J. Lin, A. R. Perry, R. L. Compton, I. B. Spielman, and J. V. Porto. Rapid production of ^{87}Rb Bose-Einstein condensates in a combined magnetic and optical potential. *Phys. Rev. A*, 79:063631, Jun 2009.

[53] D. Comparat, A. Fioretti, G. Stern, E. Dimova, B. Laburthe Tolra, and P. Pillet. Optimized production of large Bose-Einstein condensates. *Phys. Rev. A*, 73:043410, Apr 2006.

[54] Matthias Kohnen. *Detecting Atoms with Integrated Optics and Frequency-Synthesised Light*. PhD thesis, Imperial College London, 2011.

[55] Manuel Succo. *An integrated optical-waveguide chip for measurement of cold-atom clouds*. PhD thesis, Imperial College London, 2011.

[56] S.J. Hewlett and F. Ladouceur. Fourier decomposition method applied to mapped infinite domains: scalar analysis of dielectric waveguides down to modal cutoff. *Lightwave Technology, Journal of*, 13(3):375 –383, mar 1995.

[57] Guillaume Lepert. *Integrated optics for coupled-cavity quantum electrodynamics.* PhD thesis, Imperial College London, 2013.

[58] J. Reichel, W. Hänsel, and T. W. Hänsch. Atomic micromanipulation with magnetic surface traps. *Phys. Rev. Lett.*, 83:3398–3401, Oct 1999.

[59] S. Wildermuth, P. Krüger, C. Becker, M. Brajdic, S. Haupt, A. Kasper, R. Folman, and J. Schmiedmayer. Optimized magneto-optical trap for experiments with ultracold atoms near surfaces. *Phys. Rev. A*, 69:030901, Mar 2004.

[60] A. S. Arnold, J. S. Wilson, and M. G. Boshier. A simple extended-cavity diode laser. *Rev. Sci. Instrum.*

[61] Jocelyn Anna Retter. *Cold Atom Microtraps abova a Videotape Surface.* PhD thesis, University of Sussex, 2002.

[62] C. Wieman and T. W. Hänsch. Doppler-free laser polarization spectroscopy. *Phys. Rev. Lett.*, 36(20):1170–1173, May 1976.

[63] G. Ritt, G. Cennini, C. Geckeler, and M. Weitz. Laser frequency offset locking using a side of filter technique. *Applied Physics B: Lasers and Optics*, 79:363–365, 2004. 10.1007/s00340-004-1559-6.

[64] W. H. Wing. On neutral particle trapping in quasistatic electromagnetic fields. *Progress in Quantum Electronics*, 8(3-4):181 – 199, 1984.

[65] Wolfgang Petrich, Michael H. Anderson, Jason R. Ensher, and Eric A. Cornell. Stable, Tightly Confining Magnetic Trap for Evaporative Cooling of Neutral Atoms. *Phys. Rev. Lett.*, 74(17):3352–3355, Apr 1995.

[66] W. Ketterle, D. S. Durfee, and D. M. Stamper-Kurn. Making, probing and understanding Bose-Einstein condensates, 1999.

[67] M P A Jones, C J Vale, D Sahagun, B V Hall, C C Eberlein, B E Sauer, K Furusawa, D Richardson, and E A Hinds. Cold atoms probe the magnetic field near a wire. *Journal of Physics B: Atomic, Molecular and Optical Physics*, 37(2):L15, 2004.

[68] J. Estève, C. Aussibal, T. Schumm, C. Figl, D. Mailly, I. Bouchoule, C. I. Westbrook, and A. Aspect. Role of wire imperfections in micromagnetic traps for atoms. *Phys. Rev. A*, 70:043629, Oct 2004.

[69] S. Aigner, L. Della Pietra, Y. Japha, O. Entin-Wohlman, T. David, R. Salem, R. Folman, and J. Schmiedmayer. Long-range order in electronic transport through disordered metal films. *Science*, 319(5867):1226–1229, 2008.

[70] J. Reichel and J.H. Thywissen. Using magnetic chip traps to study Tonks-Girardeau quantum gases. *J. Phys. IV France*, 116:265–274, 2004.

[71] J.-B. Trebbia, C. L. Garrido Alzar, R. Cornelussen, C. I. Westbrook, and I. Bouchoule. Roughness Suppression via Rapid Current Modulation on an Atom Chip. *Phys. Rev. Lett.*, 98(26):263201, Jun 2007.

[72] Eric R.I. Abraham and Eric A. Cornell. Teflon feedthrough for coupling optical fibers into ultrahigh vacuum systems. *Appl. Opt.*, 37(10):1762–1763, Apr 1998.

[73] Alan V. Oppenheim, Ronald W. Schafer, and John R. Buck. *Discret-Time Signal Processing.* Prentice Hall, 1999.

[74] M. Kohnen, M. Succo, P. G. Petrov, R. A. Nyman, M. Trupke, and E. A. Hinds. An array of integrated atom-photon junctions. *Nature Photonics*, 5:35–38, 2011.

[75] O. J. Luiten, M. W. Reynolds, and J. T. M. Walraven. Kinetic theory of the evaporative cooling of a trapped gas. *Phys. Rev. A*, 53:381–389, Jan 1996.

[76] James P. Burke, John L. Bohn, B. D. Esry, and Chris H. Greene. Prospects for Mixed-Isotope Bose-Einstein Condensates in Rubidium. *Phys. Rev. Lett.*, 80:2097–2100, Mar 1998.

[77] Chen-Lung Hung, Xibo Zhang, Nathan Gemelke, and Cheng Chin. Accelerating evaporative cooling of atoms into Bose-Einstein condensation in optical traps. *Phys. Rev. A*, 78(1):011604, Jul 2008.

[78] J.-F. Clément, J.-P. Brantut, M. Robert-de Saint-Vincent, R. A. Nyman, A. Aspect, T. Bourdel, and P. Bouyer. All-optical runaway evaporation to Bose-Einstein condensation. *Phys. Rev. A*, 79(6):061406, Jun 2009.

[79] A. G. Martin, K. Helmerson, V. S. Bagnato, G. P. Lafyatis, and D. E. Pritchard. rf spectroscopy of trapped neutral atoms. *Phys. Rev. Lett.*, 61:2431–2434, Nov 1988.

[80] J. P. Brantut, J. F. Clément, M. Robert de Saint Vincent, G. Varoquaux, R. A. Nyman, A. Aspect, T. Bourdel, and P. Bouyer. Light-shift tomography in an optical-dipole trap for neutral atoms. *Phys. Rev. A*, 78:031401, Sep 2008.

[81] D. Sofikitis, G. Stern, L. Kime, E. Dimova, A. Fioretti, D. Comparat, and P. Pillet. Loading a dipole trap from an atomic reservoir. *The European Physical Journal D*, 61(2):437–442, 2011.

[82] T. A. Savard, K. M. O'Hara, and J. E. Thomas. Laser-noise-induced heating in far-off resonance optical traps. *Phys. Rev. A*, 56:R1095–R1098, Aug 1997.

[83] Wolfgang Ketterle and David E. Pritchard. Atom cooling by time-dependent potentials. *Phys. Rev. A*, 46:4051–4054, Oct 1992.

[84] P. W. H. Pinkse, A. Mosk, M. Weidemüller, M. W. Reynolds, T. W. Hijmans, and J. T. M. Walraven. Adiabatically changing the phase-space density of a trapped bose gas. *Phys. Rev. Lett.*, 78:990–993, Feb 1997.

[85] Graham D. Bruce, Sarah L. Bromley, Giuseppe Smirne, Lara Torralbo-Campo, and Donatella Cassettari. Holographic power-law traps for the efficient production of Bose-Einstein condensates. *Phys. Rev. A*, 84:053410, Nov 2011.

[86] Huang Wu and Christopher J Foot. Direct simulation of evaporative cooling. *Journal of Physics B: Atomic, Molecular and Optical Physics*, 29(8):L321, 1996.

[87] Huang Wu, Ennio Arimondo, and Christopher J. Foot. Dynamics of evaporative cooling for Bose-Einstein condensation. *Phys. Rev. A*, 56:560–569, Jul 1997.

[88] M Holland, J Williams, K Coakley, and J Cooper. Trajectory simulation of kinetic equations for classical systems. *Quantum and Semiclassical Optics: Journal of the European Optical Society Part B*, 8(3):571, 1996.

[89] P. W. H. Pinkse, A. Mosk, M. Weidemüller, M. W. Reynolds, T. W. Hijmans, and J. T. M. Walraven. One-dimensional evaporative cooling of magnetically trapped atomic hydrogen. *Phys. Rev. A*, 57:4747–4760, Jun 1998.

[90] E. L. Surkov, J. T. M. Walraven, and G. V. Shlyapnikov. Collisionless motion and evaporative cooling of atoms in magnetic traps. *Phys. Rev. A*, 53:3403–3408, May 1996.

[91] P. W. H. Pinkse, A. Mosk, M. Weidemüller, M. W. Reynolds, T. W. Hijmans, and J. T. M. Walraven. One-dimensional evaporative cooling of magnetically trapped atomic hydrogen. *Phys. Rev. A*, 57:4747–4760, Jun 1998.

[92] D. A. Steck. Quantum and atom optics, revision 0.9.12, 2007: *http://atomoptics.uoregon.edu/ dsteck/teaching/quantum- optics.*

[93] Albert Messiah. *Quantum Mechanics.* Dover, 1961.

[94] M. S. Safronova, Carl J. Williams, and Charles W. Clark. Relativistic many-body calculations of electric-dipole matrix elements, lifetimes, and polarizabilities in rubidium. *Phys. Rev. A*, 69:022509, Feb 2004.

[95] M. D. Lukin, M. Fleischhauer, R. Cote, L. M. Duan, D. Jaksch, J. I. Cirac, and P. Zoller. Dipole blockade and quantum information processing in mesoscopic atomic ensembles. *Phys. Rev. Lett.*, 87:037901, Jun 2001.

[96] E. Urban, T. A. Johnson, T. Henage, L. Isenhower, D. D. Yavuz, T. G. Walker, and Saffman. Observation of Rydberg blockade between two atoms. *Nature Physics*, 5:110–114, Feb 2009.

[97] M. Saffman, T. G. Walker, and K. Mølmer. Quantum information with Rydberg atoms. *Rev. Mod. Phys.*, 82:2313–2363, Aug 2010.

[98] K. M. Birnbaum, A. Boca, R. Miller, A. D. Boozer, T. E. Northup, and H. J. Kimble. Observation of Rydberg blockade between two atoms. *Nature*, 436:87–90, Jul 2005.

[99] T. Shi, Shanhui Fan, and C. P. Sun. Two-photon transport in a waveguide coupled to a cavity in a two-level system. *Phys. Rev. A*, 84:063803, Dec 2011.

[100] S. Gleyzes, A. El Amili, R. A. Cornelussen, P. Lalanne, C. I. Westbrook, A. Aspect, J. Estve, G. Moreau, A. Martinez, X. Lafosse, L. Ferlazzo, J. C. Harmand, D. Mailly, and A. Ramdane. Towards a monolithic optical cavity for atom detection and manipulation. *The European Physical Journal D*, 53(1):107–111, 2009.

[101] Abdelkrim El Amili, Sébastien Gleyzes, and Christoph Ira Westbrook. Atom-photon interactions in a system of coupled cavities. *J. Opt. Soc. Am. B*, 29(7):1618–1624, Jul 2012.

[102] M Kohnen, P G Petrov, R A Nyman, and E A Hinds. Minimally destructive detection of magnetically trapped atoms using frequency-synthesized light. *New Journal of Physics*, 13(8):085006, 2011.

[103] A. Kubanek, M. Koch, C. Sames, A. Ourjoumtsev, T. Wilk, P. Pinkse, and G. Rempe. Feedback control of a single atom in an optical cavity. *Applied Physics B: Lasers and Optics*, 102:433–442, 2011. 10.1007/s00340-011-4410-x.

[104] Kurt Jacobs. How to project qubits faster using quantum feedback. *Phys. Rev. A*, 67(3):030301, Mar 2003.

[105] S. S. Szigeti, M. R. Hush, A. R. R. Carvalho, and J. J. Hope. Continuous measurement feedback control of a Bose-Einstein condensate using phase-contrast imaging. *Phys. Rev. A*, 80(1):013614, Jul 2009.

[106] J. T. M. Walraven. Atomic hydrogen in magnetostatic traps. *Conference proceedings: Quantum dynamics of simple systems (SUSSP Proceedings)*, 44, 1996. Editors: G.-L. Oppo, S. M. Barnett, E. Riis, and M. Wilkinson.

[107] A. R. Edmonds. *Angular Momentum in Quantum Mechanics.* Princeton, 1996.

A. Linking Trap Shape to Phase Space Density

To understand the link between the deformation parameter and phase space density, it is useful to start with some general thermodynamic expressions. For a system of trapped atoms, the total number of atoms N is given by

$$N = \int \rho\left(\epsilon\right) f\left(\epsilon\right) d\epsilon, \tag{A.1}$$

where $\rho\left(\epsilon\right)$ is the density of states, given in Section 5.1.1 as

$$\rho(\epsilon) = \frac{2\pi(2m)^{\frac{3}{2}}}{h^3} \int_{\mathrm{U}(\mathbf{r})\leq\epsilon} d^3r\,\sqrt{\epsilon - U(\mathbf{r})}, \tag{A.2}$$

and $f\left(\epsilon\right)$ is the population distribution which, in the absence of quantum effects, is given by

$$f\left(\epsilon\right) = z \exp\left(-\epsilon/k_{\mathrm{B}}T\right), \tag{A.3}$$

where z is the fugacity. Evaluating the integral for N gives

$$N = \frac{z}{\lambda_{\mathrm{dB}}^3} \int \exp\left(-\frac{U\left(\mathbf{r}\right)}{k_{\mathrm{B}}T}\right) d^3r, \tag{A.4}$$

where λ_{dB} is defined as

$$\lambda_{\mathrm{dB}} = \frac{h}{\sqrt{2\pi m k_{\mathrm{B}}T}}. \tag{A.5}$$

Comparing this expression with equation (5.21) shows that the fugacity z reduces to $n_0\lambda_{\mathrm{dB}}^3$ for systems where quantum effects are negligible[106].

The single particle partition function Z_1 for a trapped ideal gas is given by

$$Z_1 = \frac{1}{h^3} \int \exp\left(-\frac{U\left(\mathbf{r}\right) + p^2/2m}{k_{\mathrm{B}}T}\right) d^3p\ d^3r. \tag{A.6}$$

Evaluating the momentum integral gives

$$Z_1 = \frac{1}{\lambda_{\mathrm{dB}}^3} \int \exp\left(-\frac{U(\mathbf{r})}{k_{\mathrm{B}}T}\right) d^3r, \tag{A.7}$$

which by comparison to equation (A.4) demonstrates that

$$n_0 \lambda_{\mathrm{dB}}^3 = N/Z_1. \tag{A.8}$$

The internal energy of a gas at equilibrium is given by

$$E = \int \epsilon \rho(\epsilon) f(\epsilon) \, d\epsilon, \tag{A.9}$$

which using the expressions given above can be rewritten as

$$E = N k_{\mathrm{B}} T^2 \frac{1}{Z_1} \frac{\partial Z_1}{\partial T}. \tag{A.10}$$

It is useful here to define an *effective volume* V_{e}, such that

$$V_{\mathrm{e}} = N/n_0, \tag{A.11}$$

which can be rewritten as

$$V_{\mathrm{e}} = Z_1 \lambda_{\mathrm{dB}}^3, \tag{A.12}$$

using equation (A.8). Using this definition, we can write

$$\begin{aligned}
\frac{1}{Z_1}\frac{\partial Z_1}{\partial T} &= \frac{1}{V_{\mathrm{e}}}\frac{\partial V_{\mathrm{e}}}{\partial T} + \lambda_{\mathrm{dB}}^3 \frac{\partial}{\partial T}\left(\frac{1}{\lambda_{\mathrm{dB}}^3}\right) \\
&= \frac{1}{V_{\mathrm{e}}}\frac{\partial V_{\mathrm{e}}}{\partial T} + \lambda_{\mathrm{dB}}^3 \frac{\partial}{\partial T}\left(\frac{(2\pi m k_{\mathrm{B}} T)^{3/2}}{\lambda_{\mathrm{dB}}^3}\right) \\
&= \frac{1}{V_{\mathrm{e}}}\frac{\partial V_{\mathrm{e}}}{\partial T} + \frac{3}{2T},
\end{aligned}$$

so that the expression for energy becomes

$$E = N k_{\mathrm{B}} T \left(\frac{T}{V_{\mathrm{e}}}\frac{\partial V_{\mathrm{e}}}{\partial T} + \frac{3}{2}\right). \tag{A.13}$$

This expression depends on the quantity $\frac{T}{V_{\mathrm{e}}}\frac{\partial V_{\mathrm{e}}}{\partial T}$. We refer to this as the deformation parameter γ, so that

$$\gamma = \frac{T}{V_{\mathrm{e}}} \frac{\partial V_{\mathrm{e}}}{\partial T}. \tag{A.14}$$

We can relate the phase space density to the value of γ using the Helmholtz free energy of the system F, given by

$$F = E - TS. \tag{A.15}$$

F can be written in terms of the partition function by using Gibb's expression for the entropy S of a system;

$$S = -k_{\mathrm{B}} \sum_{\mathrm{i}} P_{\mathrm{i}} \log P_{\mathrm{i}}. \tag{A.16}$$

P_{i} is the probability of finding the system in state i, which can be related to the partition function Z using

$$P_{\mathrm{i}} = n_{\mathrm{i}}/N = \exp\left(-E_{\mathrm{i}}/k_{\mathrm{B}}T\right)/Z, \tag{A.17}$$

so that

$$S = \left(\sum_{\mathrm{i}} P_{\mathrm{i}} E_{\mathrm{i}}/T + k_{\mathrm{B}} \sum_{\mathrm{i}} P_{\mathrm{i}} \log Z \right). \tag{A.18}$$

As $\sum_{\mathrm{i}} P_{\mathrm{i}} E_{\mathrm{i}}$ is just the internal energy E, and $\sum_{\mathrm{i}} P_{\mathrm{i}} = 1$;

$$S = \frac{E}{T} + k_{\mathrm{B}} \log Z. \tag{A.19}$$

Using this expression in equation (A.15) gives

$$F = E - T\left(\frac{E}{T} + k_{\mathrm{B}} \log Z\right), \tag{A.20}$$

which reduces down to

$$F = -k_{\mathrm{B}} T \log Z. \tag{A.21}$$

Rewriting this in terms of the single particle partition function gives

$$F = -k_{\mathrm{B}} T \log\left(\frac{Z_1^N}{N!}\right). \tag{A.22}$$

Using the expression for internal energy in equation (A.13) and the definition of γ we can therefore write

$$Nk_{\mathrm{B}}T\left(\gamma+\frac{3}{2}\right)-TS=-k_{\mathrm{B}}T\log\left(\frac{Z_1^N}{N!}\right). \tag{A.23}$$

Stirling's approximation can be used to simplify;

$$N\left(\gamma+\frac{3}{2}\right)-\frac{S}{k_{\mathrm{B}}}=-N\log\left(Z_1\right)+N\log\left(N\right)-N, \tag{A.24}$$

finally giving

$$Z_1=N\exp\left(\frac{S}{Nk_{\mathrm{B}}}-\gamma-\frac{5}{2}\right). \tag{A.25}$$

As the phase space density $n_0\lambda_{\mathrm{dB}}^3=N/Z_1$, we can write

$$n_0\lambda_{\mathrm{dB}}^3=\exp\left(\gamma+\frac{5}{2}-\frac{S}{Nk_{\mathrm{B}}}\right). \tag{A.26}$$

B. Simplifying the Light Shift Calculation

The light shift calculations discussed in Section 6.4.4 hinge on the calculation of the matrix element

$$M = \langle n\, S\, L\, J\, I\, F\, m_{\mathrm{F}}|\, d_{\mathrm{q}} \left| n'S'L'J'I'F'm'_{\mathrm{F}} \right\rangle . \tag{B.1}$$

This appendix covers the simplifications we perform to enable this calculation.

The Wigner-Eckart theorem states that for a tensor operator of order k $\mathbf{T}^{(k)}$[93],

$$\langle \tau\; J\; m|\, |\mathbf{T}^{(k)}|\, \left|\tau' J' m'\right\rangle = \frac{(-1)^{2k}}{\sqrt{2J+1}} \left\langle \tau\; J|\, |\mathbf{T}^{(k)}|\, \left|\tau' J'\right\rangle \right. \langle J' k\; m' q | J m\rangle. \tag{B.2}$$

For our calculation k is equal to 1, as the electric dipole operator is a vector operator. Applying this to the matrix element we wish to simplify:

$$\begin{aligned} &\langle n\; S\; L\; J\; I\; F\; m_{\mathrm{F}}|\, d_{\mathrm{q}} \left| n'S'L'J'I'F'm'_{\mathrm{F}} \right\rangle = \\ &\qquad \frac{1}{\sqrt{2F+1}} \langle n\; S\; L\; J\; I\; F|\, d_{\mathrm{q}} \left| n'S'L'J'I'F' \right\rangle \langle F' 1 m'_{\mathrm{F}} q | F\; m_{\mathrm{F}} \rangle. \end{aligned} \tag{B.3}$$

We can write the Clebsch-Gordon coefficient $\langle F' 1 m'_{\mathrm{F}} q | F\; m_{\mathrm{F}} \rangle$ in terms of a Wigner-3j symbol (in the square brackets);

$$\langle F' 1 m'_{\mathrm{F}} q | F\; m_{\mathrm{F}} \rangle = (-1)^{(F'-1+m_{\mathrm{F}})} \sqrt{2F+1} \begin{bmatrix} F' & 1 & F \\ m_{\mathrm{F}} & q & -m_{\mathrm{F}} \end{bmatrix}, \tag{B.4}$$

giving

$$\langle n\,S\,L\,J\,I\,F\,m_{\mathrm{F}}|\,d_{\mathrm{q}}\,|n'S'L'J'I'F'm'_{\mathrm{F}}\rangle =$$
$$(-1)^{(F'-1+m_{\mathrm{F}})}\,\langle n\,S\,L\,J\,I\,F|\,d_{\mathrm{q}}\,|n'S'L'J'I'F'\rangle \begin{bmatrix} F' & 1 & F \\ m_{\mathrm{F}} & q & -m_{\mathrm{F}} \end{bmatrix}. \quad \text{(B.5)}$$

Since we do not excite the nucleus, $I = I'$, so we can separate out the nuclear angular momentum I from the reduced matrix element $\langle n\,S\,L\,J\,I\,F|\,d_{\mathrm{q}}\,|n'S'L'J'I'F'\rangle$ by making use of a second theorem[107];

$$\langle \gamma\,j_1\,j_2\,J|\,|\mathbf{T}^{(k)}|\,|\gamma' j_1' j_2' J'\rangle =$$
$$(-1)^{(j_1+j_2'+J+k)}\sqrt{(2J+1)(2J'+1)} \begin{Bmatrix} j_1 & J & j_2' \\ J' & j_1' & k \end{Bmatrix} \times \langle \gamma\,j_1|\,|\mathbf{T}^{(k)}|\,|\gamma' j_1'\rangle\,, \quad \text{(B.6)}$$

where the curly brackets indicate Wigner-6j symbols. Substituting $\gamma \to nLS$, $j_1 \to J$, $j_2 \to I$ and $J \to F$;

$$\langle n\,S\,L\,J\,I\,F|\,d_{\mathrm{q}}\,|n'S'L'J'I'F'\rangle =$$
$$(-1)^{(J+I+F+1)}\sqrt{(2F+1)(2F'+1)} \begin{Bmatrix} J & F & I \\ J & J' & 1 \end{Bmatrix} \times \langle n\,L\,S\,J|\,d_{\mathrm{q}}\,|n'L'S'J'\rangle\,. \quad \text{(B.7)}$$

Thus an expression initially in terms of $\langle n\,S\,L\,J\,I\,F\,m_{\mathrm{F}}|\,d_{\mathrm{q}}\,|n'S'L'J'I'F'm'_{\mathrm{F}}\rangle$ is simplified to an expression in terms of $\langle n\,L\,S\,J|\,d_{\mathrm{q}}\,|n'L'S'J'\rangle$, the values of which are tabulated for rubidium-87[94]. All other coefficients in the final expression can be calculated easily[1].

---

[1] With Mathematica.